ALMA MATER STUDIORUM
UNIVERSITÀ DI BOLOGNA

DIPARTIMENTO DI INGEGNERIA INDUSTRIALE - DIN

CORSO DI LAUREA MAGISTRALE IN

Ingegneria Meccanica con Curriculum Biomeccanica

Development and mechanical testing of synthetic 3D printed models of healthy and metastatic vertebrae

Tesi di laurea in Biomeccanica Sperimentale M

Relatore

Prof. Luca Cristofolini

Presentata da

Bruno Daniela

Correlatore

Prof. Paolo Gargiulo

Prof. Marco Viceconti

Ing. Marco Palanca

Ing. Riccardo Forni

SESSIONE II

Anno Accademico 2022/2023

Abstract

The spine is frequently affected by metastases, which can disrupt the normal distribution of bone tissues, reduce load-bearing capacity, and lead to spinal instability. However, the assessment of spinal instability remains unclear for most patients. A comprehensive understanding of metastatic vertebrae is crucial to identify and subsequently treat those at a high risk of fractures.

The aim of the study is to evaluate the mechanical properties of synthetic 3D printed models of healthy and metastatic vertebrae to replicate the mechanical behavior of ex-vivo vertebrae. The goal was to explore the possibility of providing an alternative solution by producing a large number of repeatable samples with high accuracy. Using an innovative approach that incorporated Digital Anatomy Printing and Digital Materials, over a hundred models (both healthy and metastatic) were printed based on medical images and subjected to compression loading.

Initially, the study focused on characterizing the properties of digital materials and then assessed the influence of morphology on the models. At the end the stress-strain analysis indicated a correspondence between the fracture mode of metastatic synthetic models and ex-vivo models. Once this method and the associated evidence are generalized on a larger sample, they could contribute to the development of new biomechanical-based criteria within current scoring systems. This would provide clearer guidelines for assessing spinal instability and open new avenues for research on fracture risk prediction.

Key words: spinal metastases; spinal instability; 3D Printing; Digital Anatomy Printing; mechanical test; medical images; segmentation; polymers; stress-strain analysis.

Contents

Motivations

The spine plays a crucial role in supporting the head and trunk, protecting the spinal cord, and reducing stress on the brain. However, neoplastic diseases like primary spinal tumors and spinal metastases can compromise its proper functioning [1],[2]. Bone metastases result either in an abnormal focalized reduction of bone mass (i.e. lytic tissue), or in an increase of bone density (i.e. blastic tissue). In some cases, both lytic and blastic tissues are observed in the same bone (i.e. mixed metastasis) [3]. In case of lytic metastases, the load-bearing cross-section of the bone is reduced with consequent decrease in strength. On the other hand, blastic metastases result in denser bone with abnormal structural organization, this can reduce the load-bearing capacity of the vertebrae and results in catastrophic events such as mechanical instability, vertebral fractures and paralysis [3].

Although there are clinical tools to refer patients with vertebral metastases to orthopaedic consultation (e.g. the Spine Instability Neoplastic Score) and to assess the risk of fracture, these tools lack in sensitivity and/or specificity and lead to under or over-treatment of patients. Clinical assessment of spinal instability remains uncertain for many patients, and treatment choices often rely on the experience of individual clinicians. Additionally, existing scoring systems do not incorporate biomechanical parameters that consider how the presence of metastases affects the mechanical competence of the vertebrae [4],[5]. Several experimental and computational biomechanical studies have analysed the effects of bone metastases on the mechanical behaviour of the vertebrae in order to improve our understanding of their failure location.

Numerous in vitro biomechanical studies [6], [7], [8] have shown that adding biomechanical parameters (i.e. the size and position of the metastasis) improves the correlation with the mechanical competence of the metastatic vertebrae and aims to prevent fractures. In another

biomechanical work, the material properties of blastic, lytic and healthy trabecular tissues were explored. The authors remarked on differences in mechanical behavior for each type of tissue and they observed a good fit with finite element (FE) models, based on micro-CT, to evaluate the local internal strain and the failure location of vertebrae with different types of metastases.

To investigate the complete strain distribution both on the external surface and inside the volume of vertebrae, advanced techniques such as Digital Image Correlation (DIC) [9] and Digital Volume Correlation (DVC) [10] can be employed. DIC and DVC have been recently employed to assess the mechanical competence of the human metastatic spine in multi-vertebrae segments, revealing the potential relevance of certain metastatic features in modifying strain distribution and driving spinal biomechanical instability [11], [12].

Recent study has shown that to achieve reliable numerical simulations, the models need to accurately replicate experimental biomechanics, including both the elastic and plastic phases leading up to the breaking load. To accomplish this, the models should be validated [13],[14]. Geometry is obtained through image acquisition and transformed into a mesh model. Mathematical equations are solved to determine displacements and loads. The gray levels in the images are converted into density and subsequently into intrinsic material properties, such as Young's modulus. But there are still issue to analyse bone metastases such as mesh quality, material properties, appropriate energy balance methods.

Even if today mathematical models are a non-invasive method that can be used for predicting forces and moments, in vivo and in vitro tests are considered more reliable. However both of them must be repeatable, proving a consistent response when the same input is given several times, and reproducible, providing the same output when performed in different instances, following the same protocol. This allows us to compare the results obtained from the same test, carried out following the same protocol, on two different specimens, such as two vertebrae, one with and one without metastases. Due to the fact human cadaveric specimens are difficult to obtain and their use is subjected to strict ethical regulation, more often animal models from the alimentary chain are used, even if there are strong anatomical differences within quadrupeds and humans, both in terms of dimensions and microstructure, but also

mechanical properties [15].

The introduction of 3D printing may provided a solution to these issues. Starting from CT or MR medical images, it is possible to create custom 3D synthetic models of the patient's case, thus allowing for the production of a large number of repeatable samples with high accuracy, as well as the ability to analyze properties that would be challenging to study in vitro. While many studies have focused on the use of 3D-printed synthetic models for surgical planning and aesthetic purposes, both for cortical and trabecular bone, none of them have thoroughly characterized the mechanical properties of these models or compared them to in vitro tests.
Hence, the aim of this study is to replicate the mechanical behavior of ex-vivo vertebrae, with an exploration of the possibility of building reliable copies of both healthy and diseased vertebrae using 3D printed synthetic models. To achieve this objective, specific sub-goals have been established: firstly, to characterize the mechanical properties of 3D printable materials, subsequently to evaluate the mechanical characteristics of 3D-printed models based on anatomy and morphology. Then, to compare healthy and metastatic 3D models and to compare these models with ex-vivo specimens.
This objective introduces an innovative approach to spinal biomechanical studies, incorporating digital anatomy printing, mechanical tests, and research on fracture risk prediction.

Chapter 1

Background

1.1 Anatomy of the human spine

The spine is one of the most complex portions of the skeleton to study.
It serves as a mechanical support structure for the human body and it is the subject of numerous biomechanical studies [16]. The spine fulfills three primary biomechanical functions:

- It bears and distributes loads, along with managing the resulting bending forces generated by the head, trunk, and pelvis. This provision of structural support and balance enables the maintenance of an upright posture.
- It facilitates the physiological movements of the head, trunk, and pelvis, including the relative rotation between vertebral bodies while preventing their translation.
- It acts as a protective barrier for the spinal cord, nerve roots, and several internal organs, diminishing the transmission of accelerations from the lower limbs to these internal organs.

The spine is composed of an arrangement of vertebrae and intervertebral discs, secured by a series of ligaments. There are typically 33 or 34 vertebrae within the spine, categorized based on their location into cervical (7 vertebrae, C1 - C7), thoracic (12 vertebrae, T1 – T12), lumbar (5 vertebrae, L1 – L5), sacrum (5 fused vertebrae), and coccyx (4 fused vertebrae) regions; as represent in Figure 1.1.

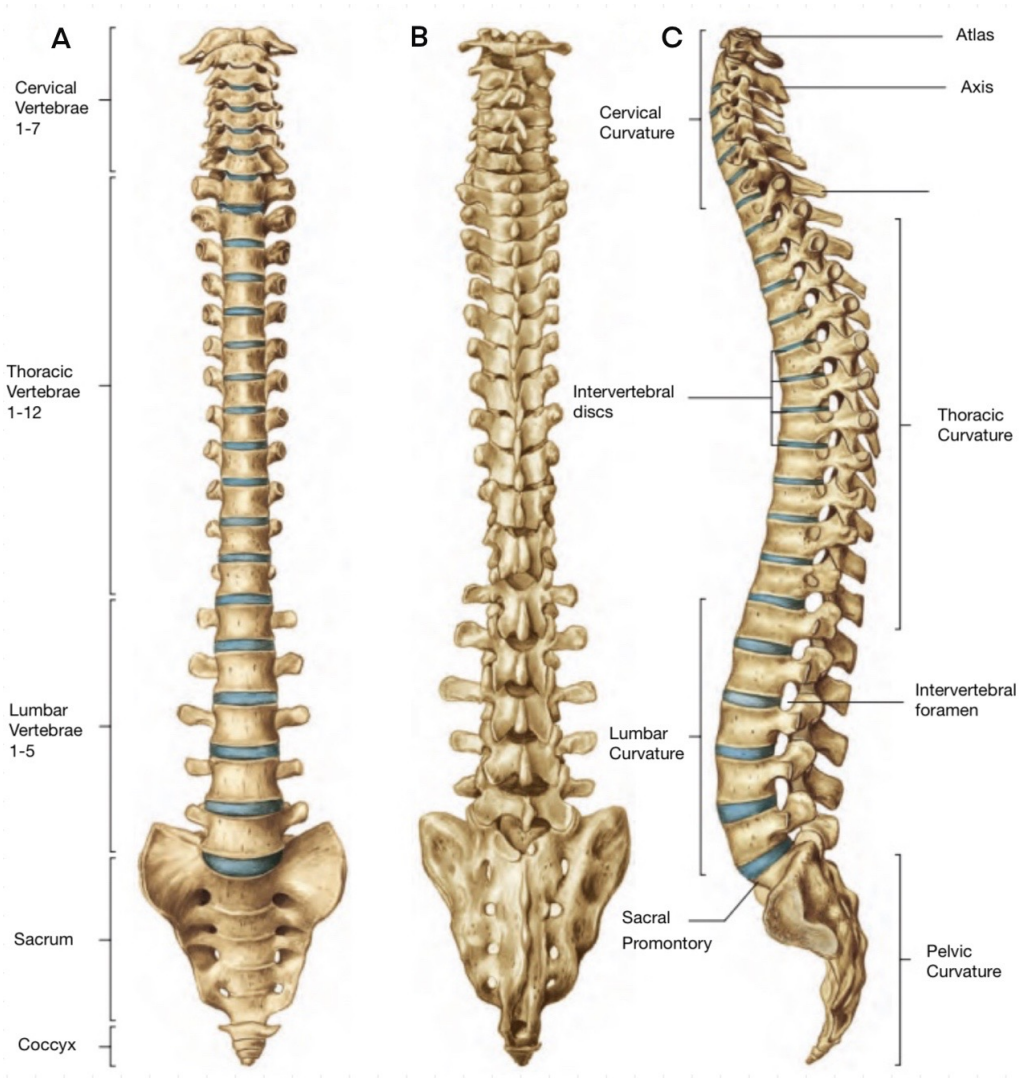

Figure 1.1: *The vertebral column. A, Anterior aspect. B, Posterior aspect. C, Lateral aspect [17].*

The intervertebral discs consist of two soft tissues [18]: the anulus fibrosus, which comprises layers of fibrocartilage, and the nucleus pulposus, which contains fibers scattered within a mucoprotein gel. The structure of these intervertebral discs enables them to function as shock absorbers, distributing pressure in all directions and mitigating force peaks from the lower limbs. Additionally, by connecting the vertebrae to each other, the intervertebral discs restrict certain movements of the spine, restraining translations while allowing rotations, thus preserving neighboring nervous tissues.

The spinal ligaments are fibrous bands or sheets of connective tissue made up of collagenous fibers. Each ligament has its specific function [19], but in general, they serve to inter-

connect the vertebrae and maintain an upright posture, preventing excessive movements or movements in specific directions. Additionally, the spine has different muscle insertions which provide spinal stability along with dynamic neuromuscular control systems [16]. While each of these components possesses unique characteristics, behaviours, and specific roles within the musculoskeletal system, they collectively contribute to the spine's fundamental functions (Figure 1.2).

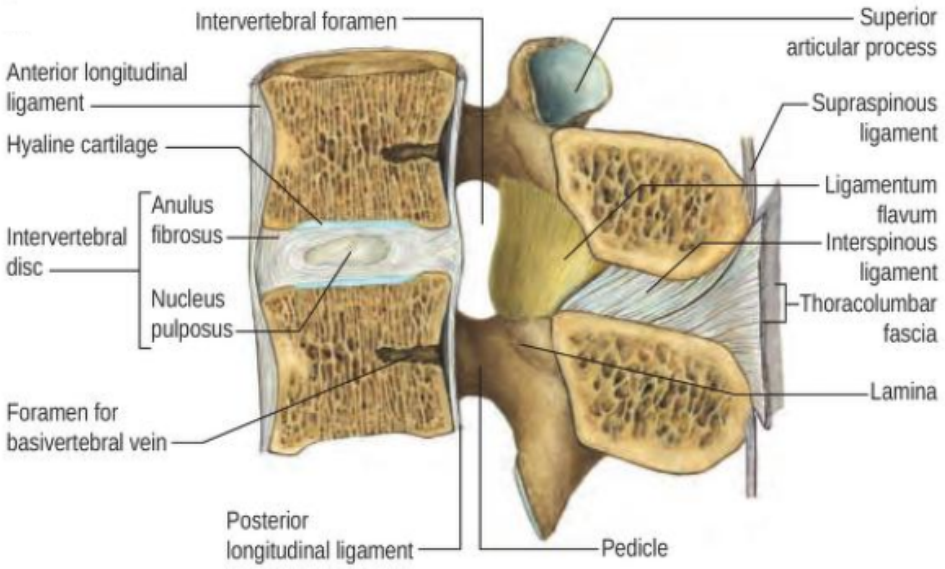

Figure 1.2: *A median sagittal section through the upper lumbar vertebral column showing discs and ligaments [17].*

1.1.1 Vertebra

Vertebrae are irregular short bones, whose dimensions and mass varies depending on their position in the spine, load, pathology [17]. A typical vertebra consists of the vertebral body, that is the largest part of a vertebra, more or less cylindrical in shape and of the vertebral arch, a posterior bony ring connected to the body by a pair of pedicles and laminae from which arise seven articular processes (posterior bilateral joints, connecting each vertebra to the adjacent one) [17]. Between the vertebral body and the arch lies the spinal cavity, where the spinal cord is located. The vertebrae are the hard tissues of the spine.

Thoracic vertebrae (Figure 1.3) increase in size as one moves downward along the spine.

They are mechanically stiffer and less mobile compared to other regions of the spine due to the presence of costovertebral articulations, the structure of the rib cage, and the orientation of the pedicles. These characteristics provide the necessary support for bipedal posture and protection for the spinal cord and other organs within the thoracic cavity [16]. Thoracic vertebrae are distinguished by the presence of facets on the sides of the vertebral bodies for articulation with the heads of the ribs. Additionally, there are facets on the transverse processes of all vertebrae, except T11 and T12, for articulation with the tubercles of the ribs [17].

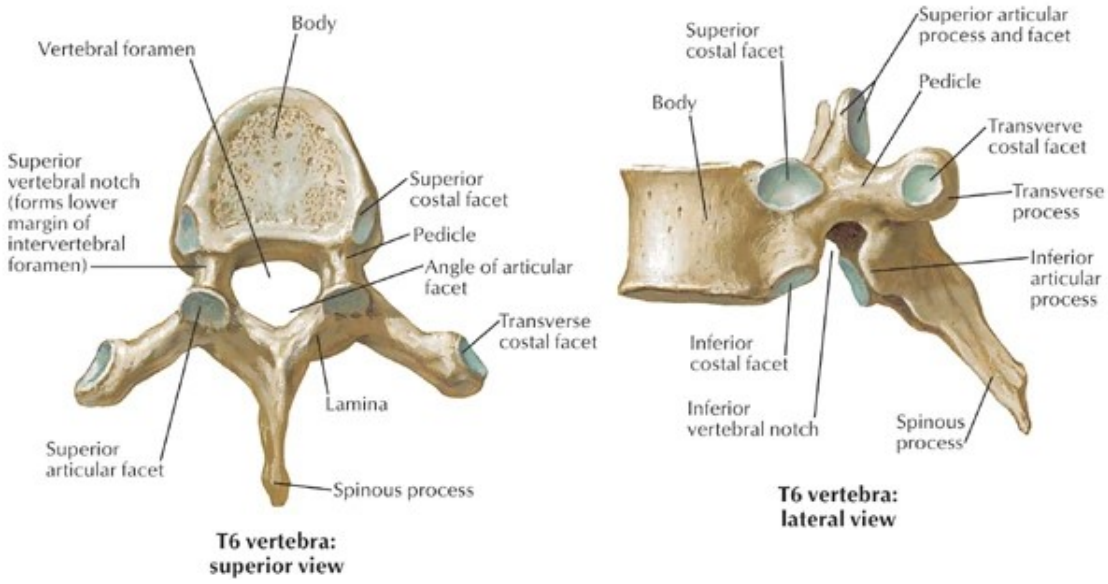

Figure 1.3: *Thoracic vertebra: superior and lateral view.*

The vertebrae facilitate various physiological movements, including torsion, anterior and lateral flexion of the head, trunk, and pelvis (motor function) [16]. Figure 1.4 illustrates the directions in which these physiological movements of the spine occur, along with the associated mechanical stresses.

Vertebral bodies consist primarily of trabecular bone, which is encased by a cortical shell. In nearly all physiological circumstances, in comparison with the posterior arch, it is the vertebral body that bears the heaviest loads and conveys them from the superior to the inferior end-plate of the vertebra. Indeed, the delicate bony lamellae within the cancellous tissue become more pronounced in lines perpendicular to the upper and lower surfaces due to increased pressure in this orientation [17]. Consequently, vertebrae are frequently subjected to compression testing

along the cranio-caudal direction. White and Panjabi summarized the compressive strength properties of cancellous bone in vertebrae, as measured on trabecular samples (see Table 1.1) [16].

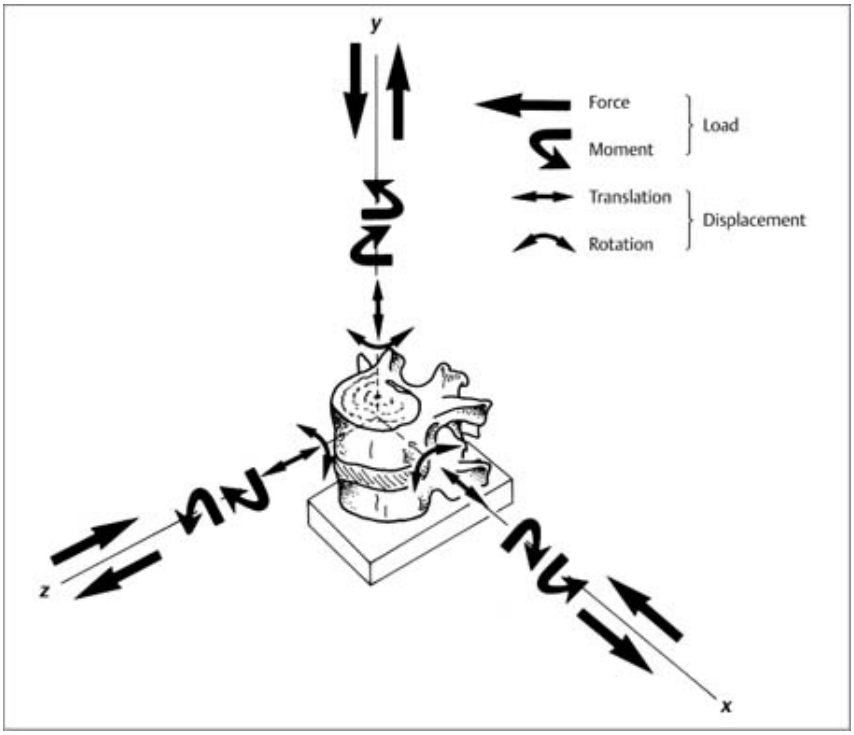

Figure 1.4: *Representation of physiological motions (3D coordinate system at the centre of the upper vertebral body of a motion segment) [16].*

Table 1.1: *Compressive Strenght Properties of Cancellous Bone of Vertebrae [16].*

Physical Property	**Magnitude**
Proportional-limit stress	1.37-4.0 MPa
Compression at proportional limit	6.0-6.7%
Modulus of elasticity	22.8-55.5 MPa
Failure stress	1.55-4.6 MPa
Compression at failure	7.4-9.5%

However, for mechanical characterization, it would be more appropriate to utilize a functional spinal unit (FSU), also referred to as a motion segment (see Fig. 1.2). The FSU represents

the smallest segment of the spine that displays biomechanical characteristics akin to those of the entire spine [16]. Using specimens composed of spinal segments allows for the replication of a more physiological condition, as they include not only the vertebra itself but also the surrounding soft tissues. It's worth noting that the distribution of load across the vertebral endplate is influenced by the anatomy and health of the adjacent intervertebral discs [20]. As previously mentioned, the various regions of the spine exhibit varying stiffness levels because they are subjected to different loads. Consequently, the mechanical properties will also differ depending on the region under consideration, as outlined in Table 1.2.

Regrettably, certain pathological conditions such as osteoporosis, primary spinal tumors, and spinal metastases have the potential to impair proper vertebral function. These conditions can diminish mobility, weaken tissues, elevate the risk of fractures, and alter the mechanical stiffness and strength of the entire spine.

Table 1.2: *Average Stiffness Coefficients and Flexibility Coefficients of a Representative Functional Spinal Unit in Different Regions of the Spine [16].*

Forces (N)					
	Tension	*Compression*	*Ant.Shear*	*Post.Shear*	*Lat.Shear*
	(+FY)	*(-FY)*	*(+FZ)*	*(-FZ)*	*(FX)*
Flexibility Coefficients (mm/kN)					
Cervical	19	5	20	19	19
Thoracic	1.3	0.8	9.1	9.1	9.1
Lumbar	1.3	0.5	8.3	5.9	6.9
Sacroiliac	6.4	3.4	9.3	5.3	2.6
Stiffness Coefficients (N/mm)					
Cervical	53	200	50	53	53
Thoracic	770	1250	110	110	110
Lumbar	770	2000	121	170	145
Sacroiliac	156	294	108	189	385

1.2 Spinal diseases

Spinal diseases and failures have a significant impact on a substantial portion of the population. They can arise from various causes and affect different components of the spine, including the vertebrae, intervertebral discs, and ligaments. The most common spine syndromes include scoliosis [21], hyper-kyphosis [22], and hyper-lordosis [23]. These syndromes can affect individuals of various ages, manifesting with a wide range of severity, symptoms, and consequences. They involve the degeneration of a segment of the spine, which can vary in extent, and disrupt the natural curvature of the spine. Different levels of these syndromes can lead to various issues, ranging from back pain to cardiovascular and respiratory problems, and even immobility.

Vertebrae, like other bones, can be affected by conditions such as osteoporosis and osteopenia. Osteoporosis involves a gradual loss of bone density [24], while osteopenia results in a reduction in bone mineral density [25], both of which weaken bone strength. These conditions increase the risk of vertebral fractures, as well as forearm and hip fractures, particularly in elderly individuals under normal daily loading conditions [26]. This heightened risk is often associated with complications affecting nearby nervous tissue.

Furthermore, the function of vertebrae can be compromised by metastasis, typically spread from prostate or lung cancers. In such cases, there is a significant reduction in bone mass within the vertebrae, consequently diminishing their strength [27]. Unfortunately, a well-defined surgical procedure for addressing this condition is lacking due to the limited number of cases and the ongoing advancements in medical technologies. This lack of a standardized approach increases the risks associated with this pathology and its profound impact on the quality of life. A comprehensive understanding of the human spine's anatomy is vital for medical professionals as it aids in the diagnosis and treatment of various spinal conditions and injuries.

1.2.1 Spinal metastases

The incidence of bone metastases varies significantly depending on the type of tumor (e.g., breast, prostate, etc.). Spinal metastases can manifest as lytic, blastic, or mixed lesions. From a

clinical perspective, lytic bone metastases are more prevalent and contribute to the majority of morbidity [2]. Lytic metastases are often referred to as bone-destructive [28] due to increased osteoclastic activity and/or an elevated number of osteoclasts. This activity compromises the highly organized trabecular structure of the vertebral body, leading to the destruction of trabeculae and the generation of micro-fractures [2].

The associated reduced mineralization and loss of structural integrity result in a weakening of the bone, reducing its load-bearing capacity. Consequently, this indirectly increases the risk of collapse [5]. In fact, previous research has already demonstrated how conditions like bone diseases [29] or aging [30] can lead to a decrease in bone mineral content. Even a small loss of bone tissue (e.g., 25%) can result in a significant reduction in vertebral bone strength (e.g., 50%) (see Fig. 1.5). This phenomenon is closely related to the load-bearing capacity of the vertical and horizontal trabeculae, which, in the presence of lytic metastases, are diminished and improperly oriented, consequently weakening the entire structural integrity.

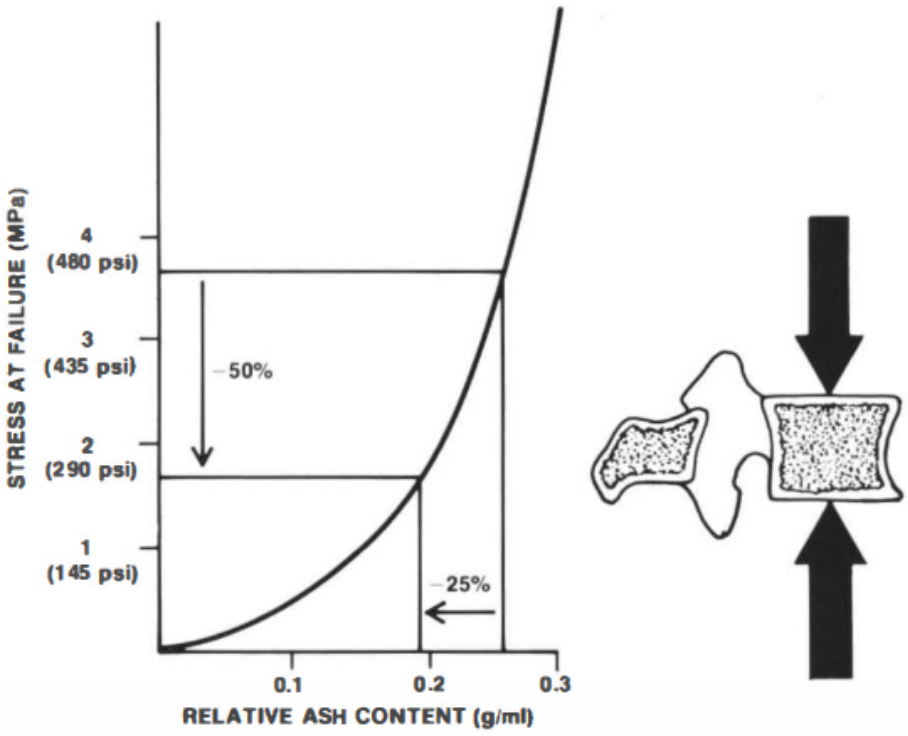

Figure 1.5: *Relationship between osseous tissue and vertebral strength [16].*

On the other hand, blastic metastases promote osteoblastogenesis [28]. This process leads to the formation of new bone tissue, which is mineralized but poorly organized, covering the normal trabecular structure and resulting in limited bone quality. By using quantitative computed tomography (qCT) or micro computed tomography (μCT) scans, it is possible to assess how both types of lesions alter the typical tissue distribution: lytic metastases create voids within the trabecular network and/or the cortical shell, while blastic metastases deposit an excess of bone tissue. Mixed-metastatic vertebrae exhibit characteristics of both lytic and blastic lesions (see Fig. 1.6).

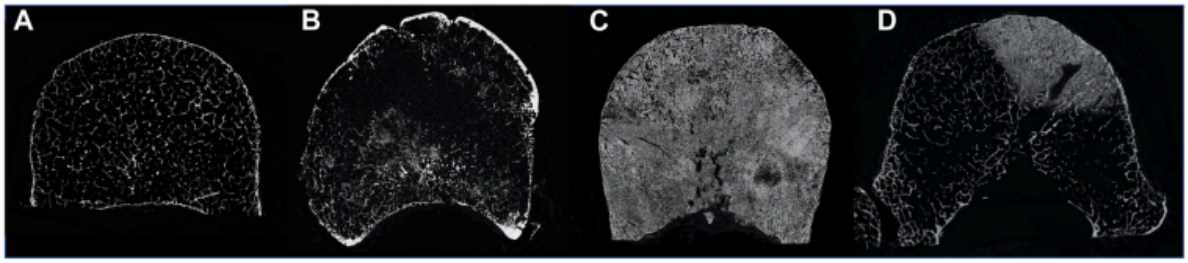

Figure 1.6: *Healthy (A), litic (B), blastic (C) and mixed (D) vertebrae scan with micro-CT [3].*

Due to the disrupted balance in the bone remodeling process and the consequent alteration in the distribution of bone tissue within the vertebra, both types of vertebral metastases often lead to mechanical instability of the spine.

1.2.2 Spinal Instability Neoplastic Score (SINS)

The likelihood of developing a fracture increases with the duration of metastatic involvement [31], and it is also influenced by the location and size of the metastases [32]. While radiation is effective for local tumor control, it does not impact spinal stability [33]. Therefore, to prevent fractures, stabilization interventions are required, including brace application, percutaneous cement injection, pedicle screw augmentation, or open surgery. These surgical treatments are challenging and pose risks [31], potentially confining patients to bed rest and exacerbating pain and other symptoms [34]. Thus, excessive protection may lead to unnecessary constraints and a reduced quality of life, while inadequate treatments can result in fractures and spinal deformities with potential neurological consequences [1]. Therefore, predicting the risk of

fracture for each specific patient holds significant clinical relevance, as it could enable the implementation of preventive measures that enhance the patient's quality of life.

In the past, predictions of fractures in patients with cancer and/or bone metastases were primarily based on expert opinions derived from clinical experience and descriptive studies. Over the years, several scoring systems have been developed as prognostic tools for surgeons. In contemporary clinical practice, a widely adopted classification scheme is used to assess the mechanical instability of the spine and, consequently, the risk of fractures.
The Spinal Instability Neoplastic Score (SINS) is a scoring system introduced in 2010 by the Spine Oncology Study Group (SOSG) [1]. It relies on clinical factors (patient-reported pain) and objective radiological criteria. SINS aids healthcare professionals, including surgeons, oncologists, radiologists, and orthopedic specialists, in devising tailored treatment plans. It helps identify patients who require surgical evaluation [5] and may derive the most benefit from surgical intervention, as well as those who may not tolerate such invasive procedures or might benefit more from alternative therapies like chemotherapy or radiotherapy. SINS evaluates spinal instability by assessing and assigning scores to six variables: lesion location, pain characterization, type of bony lesion, radiographic spinal alignment, degree of vertebral body destruction, and involvement of posterolateral spinal elements (see Figure 1.7).

The scores for each variable are summed to calculate a final score, which ranges from a minimum of 0 to a maximum of 18. A score of 0 to 6 indicates stability, a score of 7 to 12 suggests indeterminate (possibly impending) instability, and a score of 13 to 18 indicates instability. When the SINS score exceeds 7, it is recommended to seek a surgical consultation [5]. One of the most crucial challenges is that no clear guidelines are provided for patients with a score between 7 and 12 (potentially unstable), leaving clinicians to rely on their personal experience when making decisions [35]. Furthermore, there is a poor correlation between the SINS score and biomechanical outcomes in the case of metastatic vertebrae [36].

[1]The SOSG is an international group of 30 spine oncology experts and thought leaders from North America, Europe, South America, and Asia who meet biannually to discuss research, assess the best evidence for current practices, and formulate clinical trials to advance the field of spine oncology

Component	Score
Location	
Junctional (O-C2; C7-T2; T11-L1; L5-S1)	3
Mobile spine (C3-6; L2-4)	2
Semirigid (T3-10)	1
Rigid (S2-S5)	0
Mechanical pain	
Yes	3
No	2
Pain free lesion	1
Bone lesion	
Lytic	2
Mixed (lytic/blastic)	1
Blastic	0
Radiographic spinal alignment	
Subluxation/translation present	4
Deformity (kyphosis/scoliosis)	2
Normal	0
Vertebral body collapse	
>50% collapse	3
<50% collapse	2
No collapse with >50% body involved	1
None of the above	0
Posterolateral involvement	
Bilateral	3
Unilateral	1
None of the above	0

[a]Data adapted from Fischer et al.[9]

Figure 1.7: *Elements of SINS [5].*

Palanca et al. demonstrated that in two out of three considered cases, SINS did not indicate the need for spinal stabilization, assigning low scores (e.g., 4-6), while biomechanical tests revealed a high risk of fracture in these patients. According to Costa et al., SINS does not correlate with the compressive strength of vertebrae with lesions because there is no observed correlation between the scoring system and mechanical properties estimated from computational models. Nevertheless, mechanical properties, such as bone strength [37], are associated with the presence of metastases. Load distribution and strain patterns can change from a healthy state to a metastatic condition. Indeed, load transfer between vertebrae depends on factors such as the quality of bone tissue, intervertebral discs, and the presence, size, and shape of os-

teophytes [38]. Therefore, gaining a deeper understanding of the mechanical behavior of bone tissue affected by metastatic disease could help identify sites and mechanisms of fractures.

1.2.3 Mechanical characterization of the spine and metastases: state of the art

In 1997, Taneichi and colleagues [39] reported that the mechanical properties of the metastatic spine and the mechanisms of collapse were still unknown. Today, the scientific literature widely discusses the characterization of the mechanical properties of the spine in various conditions, including physiological states, the presence of pathologies like vertebral metastases, or post-treatment effects. Notably, the measurement of spinal strain fields is employed to investigate how metastases affect bone failure mechanics, aiding in predicting vertebral fractures. In vitro experiments provide a means to measure mechanical and apparent properties (such as stiffness, strains, failure strength, and mode of failure) of the spine by applying simplified loading conditions to specimens, often axial compression [40].

In vitro tests must meet two key criteria: repeatability, which ensures a consistent response when the same input is applied multiple times, and reproducibility, ensuring the same output when tests are conducted under different instances but following the same protocol. This enables the comparison of results from identical tests performed on different specimens, such as two vertebrae, one with metastases and one without. Due to the challenges in obtaining human cadaveric specimens, which are subject to strict ethical regulations, researchers often turn to animal models within the food chain.
However, notable anatomical differences exist between quadrupeds and humans, including size dimensions (porcine vertebral bodies are smaller and have thicker cortical shells) and microstructure (porcine vertebrae are denser than human ones). Additionally, bone structure and mechanical properties, such as range of motion and stiffness, differ between the two [41].

Whether dealing with human or animal specimens, the choice of specimen type is typically based on the study's objectives (as depicted in Fig.1.8). Specimens consisting of spine

segments (series of adjacent vertebrae) are valuable for characterizing kinematics and spinal instability. This specimen type replicates a more physiological condition by including not only the vertebra itself but also the surrounding soft tissues. Conversely, when the goal is to study the structural properties of an individual vertebra, specimens containing a single whole vertebra or just the vertebral body, with or without end plates, are employed. In this scenario, loads are applied directly to the vertebra's surface or end plate, sometimes embedded in polymethyl-methacrylate (PMMA). It's worth noting that the absence of adjacent intervertebral discs in this setup may limit the physiological relevance of the results due to artificial failure mechanisms [20].While trabecular and cortical core specimens provide insights into the local mechanical properties of bone tissue, they do not fully represent the behavior of the entire vertebra [40].

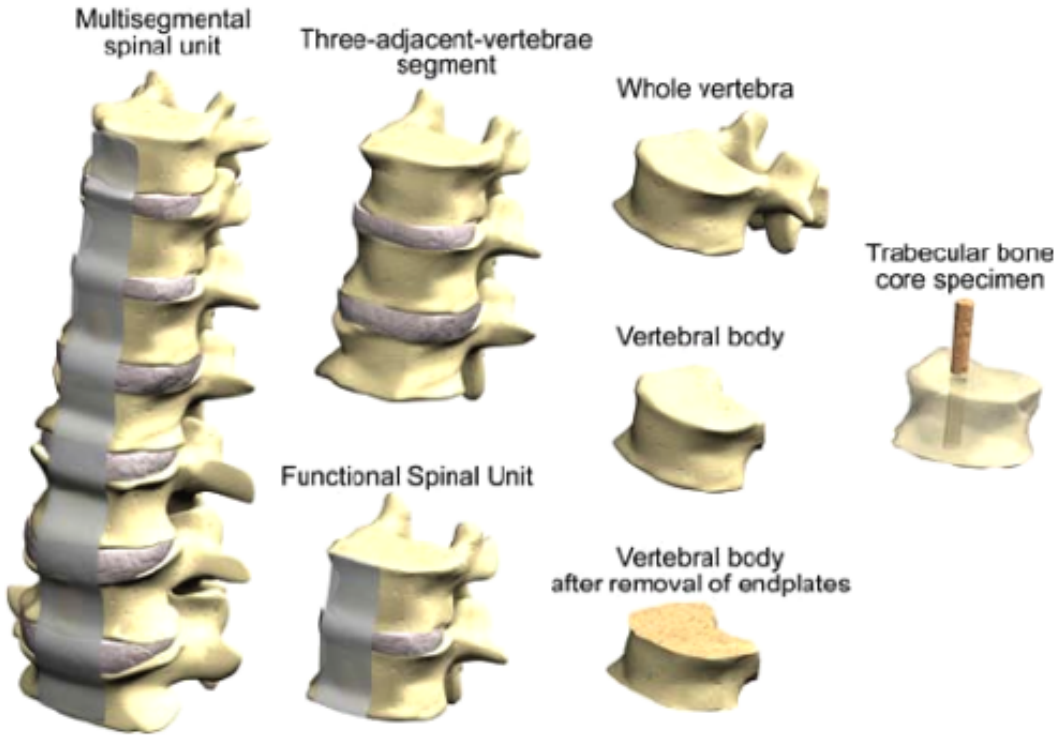

Figure 1.8: *Main types of specimens used in vitro testing [40].*

Additionally, researchers must carefully choose the most appropriate loading conditions. Spine segments can experience various types of loads, such as compression, torsion, flexion, extension, and lateral bending, alone or in combination. However, the precise extent of these

loads' physiological relevance remains uncertain. While mathematical models offer a non-invasive means to predict forces and moments, in vivo tests are generally considered more reliable than in vitro ones, as they can account for muscle structures and neuromuscular control [16].

Regarding the mechanical characterization of bone metastases, recent studies [3] have highlighted the significant role of the type, size, and location of metastases in determining the mechanical response of metastatic vertebrae. Specifically, the type of metastatic tissue (i.e., lytic, blastic, or mixed) has emerged as the most crucial factor for predicting variations in vertebral strength. Interestingly, despite vertebrae with lytic metastases exhibiting a similar elastic modulus to healthy ones, their strength was found to be lower, thereby increasing the risk of fracture. In contrast, vertebrae with blastic metastases exhibited higher strength, despite their elastic modulus being lower than that of healthy vertebrae. This study demonstrated that in most cases, metastatic vertebral bodies fail similarly to those without lesions, with direct involvement of the endplates or the tissue nearby.

1.3 3D Printing

3D printing is a form of additive manufacturing, that operates on the principle of layered manufacturing, where materials are deposited layer by layer to build objects. This process involves the creation of three-dimensional (3D) objects by adding materials successively in 2D layers. 3D printing offers numerous advantages compared to traditional manufacturing methods, including the capacity to fabricate objects with intricate internal structures, enhanced versatility, customization options and reduced space requirements. This technology enables the rapid production of components with complex shapes by precisely accumulating material based on a computer-aided design (CAD) model.

A three-dimensional model of the object, created using CAD software, is converted into an STL file. Subsequently, using a slicer (slicing software), the structure is divided into digital layers, and a G Code is generated (a code that defines the commands to be sent to a numerical control device). These commands are then transferred to the 3D printer using custom machine software. Typically, the printer comes with integrated software that handles both the slicing

and the code generation automatically.

When integrated with medical imaging, 3D printing unlocks new possibilities in the field of healthcare. Clinical applications of this emerging technology are actively being explored across various medical disciplines. The capability to generate 3D models from patient data empowers physicians to create customized prosthetics and implants, gain clearer insights into complex pathologies and enhance medical education for trainees like never before [42].

The process of generating 3D objects from imaging data generally follows these steps:

1. acquisition of image data (CT or MRI);
2. extraction of the chosen regions of interest termed “segmentation”;
3. transformation of the data from set of images to a 3D triangular mesh;
4. transfer of the data to a 3D printer for production, from CAD to the 3D model, involves passing through the STL file, slicing, and G Code generation.

A typical sequence of this process can be seen in Fig.1.9. These steps are each discussed in detail in the following sections.

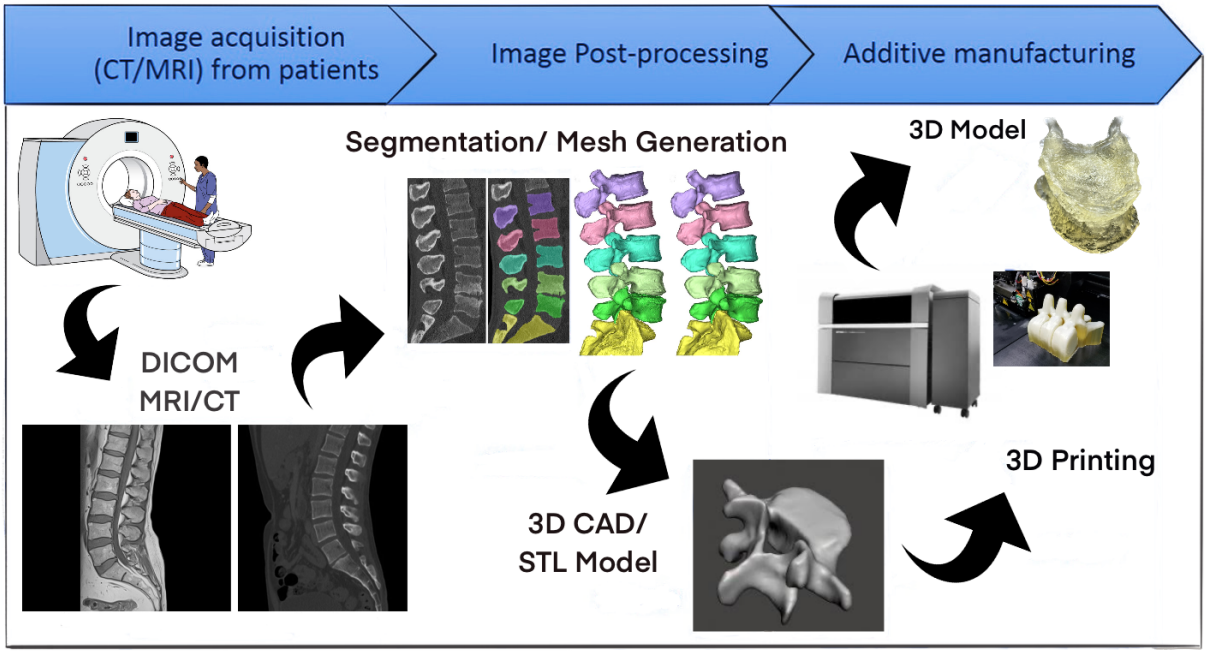

Figure 1.9: *Flowchart of creating a 3D printed model from medical images.*

1.3.1 Image acquisition

The initial step in creating 3D printed models from medical imaging involves obtaining usable data. Typically, data for generating medical models are acquired using computerized tomography (CT) or magnetic resonance imaging, although other modalities like ultrasound can also be utilized.

The selection of image data is crucial, as low-resolution images can lead to disparities between the generated model and actual anatomy. In contemporary clinical practice, image acquisition can achieve ultra-high spatial resolution (ranging from 250 to 600 microns) with excellent contrast quality. Most imaging techniques are non-invasive, enabling the exploration of internal structures within a patient's body that are concealed by skin and bones.

Clinical Images are stored ad DICOM (Digital Imaging and Communications in Medicine), format that includes pictures, images and study information [43].

The most commonly used medical imaging method for bone structure is computed tomography (CT), a medical imaging technique that uses X-rays to create detailed cross-sectional images of different parts of the body. CT scans rely on pixel intensities that directly represent tissue density, making them suitable for distinguishing structures with both high density (like bones) and low density (like lungs). During a CT scan, the patient lies on a table that moves through a circular scanning device. Multiple X-ray images are taken from different angles and then combined to create three-dimensional images using backprojection algorithms.

The Hounsfield Unit (HU) scale measures the radiodensity of materials based on their X-ray absorption properties. For example, high-density tissues like bone appear bright (white) due to their strong X-ray absorption, while soft tissues allow more X-ray penetration, resulting in darker appearances (Fig.1.10). CT is widely used to create 3D anatomical models because it is easy to process the collected data.

However, CT has its limitations, such as sensitivity to patient movement, which can make it challenging to define morphological boundaries due to the grayscale scales in the images. Nonetheless, software reconstruction can help mitigate these issues in some cases.

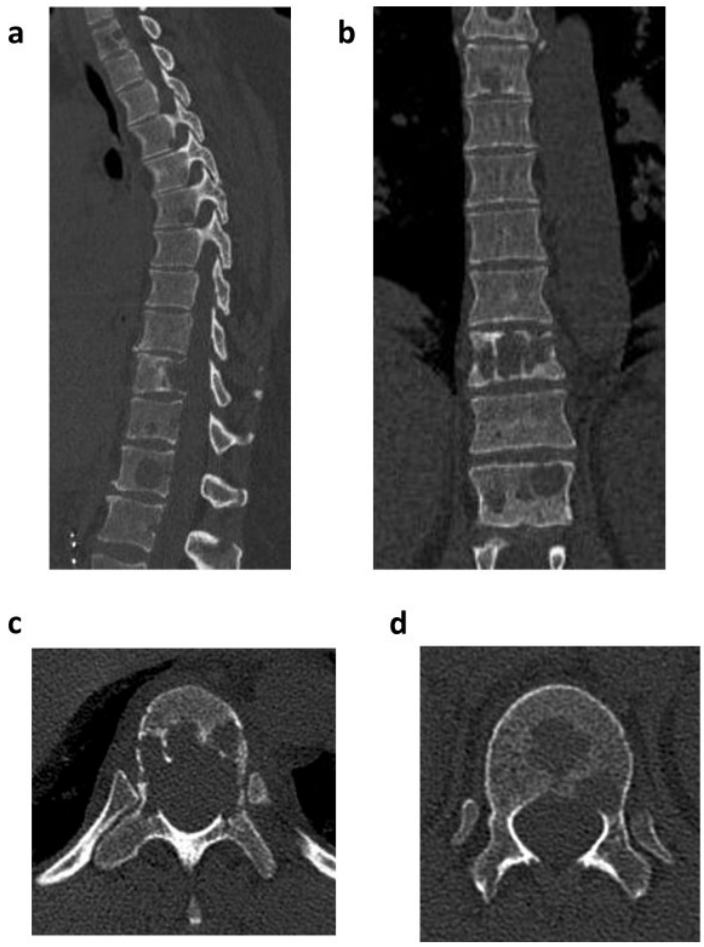

Figure 1.10: *Computed tomography (CT) of the thoracic spine [44]. Sagittal (a) and coronary (b) CT scans revealing multiple osteolytic lesions. (c) Axial CT image of T10 depicting destruction of the rear edge without spinal obstruction. (d) Axial image of the CT scan of T12 showing osteolytic lesions centrally and in proximity of the left pedicle.*

Micro-computed tomography (micro-CT) is an advanced imaging technique that operates on a miniature scale, providing significantly enhanced resolution compared to standard hospital CT scans. It enables imaging of samples with pixel sizes as minuscule as 100 nanometers while accommodating objects as large as 200 millimeters in diameter. Micro-CT delivers high-resolution 3D imaging that surpasses the capabilities of any other non-destructive technology. This technology allows for the examination of the internal structures, such us trabecular bone (Fig. 1.11), and biological specimens without the need for sample dissection, preserving them for future investigations. Micro-CT scanning offers scientists a unique opportunity to explore

sample morphology and investigate properties such as porosity, bone thickness, volume fraction, defect analysis, density, particle size, voids, fiber orientation, and more.

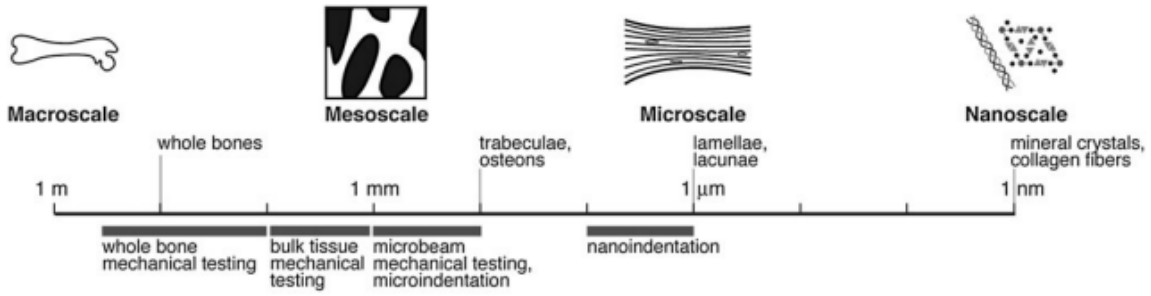

Figure 1.11: *Hierarchical bone structure schematically divided on a logarithmic scale with differentiation of mechanical characterization techniques for each parameter.*

1.3.2 Segmentation

Image segmentation is a crucial step in creating precise 3D anatomical models customized for individual patients, and it plays a pivotal role in numerous clinical applications. The primary objective of image segmentation is to divide a volumetric medical image into distinct regions, typically corresponding to organs or structures of interest. Various image segmentation techniques are available, each with its own advantages and disadvantages. However, there is no one-size-fits-all segmentation technique suitable for all images and applications. These methods operate on the principle that different tissue types exhibit specific ranges of pixel intensities, allowing for tissue differentiation and boundary identification.

A wide range of software tools is capable of performing image segmentation, ranging from versatile commercial platforms like Mimics, which include integrated physics simulations, to open-source solutions such as 3D Slicer, designed for specific organs or applications. Segmentation algorithms for grayscale images generally fall into one of two categories based on intensity value properties: discontinuity, which involves partitioning an image based on abrupt changes in gray levels, and similarity, which entails dividing an image into regions that share similarities. Common image segmentation techniques include thresholding, edge detection, and region growing (Fig.1.12).

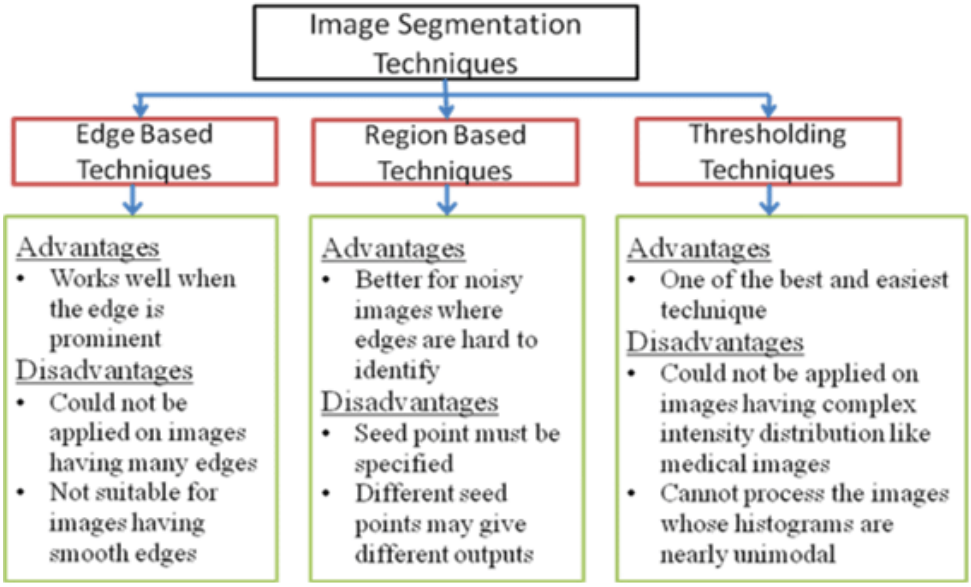

Figure 1.12: *Classical Image Segmentation Techniques with their advantages and disadvantages[45].*

Thresholding, the simplest method, involves dividing an image into a binary representation of the segmented areas. This process distinguishes pixels of interest by comparing each pixel's intensity value to a predefined threshold. Pixels with intensities higher than the threshold are set to one value, typically white, while those with intensities lower than the threshold are set to another, typically black.

Edge pixels represent locations where the intensity of an image changes suddenly, forming sets of interconnected pixels known as edges. Edge pixels can be detected using local image processing techniques known as edge detectors. Edge detection is commonly used to segment images based on abrupt local intensity changes.

Region growing is another technique that groups pixels or sub-regions into larger categories based on predefined growth criteria. The fundamental approach involves initiating the process with a set of "seed" points and expanding regions by incorporating neighboring pixels that exhibit predefined properties similar to the seed.

Automated segmentation of medical images is a valuable tool for streamlining time-consuming tasks, with the goal of achieving faster and, ideally, more reliable results than manual procedures. However, it remains a challenging task due to the inherent complexity of medical images, which often suffer from issues such as tissue type overlap, biased intensity, presence

of artifacts, and proximity of gray values for different tissues.

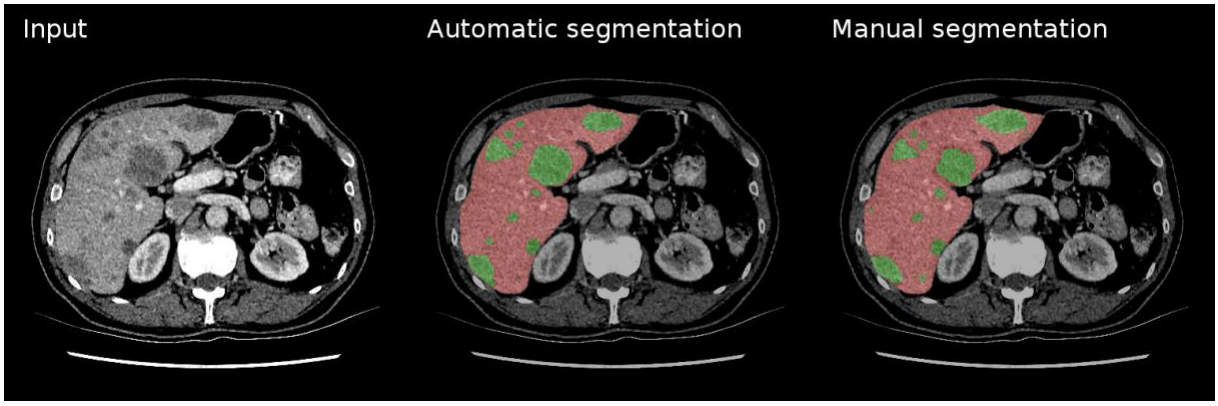

Figure 1.13: *Example of tumor segmentation.*

1.3.3 Mesh generation

After completing the segmentation, a surface is extracted from the volumetric data by converting the data from voxels into a mesh composed of a series of geometrical facets. This can be achieved using automated surface rendering tools [46].

The transformation from a voxel to a polygonal model results in a smoother surface but represents an approximation of the original image. Additional adjustments can be made manually or automated algorithms may be employed to smooth out artifacts. Various computer-aided design tools are available for this purpose, allowing for extensive mesh manipulation and refinement. However, the primary reasons for post-processing the mesh segmentation are as follows:

- Repairing: Errors and discontinuities that may occasionally arise during the image segmentation and exporting process need to be corrected before printing.
- Smoothing: 'Staircasing errors' that result from the resolution of the original medical image can be reduced by smoothing the surface of the mesh model.
- Appending: The segmentation often constitutes only one component of the final model. To make the model usable, it is often necessary to combine it with other structures or remove unnecessary parts from the segmentation.

The segmentation and mesh generation process can introduce significant inaccuracies between the original DICOM data and the final 3D generated model. It is crucial to compare the region of interest in the processed data with the original unprocessed DICOM data at each step to ensure that it remains an accurate anatomical representation. Finally, the data is saved in a standard tessellation language (STL) file format.

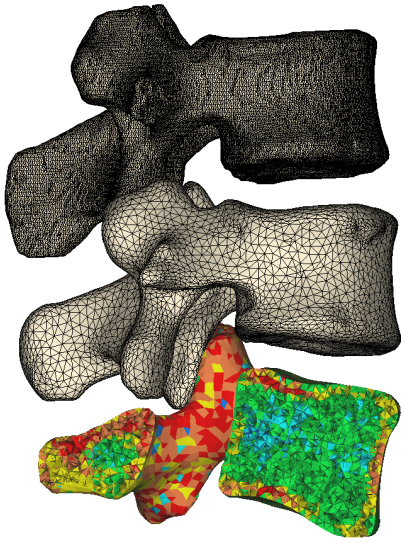

Figure 1.14: *Example of 3D meshing models of human vertebrae.*

1.3.4 3D Printing Technologies

Creating three-dimensional models offers both visual and tactile representations of anatomy, enhancing preoperative planning and contributing to the precision and accuracy of complex medical procedures.

Surgical planning with 3D printing models have garnered significant attention within the field of orthopaedics, leading to substantial progress in the preparation for surgical procedures. It has been observed that 3D models enable surgeons to visualize anatomical structures in three dimensions, facilitating the planning and execution of patient-specific complex surgeries. Recent advancements in 3D printing technology have introduced new methods that enable the utilization of various materials, ranging from synthetic polymers to metal alloys.

The choice of a 3D printer depends on the intended application and several factors should be taken into account, including cost, accuracy, speed, and the availability of printing materials

[47]. Various 3D printing technologies are available, each possessing its unique characteristics. In Figure 1.15, the different type of 3D printing technologies in medical applications are summarized.

Technology	*Pros*	*Cons*	*Main applications*	*Layer thickness*
Material extrusion (FDM)	• Strength, stability, and durability of the final part • Better mechanical properties • Use of common thermoplastics • Easily removable soluble supports • Easy-of-use	• Visible lines of the layers on the side walls • Waterproofing required in some applications • Post-finishing of the printed objects to remove the staircase effect	• Musculoskeletal 3DP • Patient-specific guides and surgical tools • Anthropomorphic phantoms for medical imaging • Customized prostheses • Radiotherapy mask, models, and bolus	0.1 – 0.4 mm
Material jetting (PolyJet)	• Smooth surfaces and fine details • Good appearance and consistency of the final product • Easy printing of flexible materials • Multi-material 3DP	• Greater weakness of printed parts • Soluble supports removable with pressurized waterjet • High costs of 3D printers, materials, and maintenance	• Pre-surgical planning and education • Customized implants and prostheses • Surgical guides and tools • Digital dentistry	up to 16 μm
Vat photopolym. (SLA/DLP)	• High printing speed • Minimized staircase effect • Isotropic properties (in DLP) • Dimensional stability and durability • Low and high temperatures resistance	• Lattice support structures need to be manually removed • Supports could leave marks on the surface and create uneven surfaces • Models can contain only a single material (colour/properties)	• Bone applications • Fabrication of advanced and functional constructs • Scaffolds for cells • Personalized 3DP drugs • Radiotherapy mask, models, and bolus • Digital dentistry	0.02 – 0.2 mm
Binder jetting	• Color print heads or binders • Support structures are not needed • The model is continuously supported by unbonded powder	• Inability to print translucent or flexible models • Rough in surface finish • Difficulties in removing dust from convoluted hollow models	• Models for anatomic visualization with color-coded anatomy • Metal parts especially in implants and tools • Instruments and parts for medical devices	0.05 – 0.1 mm
Power bed fusion (SLS)	• Non-metal materials do not require support structures • Biocompatible synthetic polymers (e.g., nylon, polyether ether ketone (PEKK)) and metals (e.g., titanium and cobalt-chrome alloys) that are sterilizable and can be safely implanted	• Low printing speed • Expensive materials • Less accuracy than in vat and jet techniques • Difficulties in removing unsintered powder remaining in printing model cavities (this could affect biocompatibility and sterilization)	• Implants to promote osseointegration • Surgical instruments and guides • Patient-specific temporary devices (such as splints) • Customized implants and prostheses • Digital dentistry	0.02-0.15 mm

Figure 1.15: *Overview of the most important 3D printing technologies with medical applications [48].*

These 3D printing technologies can be broadly categorized into three groups: extrusion printing, photopolymerization, and powder-based printing [49].

Extrusion printing, exemplified by Fused Deposition Modeling (FDM), involves melting and depositing material through a nozzle to construct the desired shape.

Photopolymerization relies on selectively curing liquid polymers, employing UV light. Prominent examples of this method include Stereolithography (SLA) and Digital Light Processing (DLP), which cure plastic within a bath. Alternatively, photopolymer can be sprayed onto the print in thin layers and subsequently cured, known as Photopolymer Jetting (PolyJet).

In powder-based techniques, a powdered material is fused together, achieved either by using a liquid binding agent (Binder Jetting, BJ) or by applying heat to fuse the particles (Selective Laser Sintering, SLS).

Photopolymer jetting, also known as PolyJet 3D printing, falls within the realm of DLP technology. This advanced additive manufacturing method involves depositing material in the form of droplets to create thin layers that are then cured to form three-dimensional objects. It is controlled both thermally and physically. While PolyJet printers are indeed one of the pricier choices in the additive manufacturing industry, this technology manages to strike an impressive balance between resolution, speed, and material quality.

The PolyJet technology consists of a build platform where the print head moves back and forth along the X and Y axes, depositing thin layers of thermoplastic resin, as shows Fig. 1.16. An ultraviolet (UV) chamber contains a UV lamp that cures and hardens these layers using UV light.

When there are overhangs or complex shapes that require support, the 3D printer deposits support material. At the end of the process, this support material can be easily removed by hand, with water, or in a solution bath. PolyJet printers are capable of quickly producing complex components, making them ideal for creating realistic prototypes and components. PolyJet additive manufacturing offers a wide range of colors and materials in a single end-use product. This method provides flexibility in selecting materials with high tensile strength, fatigue resistance, and torsional strength.

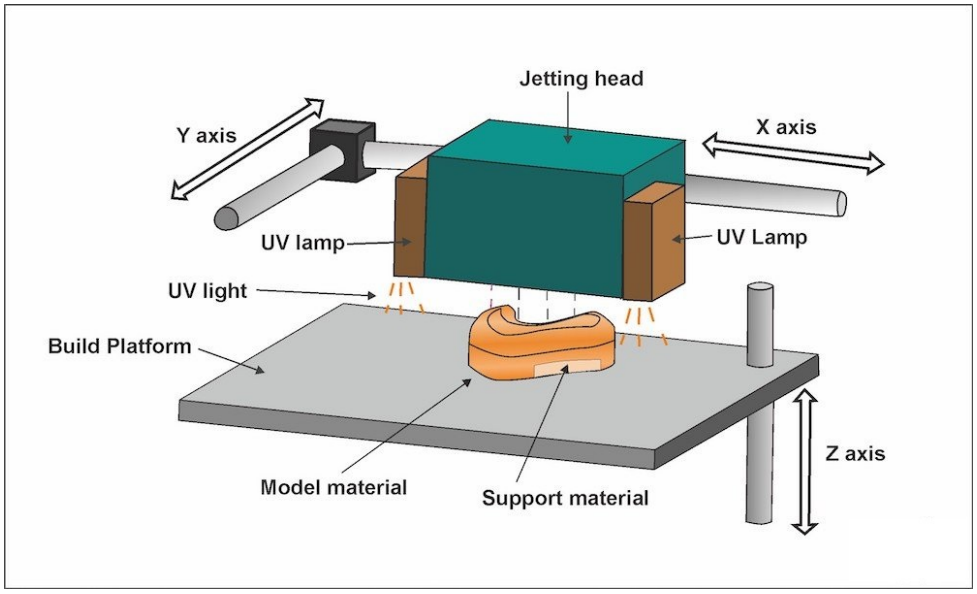

Figure 1.16: *Polyjet 3D Printing.*

The models and objects are ready for handling or use directly from the PolyJet 3D printer, without the need for additional treatments. This technology provides excellent detail, smooth surfaces, and high precision. It allows for the construction of models using various plastics and rubber with different hardness levels. Layers as thin as 16-32 µm provide nearly absolute precision (±0.1 mm) with excellent surface quality, enabling various applications such as co-printing, the use of completely transparent materials, sterilizable materials, and biocompatible materials. PolyJet technology is particularly suitable for producing highly detailed models useful for fit testing, dimensional checks, and ergonomic testing [50].

1.4 Aim of the study

The aim of the project is to replicate the mechanical behavior of ex-vivo vertebrae and explore the feasibility of creating dependable replicas of both healthy and diseased vertebrae using 3D printed synthetic models.

To achieve this goal, various materials and setups were examined, and specific sub-objectives were established:

- Characterize the mechanical properties of 3D printable materials.

- Evaluate the mechanical characteristics of 3D-printed models generated from different medical imaging sources.
- Characterize models based on anatomy, morphology and diseases, identifying differences and similarities among them.
- Compare the 3D synthetic models with ex-vivo specimens.

This work introduces an innovative approach through three fundamental elements:

1. The development of synthetic anatomical models, particularly vertebrae and metastases, using digital anatomy printing technology.
2. The execution of mechanical tests to validate their fidelity to real ex vivo models.
3. Advancement of research in the domain of fracture risk prediction from bone metastases by applying these novel paradigms to standardize and customize scenarios.

The project enhances the methodologies and procedures for testing and, consequently, provides a comprehensive characterization of spinal biomechanics.

Chapter 2

Materials and Methods

This study is based on CT and MicroCT data obtained from a human spine affected by vertebrae with bone metastases. The specimen was acquired through an ethically approved international donation program known as the Anatomy Gift Registry in the USA. Details about the donor are summarized in the table 2.1.

The specimen in question is a thoracic multi-vertebrae segment (T5-T8) extracted from the spine. It includes a healthy vertebra, referred to as the control, a metastatic vertebra, and two others at the extremities. It is reasonable considering that the control and the metastatic vertebrae, being adjacent, were subjected to similar loads. This assumption allows us to directly compare the stress-strain fields of these two vertebrae and evaluate the potential effects of the metastases.

Table 2.1: *Donor details.*

Speciment #766_T5T8

Cancer	Adrenal	**SINS**	3
Sex	M	**Control level**	T7
Age	81	**Metastasis**	T6
Height (cm)	182	**Type of metastasis**	lytic
Weight (kg)	77		

2.1 Workflow

2.1.1 Segmentation CT images and MicroCT

The segmentation process utilizes Mimics 25.0 software, developed by Materialise NV in Leuven, Belgium. Materialise Mimics is specialized image processing software designed for 3D design and modeling. It generates 3D surfaces from stacks of 2D images, serving various engineering applications, including medical, dental, and additive manufacturing. This software has also obtained CE and FDA 510K premarket clearance. In fact, the Medical License for the software is sold as a medical device and conforms to ISO 13485 standards.

The images are stored as DICOM files, which consist of a header and the actual image data, and were obtained using both clinical CT and micro-CT scanners. These two types of scanners have different imaging parameters (summarized in table 2.2), with micro-CT providing higher resolution and detail quality.

Table 2.2: *DICOM parameters of medical images.*

	Value	
Description	*CT*	*μCT*
Width	512 px	948 px
Height	512 px	1132 px
Pizel size	0.217 mm	0.039 mm
Field of view	110.10 mm	44.148 mm
Number of slice	124	662
Slice Increment	1 mm	0.039 mm
Slice Thickness	1 mm	0.039 mm

Once the imaging parameters were noted, we began the segmentation process. Segmentation of a Region of Interest (ROI) involves creating a mask through thresholding, which means generating a mask that includes all pixels within a specific Hounsfield (HU) range. By setting upper and lower threshold values, the pixels falling within the designated range form a single

mask. Each type of tissue has its typical range of Hounsfield units, but these ranges can vary between images. In this case, we defined different ranges for trabecular bone, cortical bone, and metastases, as illustrated in figures 2.1- 2.2. Each mask was saved with a specific name corresponding to its position within the structure.

After thresholding, region growing was applied to separate masks into distinct parts and to eliminate isolated pixels. Subsequently, manual editing operations were performed to enhance critical points in the images and achieve the most accurate representation possible. When the geometry of the mask has reached a fluctuating level of accuracy, we proceeded to create the 3D portion, incorporating smoothing and wrapping operations to achieve a more homogeneous structure. At the end of the process, the STL file was exported, which would be introduced into the printer software.

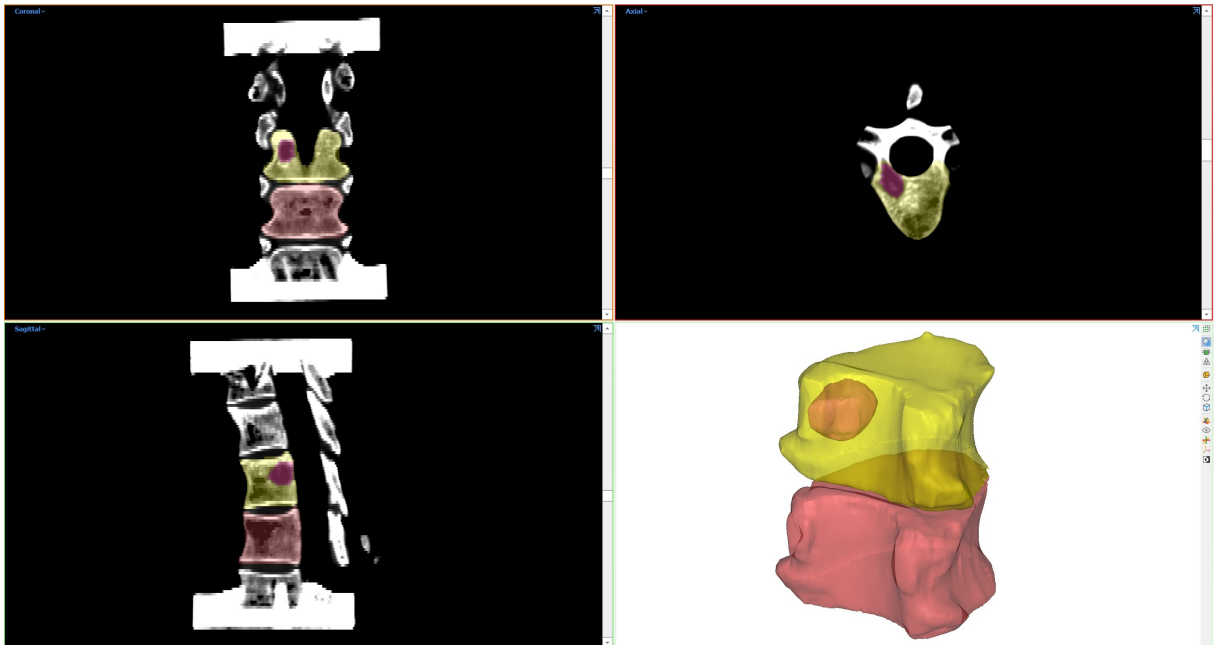

Figure 2.1: *Screenshot of Mimics application, performing Segmentation of Healthy and Metastatic from Ct scan. In this case there is only one mask for both cortical and trabecular bone, the other mask is for the metastasis. HU range for bone [100-1500], HU range for metastasis [10-150].*

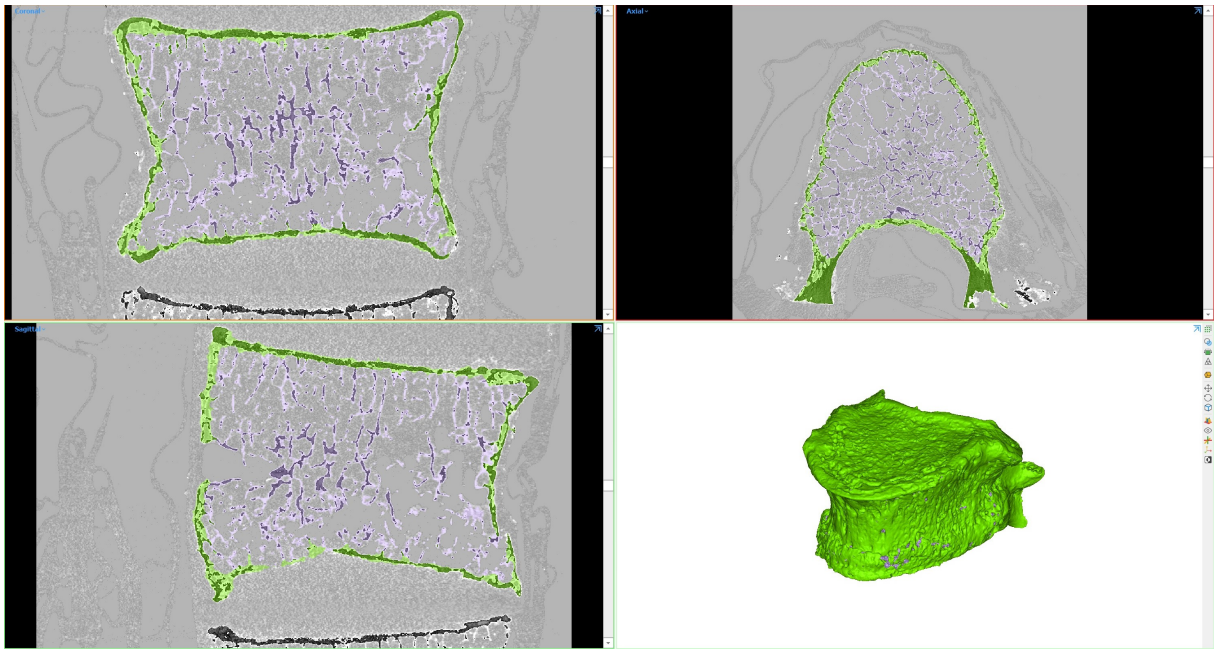

(a) *Healhty μCt, HU range for cortical and trabecular bone [1250-65535].*

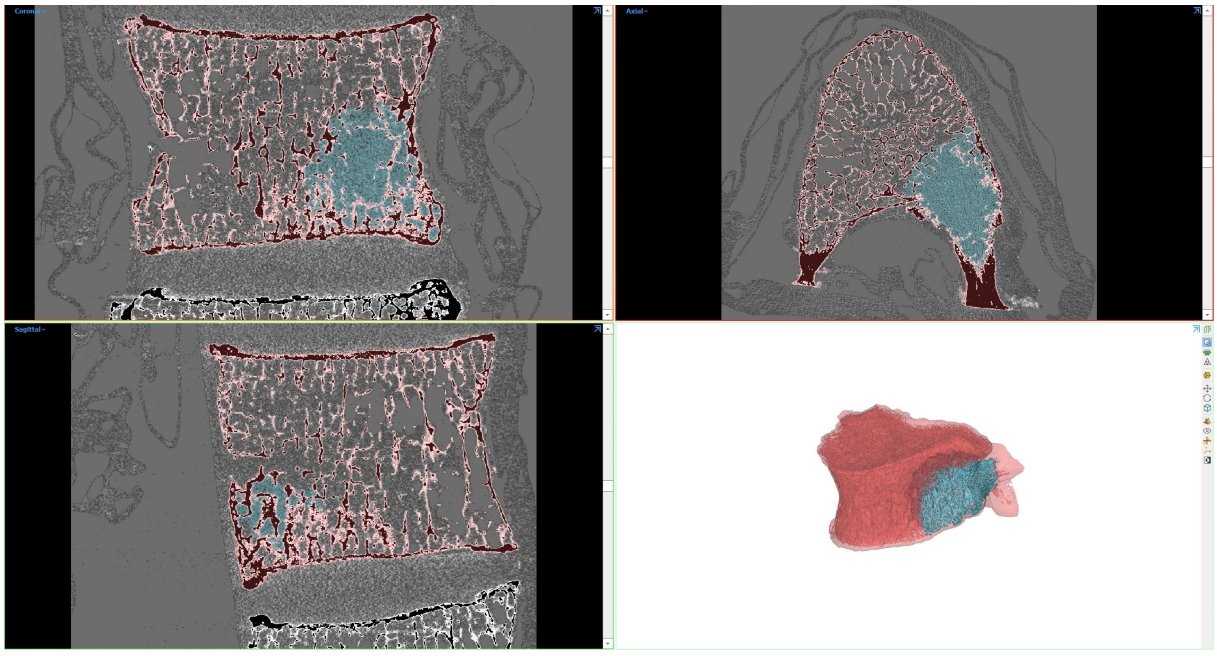

(b) *Metastatic μCt, HU range for cortical and trabecular bone [1250-65535], HU range for metastasis [35918-44898].*

Figure 2.2: *Screenshot of Mimics application, performing Segmentation for μCt scans. In this case trabecular and cortical bone have different masks, beyond the mask of the metastasis.*

2.1.2 Digital Anatomy Printer - Stratasys J850

The J850 PolyJet is a specific type of material jetting 3D printing technology by Stratasys, which was utilized in the production of all the samples. This printer is equipped with eight lines arranged in four physical inkjet heads (Figure 2.3), linked to material print cartridges. Two UV light sources are employed to cure the photosensitive resin as a roller systematically traverses the layers of the samples. It is worth noting that the printer includes a ventilation system to prevent the overheating of the UV lamps and can print on a build plate with dimensions of up to 490 x 390 x 200 mm.

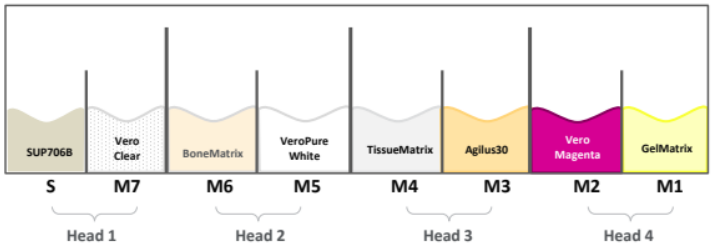

Figure 2.3: *The arrangement of digital anatomical materials in the printer heads.*

One of the standout features of this printer is its ability to simultaneously print with seven materials, in addition to support material. Each combination of materials yields a distinct set of properties, including physical, mechanical, shades and tones, which differ from those of the parent materials. To maintain optimal performance, the jetting nozzles are cleaned with isopropyl alcohol after each printing batch to prevent material build-up.

This printer is particularly renowned for the vibrancy and consistency of its materials, making it an excellent choice for surgical planning and the production of biomedical materials with minimal issues. Its capabilities allow for the creation of models featuring intricate details and fine structures that closely resemble actual human tissue, providing a genuine haptic feedback experience. Furthermore, it accomplishes all of this in a single printing operation, requiring minimal to no post-printing finishing steps such as painting, sanding, or assembly. Complex models that encompass both bone and soft tissue, along with ligaments and nerve roots, can be produced, and bone density can be varied to mimic healthy and osteoporotic bones.

The printer is operated using GrabCAD Print software, which loads the stereolithography (STL) files and assigns the printing material to each sample. It's important to note that PolyJet 3D printers exclusively work with Stratasys PolyJet materials, the company offers a wide range of materials, including biocompatible options for dental applications and high-temperature materials for industrial use. In the following paragraph, a summary of the digital materials used in printing the vertebral samples is provided [51].

2.1.3 Digital Anatomy Materials

Each material has its unique characteristics and the standard parameters are listed in table 2.3.

- VERO CLEAR is a transparent material that is nearly colorless and offers reliable dimensional stability for general purposes and visual simulation of transparent thermoplastics like PMMA. It possesses the following properties: high transparency, a fine surface finish a remarkable ability to showcase fine details. It is part of the Vero Family and is available in different color variations (Magenta, Cyan and Yellow). It can also be mixed with other materials to achieve a range of colors, levels of translucency or variations in hardness. Its key properties include durability, rigidity, excellent detail representation, options for opaque colors and outstanding dimensional stability.

- AGILUS 30 is a clear and flexible PolyJet Photopolymer with superior tear resistance and tensile strength, making it capable of withstanding repeated flexing and bending cycles. Its properties encompass significant elongation at break (240%), a silicone/rubber-like texture, high tear resistance, and high tensile strength. It can be combined with rigid materials to achieve different flexibility levels.

- TISSUE MATRIX is designed for realistic simulation of soft anatomies, including soft tissues, myocardium, soft organs, muscles, and internal organs. Its properties include being ultra-soft and featuring oriented microfibers to enhance performance, such as suturability.

- BONE MATRIX is a high-toughness material designed for cortical bone and connective tissues. It offers properties like flex-rigidity for bone simulation, the ability to withstand

screw insertion, and resistance to cracking.

- GEL MATRIX is a gel-like support material that does not have any mechanical properties. It can be easily removed from anatomy with inner diameters as small as 1mm and wall thicknesses as low as 1mm.
- VERO ULTRA FAMILY is a rigid opaque material with excellent contrast, sharp text and graphics and it is also durable. It is available in various colors.
- SUPPORT is a support material that can be easily removed with an alkaline cleaning solution or broken away by hand or water pressure.

Table 2.3: *Some properties of Digital Materials [52].*

	Materials		
Properties	*Vero Family*	*Vero Ultra Family*	*Agilus 30*
Tensile Strenght (MPa)	50-65	50-65	2.4-3.1
Elongation at Break	10-25%	5-20%	220-240%
Modulus of Elasticity (MPa)	75-110	65-85	
HDT (°C)	45-50	44-47	
Izod Notched Impact (J/m)	20-30	20-30	

2.1.4 CAD - Grab CAD

Grab CAD enabled us to visualize the arrangement of the models on the printing tray and configure the printing parameters. Through the Digital Anatomy Creator [1], anatomical models are now defined not only by their external geometry and color but also by their unique, patient-specific biomechanics. It automatically designs intricate internal structures using its proprietary digital materials to achieve the appearance, texture, and functionality of your patient's unique anatomy.

[1] See Appendix A

The Digital Anatomy printer offers four predefined anatomical applications: Structured Heart, Blood Vessels, Musculoskeletal and General. Each of these anatomical applications or categories provides specific anatomical elements or characteristics tailored to its intended use. Users have the option to print a model from a particular anatomical category, such as musculoskeletal, and can choose to print it as a single anatomical model or create a model as a single assembly containing multiple assigned structures like the heart, blood vessels, and bone. In Table 2.4 are reported the different types of elements in the Musculoskeletal Family.

Table 2.4: *Musculoskeletral Family.*

Anatomy Element	**Controlled property**
Vertebra	Porosity
Ligament	Stiffness
Intervertebral Discs	Type
Nerves	Flexibility
Facet Joints	Stiffness
General Bone	Density
Long Bone	Type
Ribs	Stifness

In this case study, we employed the Musculoskeletal Anatomy Family, specifically focusing on the Vertebra and General Bone presets, to evaluate the distinctions between the two and characterize their mechanical behavior. Additionally, we explored the Structured Heart Family, specifically the Myocardium Highly Contractible preset, as it exhibited mechanical behaviour similar to lytic metastases [2]. The figure below (A.2) illustrates the structure of the preset used for the specimen.

As you can observe, the difference between the General Bone preset and the Vertebra preset lies in their composition. The General Bone preset contains more Vero Pure White material and has support material primarily concentrated in the center. Conversely, the vertebra preset

[2]See Appendix B

exhibits the opposite characteristics. This contrast mirrors the typical anatomical distinction between vertebrae and long bones. Vertebrae typically have a thick layer of cortical bone on the outside and more trabecular bone on the inside compared to long bones.

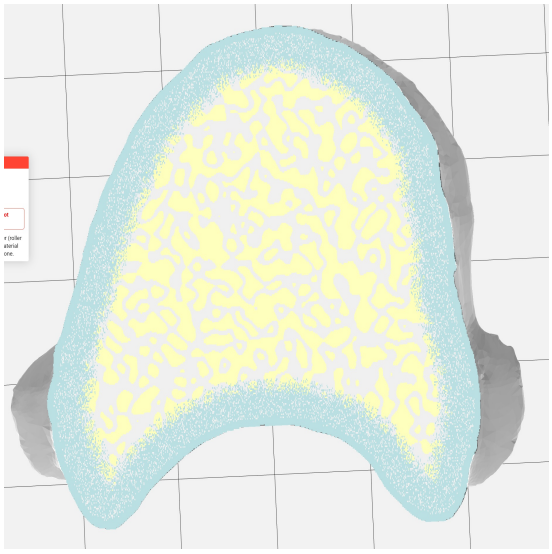

(a) *Internal structure of Vertebra Dense by DAC.*

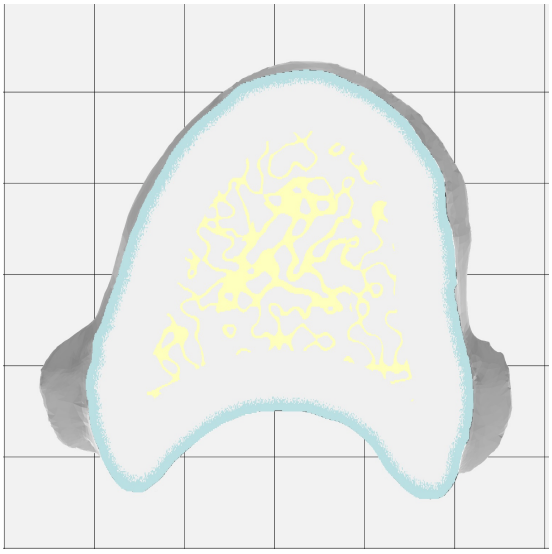

(b) *Internal structure of General Bone Dense by DAC.*

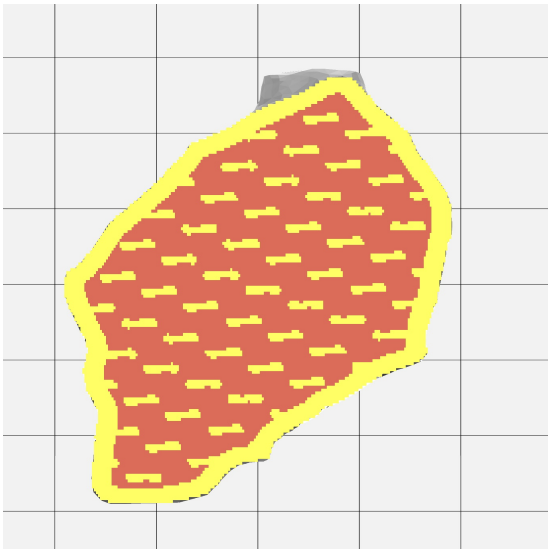

(c) *Internal structure of Highly Contractible Myocardium by DAC.*

Figure 2.4: *Composition of preset used in the model by Digital Anatomy Creator*

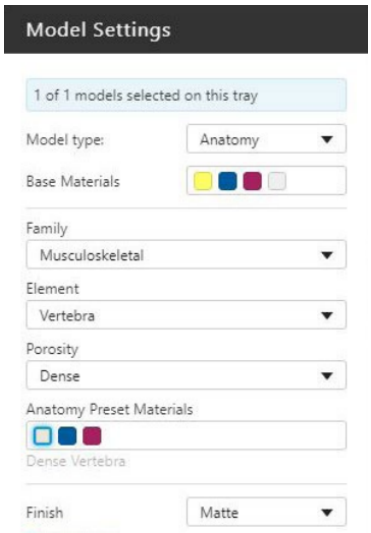

Figure 2.5: *Model settings in Grab Cad.*

After selecting the family and the element, we evaluated the porosity of the sample, distinguishing between dense and porous configurations. The difference between them lies in the composition and thickness of the mid-layer. The dense configuration consists of 1.35 mm thickness with 80% Bone matrix and 20% Vero Pure White, while the porous configuration features 1.65 mm thickness with 90% Bone matrix and 10% Vero Pure White. Furthermore, the porous configuration has a higher background composition of support materials and a smaller scale factor for trabecular bone, resulting in thinner trabeculae. In the initial phase of the project, we conducted an assessment of the mechanical properties of these two different porosity states.

The last aspect of model configuration involved deciding the finishing effect, although this was mainly a matter of aesthetics, and it wasn't a significant focus. In Figure 2.5, you can observe the parameters of model settings. Once the print tray was defined, the software established a connection with the printer and configured the print times and material consumption, including support material, which was subsequently removed manually and with the use of water. In Figure 2.6 you can see the tray view of Grab CAD and the tray with the models after the printing.

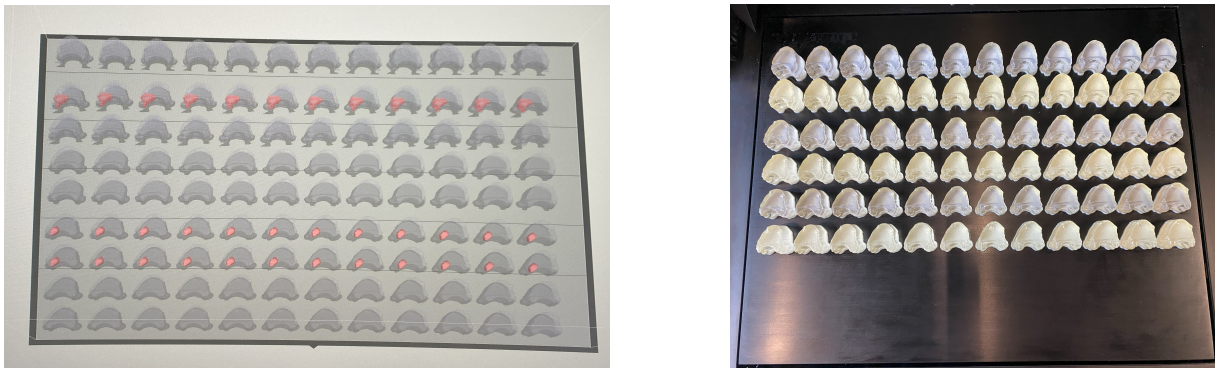

(a) *Example of tray view in GrabCAD.*

(b) *Example of a printed tray.*

Figure 2.6: *3D Printer tray.*

2.2 Specimens

The project was divided into three main phases, as summarized in Figure 2.7.[3][4][5]

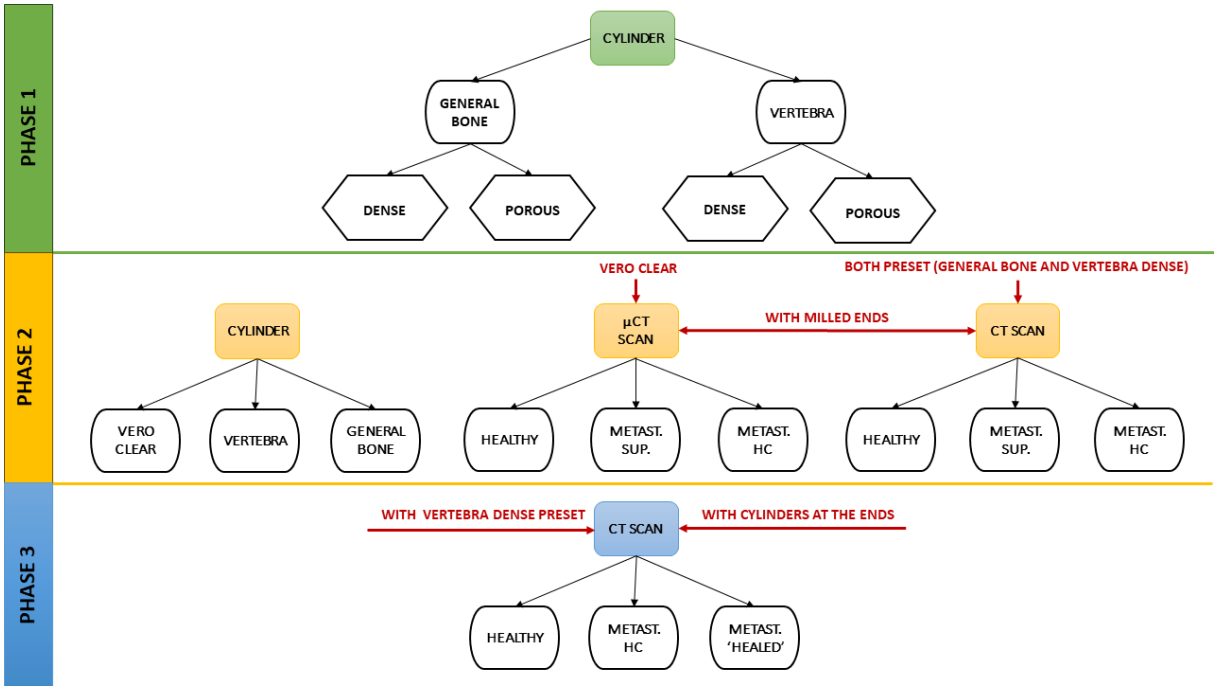

Figure 2.7: *Workflow of specimens*

[3]SUP: abbreviation of Support material.

[4]HC: abbreviation of Highly Contractible material.

[5]HEALED: is an expression used to describe metastatic models in which, with the help of the printer, the metastasis has been removed, leaving only bone tissue, essentially rendering it ”healed”.

2.2.1 Phase 1 - Material properties

As there are no articles in the literature regarding compression tests on the presets created by Stratasys, we explored various options and conducted multiple tests by altering different materials and setups. During this initial phase, the study primarily concentrated on characterizing the material properties of the two printer presets: General Bone and Vertebra, with a particular focus on the characteristics and differences between porous and dense types.
Six dense samples and six porous samples were printed of General Bone preset.
Five dense samples and five porous samples were printed of Vertebra preset.
The first sample for each type (Dense and Porous) was printed a couple of days earlier from the other and was exposed to direct light.

Dimensions

The polymer specimens used to test the material and preset properties are based on ASTM D695-15, which is the Standard Test Method for Compressive Properties of Rigid Plastic.
The sample shape is cylindrical with a diameter of 12.7 mm and a length of 25.4 mm.
To calculate the stress in the mechanical test, the area of the cylinder's base is required. It is calculate by the following equation 2.1.

$$Area = \pi \cdot r^2[mm] \tag{2.1}$$

The figure below (Figure 2.8), shows the difference of internal structure between Vertebra (left) and General Bone (right).

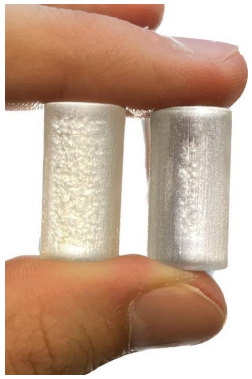

Figure 2.8: *Internal structure of cylinders created using the Vertebra and General Bone presets.*

2.2.2 Phase 2 - Anatomical specimens for compression test

The second phase can be further divided into three parts:

- In the first part, the mechanical characterization of the materials is performed. This includes Vero Clear, which will be used in the models obtained from Micro CT, and the Vertebra and General Bone presets used in the models obtained from clinical CT. While the latter two were previously characterized in the previous phase, in this case, multiple samples will be tested to ensure statistical consistency. Nine samples were printed for each material: Vero Clear, General Bone and Vertebra. Additionally, all samples are printed simultaneously without exposure to sunlight.

- The second part focuses on the mechanical characterization of the models obtained from Micro CT. These models include two parts: one for trabecular bone and one for cortical bone. Therefore, with the exact arrangement of trabeculae obtained through segmentation, the stiffer printable material, Vero Clear, can be used without relying on presets. To model the metastasis in metastatic specimens, support material is used once and Highly Contractible Myocardium material is used another time. Ten samples were printed for each category (Healthy, Metastatic with Support, Metastatic with Highly Contractible material).

- In the third part, the models obtained from clinical CT are mechanically characterized. This involves using the General Bone preset and the Vertebra preset. In this case, since there is only one part for both cortical and trabecular bone, the internal trabecular structure is defined based on the preset used, as it follow segmentation solely for the border. Such as for metastatic vertebrae in the second part, metastasis in these models is printed with support material once and with Highly Contractible material another time. In this case ten samples were printed for each category (Healthy, Metastatic with Support, Metastatic with Highly Contractible material) with Vertebra preset and ten samples for the same category but with General Bone preset.

Dimensions

For the anatomical specimens, we made an initial distinction based on the medical image from which they were obtained: CT Scan or Micro CT.
For each of these categories, three types of specimens were printed:

- Healthy,
- Metastatic with metastases in support material,
- Metastatic with metastases in highly contractible material.

In figure 2.9, various types of vertebrae and their internal structures are represented.

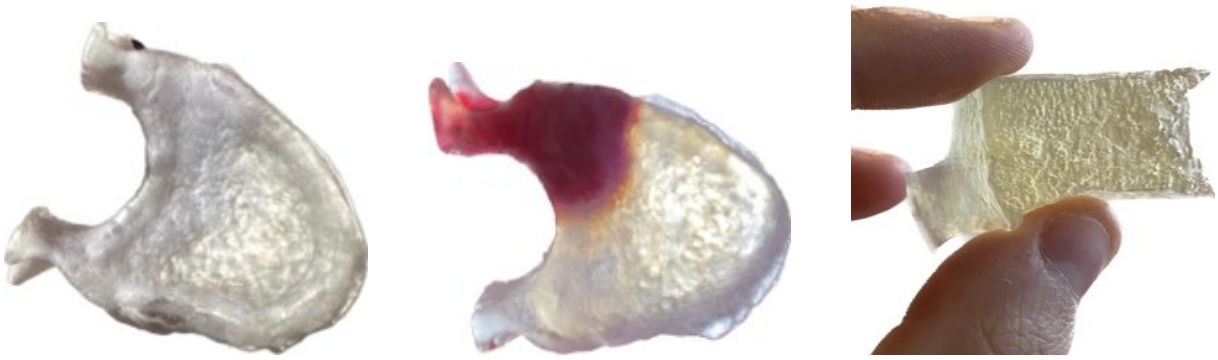

(a) *Healthy vertebrae.* **(b)** *Metastatic vertebrae.* **(c)** *Internal bone structure of vertebrae.*

Figure 2.9

Depending on the imaging methodology and type (healthy or metastatic), the specimens have different dimensions. Moreover, the samples were milled, using a Sealey 915 x 100mm Belt/Ø150mm Disc Sander bench machine (Figure 2.10), to avoid local stress concentrations and ensure a flat load-bearing surface.
Performing this operation manually can lead to slight variations in the dimensions of each individual specimen. Therefore, the main dimensions of each model, including cranial-caudal height, right-left width and anteroposterior lenght, were measured using calipers and an average for each category was recorded in the table 2.5.

(a) *Milled bench machine.*

(b) *Model after milling.*

Figure 2.10

Table 2.5: *Dimensions of different type of models.*

	Height (h) (mm)	**Lenght (l) (mm)**	**Widht (p) (mm)**
Micro CT			
Healthy	17.70	34.20	29.80
Metastatic with Support	18.20	32.90	28.40
Metastatic with HC	18.12	32.90	28.40
Clinical CT - Vertebra			
Healthy	19.27	29.90	28.50
Metastatic with Support	19.45	26.10	25.30
Metastatic with HC	19.44	26.10	25.30
Clinical CT - General Bone			
Healthy	19.23	29.90	28.50
Metastatic with Support	19.38	26.10	25.30
Metastatic with HC	19.37	26.10	25.30

Also in this case to calculate the stress in the mechanical test, it was assumed that the force is uniformly distributed over the cross-sectional area of the vertebra (approximated as an ellipse); below is the expression used 2.2.

$$Area = \frac{l}{2} \cdot \frac{p}{2} \cdot \pi[mm] \tag{2.2}$$

2.2.3 Phase 3 - Anatomical specimens with support CAD design

In the final phase, three types of specimens were tested, all obtained from Clinical CT using the Vertebra preset. The comparison will be made between healthy models, metastatic models with the use of Highly Contractible material inside and a final type called 'Healed', which represents the metastatic vertebra but treated differently. In the 'Healed' type, the metastatic part is filled through the printer software as if it is bone, using the printing software, with trabeculae identical to those present in the rest of the vertebra's body.
In this phase, all models were not milled but instead encapsulated within cylinders, to employ a more accurate methodology with reduced variability.
Six samples were printed for each category (Healthy and Metastatic with Highly Contractible). Regarding the 'Healed' type, only four samples were printed, and furthermore, these samples were printed horizontally rather than vertically like the other specimens. This could potentially introduce artifacts in the obtained values.

Dimensions

The cylinders were made by a commercial CAD software and have precise dimensions:

- Height = 36mm;
- Diameter = 40mm.

All the cylinders were made entirely of Vero Clear material. Moreover, feature a negative impression of the vertebrae to ensure that the connection between the vertebrae and cylinders does not introduce local stress concentrations during testing (Figure 2.11).

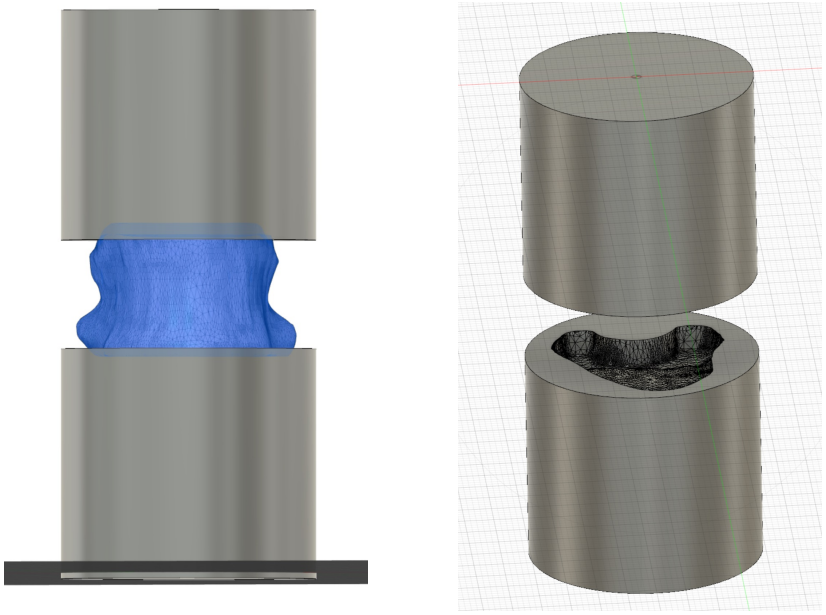

(a) *Assembly between vertebrae and cylinders.*

(b) *Negative impression of the vertebrae inside of the cylinders.*

Figure 2.11: *Support CAD Design.*

In this case, as the ends are not milled, the dimensions of the models will match those obtained from clinical CT scans and will only differ between the healthy and metastatic vertebrae, as indicated in the table 2.6.

Table 2.6: *Dimensions of models without milled ends.*

Clinical CT - Vertebra - with cylinders	**Height (h) (mm)**	**Lenght (l) (mm)**	**Widht (p) (mm)**
Healthy	19.40	29.90	28.50
Metastatic with Highly Contractible	19.60	26.10	25.30
Metastatic 'Healed'	19.60	26.10	25.30

The equation for the area of the vertebra, which will be used to calculate stress, is the same as the one seen previously (2.2).

2.3 Mechanical test

The mechanical tests for phases 1 and 2 were conducted at the Technological Innovation Center (Taeknisetur) in Reykjavik (Figure 2.12, (a)), while those for phase 3 were carried out at the Biomechanics Laboratory of the Department of Industrial Engineering at the University of Bologna. All the specimens were subjected to compression testing until failure.

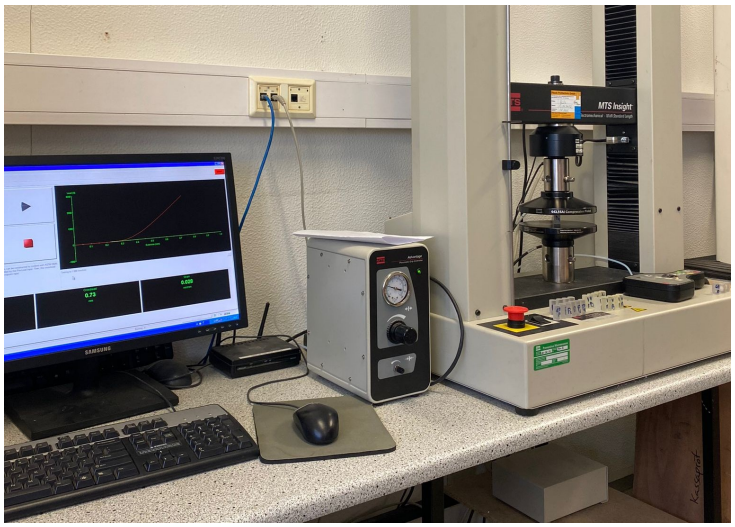

(a) *Mechanical test machine in Reykjavik: MTS Insight ElectroMechanical*

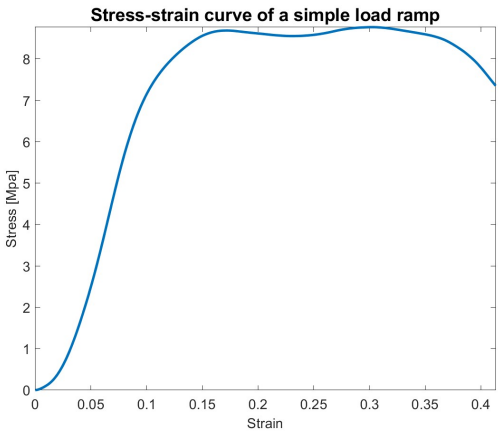

(b) *Stress-strain curve of a simple load ramp.*

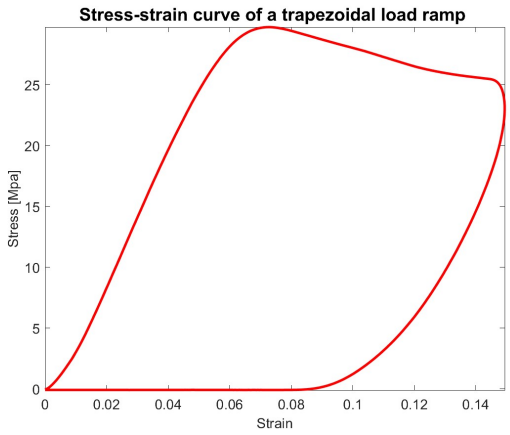

(c) *Stress strain curve of a trapezoidal load ramp.*

Figure 2.12: *Mechanical test setup in Reykjavik and comparison between simple load ramp and trapezoidal load ramp.*

The machine used for the mechanical tests in Reykjavik was an MTS Insight ElectroMechanical – Standard Length, equipped with a 10kN load cell and operating at a frequency of 10 Hz. The test setup followed the ASTM D695 – 15 standard [53] and used a simple load ramp with a speed of 1.3 mm/min.
This type of test allows the determination of the maximum stress and deformation, and the value at failure. Figure 2.12 (b) shows the stress-strain curve of one of the models tested using this setup.

Instead, the mechanical tests conducted at the University of Bologna were performed using a single-axis hydraulic press with Instron 8502 electronics, featuring a 100 kN load cell, ensuring that there are no issues with failure. The mechanical test was conducted involving a trapezoidal load ramp with a frequency of 100 Hz and a loading phase of -3mm at a speed of 0.3 mm/s, followed by a rest period of 0.01 sec, and unloading that matched the loading (Fig. 2.12 (c)). With this type of load ramp, it is possible to calculate not only the maximum value of stress and deformation, but also the ultimate tensile strength, as well as the residual deformation.
The limit for calculating residual deformation was set at 5% of the maximum stress during the unloading phase. Unfortunately, due to some issues, the first two samples of the metastatic models used a simple load ramp, so it was not possible to calculate the residual strain for them.

2.4 Metrics

As the data provided by the testing machine can exhibit considerable measurement noise, it was necessary to apply a 50-point moving average filter to all specimens (Figure 2.13). This filtering operation was performed to remove noise, creating a smoothing effect, thereby enhancing the readability and analysis of the graphs.

Using the force and displacement data provided by the testing machine, it was possible to determine the stress (σ) and strain (ε) values acting on the specimens during the conducted tests. To exclude sections with play, only force values greater than the preload (approximately 5-20% of the maximum force) were considered. In the case under examination, only values

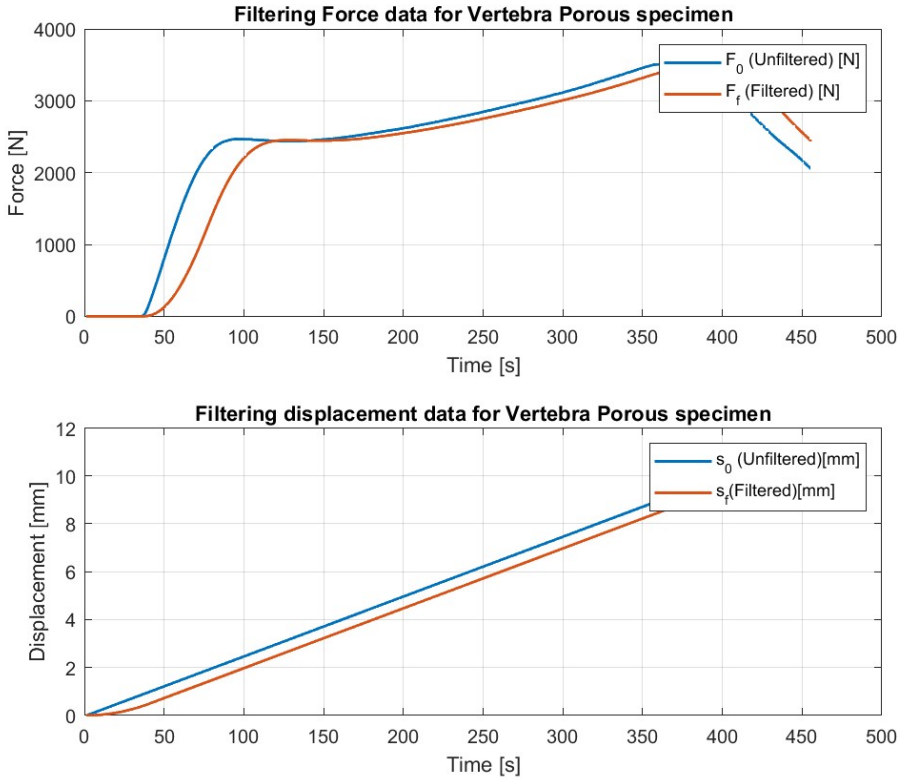

Figure 2.13: *Example of data filtered.*

exceeding 5% of the maximum force were selected.

The machine's initial offset was subtracted from the initial displacement to ensure zero displacement when the force is zero. Then, for the calculation of strain, it was assumed that the displacement is distributed over an average free height of the measurements. Once stress and strain values were obtained, they were plotted using Matlab software. The following chapter presents the graphs illustrating the relationship between stress and strain, as well as the elastic modulus.

For the elastic modulus (E), it was considered the initial point as 20% of the maximum force and the final point as 80% of the maximum force, thus excluding the initial settling and evaluating the primarily linear region. Below are the equations used to calculate stress, strain and the elastic modulus [2.3,2.4,2.5].

$$\sigma = \frac{F}{Area}[MPa] \tag{2.3}$$

$$\epsilon = \frac{s}{h} \tag{2.4}$$

$$E = \frac{\sigma}{\epsilon} = \frac{\sigma_{80\%maxforce} - \sigma_{20\%maxforce}}{\epsilon_{80\%maxforce} - \epsilon_{20\%maxforce}}[MPa] \tag{2.5}$$

In general, the tables include average values of these quantities to avoid including numerous data points. For the elastic modulus, the standard deviation has also been calculated, representing the variability of this data among the different samples. As an additional parameter, the deformation difference between a control model (healthy) and a metastatic , or healthy and metastatic, was calculated using the formula provided (2.6).

$$\sigma = \frac{\epsilon_{metastaticsubROIs} - \epsilon_{controlsubROIs}}{\epsilon_{controlsubROIs}} \tag{2.6}$$

To made some real comparison, a statistical analysis of the T-test type was carried out, comparing the healthy and metastatic samples (independent data) as well as the metastatic and treated samples (paired data). This analysis aimed to determine whether the observed differences between these two types were statistically significant or could be attributed to chance. The test was applied separately for differente typology of models (unpaired data or paired data), considering stress and strain as the variables of interest.
To conduct the test, the following were needed:

- Two sets of data, in this case, the mean values of the mentioned variables were used.
- Knowledge of the tail, i.e., whether there is a relationship between the variables in both directions or in a single direction. Both cases under examination involve relationships in both directions.
- Type of test: paired, with identical (homoscedastic) or dissimilar (heteroscedastic) variance. Although healthy and metastatic samples have different sizes, they were subjected to the same test with equal parameters. Therefore, a paired test is considered for both types.

Initially, the hypothesis H0 (null hypothesis) is rejected in order to study the level of correlation between the factors, i.e., whether there is a systematic factor or if everything is due to chance. The obtained p-value represents the smallest significance level, i.e., the probability of committing a type I error. A systematic factor is believed to exist when, in reality, everything is due to chance. Rejecting the null hypothesis H0 erroneously when it is actually true.
The significance level of p-value is set at 0.05.

Chapter 3

Results

3.1 Phase 1

3.1.1 General Bone Dense and Porous

The stress-strain curves of the individual samples are graphed below (Figure 3.1) and the maximum stresses, deformations and elastic modulus are tabulated in table 3.1[1] and 3.2[2].

Table 3.1: *General Bone Dense data.*

	GBD1	**GBD2**	**GBD3**	**GBD4**	**GBD5**	**GBD6**
Max Stress [MPa]	64.21	70.19	70.44	70.42	70.48	70.16
Max Strain	0.173	0.186	0.191	0.193	0.187	0.189
Elastic Modulus [MPa]	1398.9	1478.7	1481.4	1456.5	1446.5	1439.1

The values from different samples are consistent.
All samples within the same category exhibit a maximum stress of approximately 70 MPa. The maximum strain is around 0.180 and the average Elastic Modulus is 1450 MPa.

[1]GBD: abbreviation of General Bone Dense.
[2]GBP: abbreviation of General Bone Porous.

Table 3.2: *General Bone Porous data.*

	GBP1	GBP2	GBP3	GBP4	GBP5	GBP6
Max Stress [MPa]	64.27	70.07	70.14	68.41	69.50	69.23
Max Strain	0.190	0.184	0.184	0.189	0.188	0.212
Elastic Modulus [MPa]	1405.3	1482.4	1482.1	1415.4	1463.8	1453.2

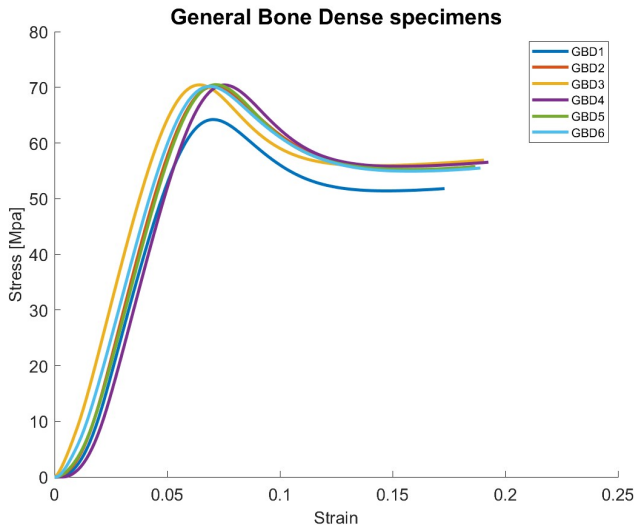

(a) *Stress-strain curve of General Bone Dense samples.*

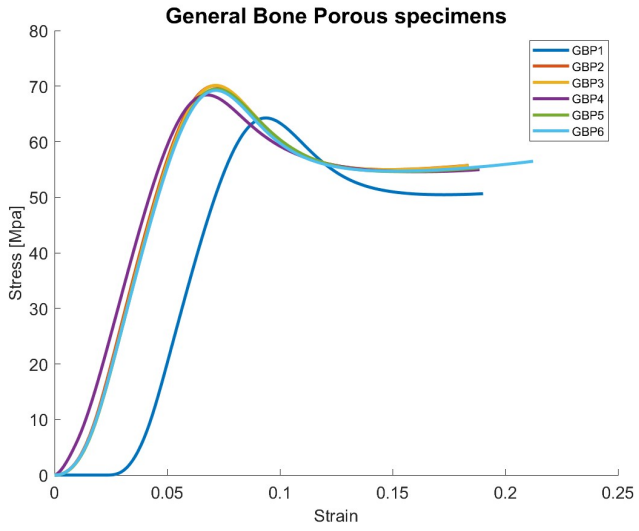

(b) *Stress-strain curve of General Bone Porous samples.*

Figure 3.1: *Stress-strain curve of General Bone specimens.*

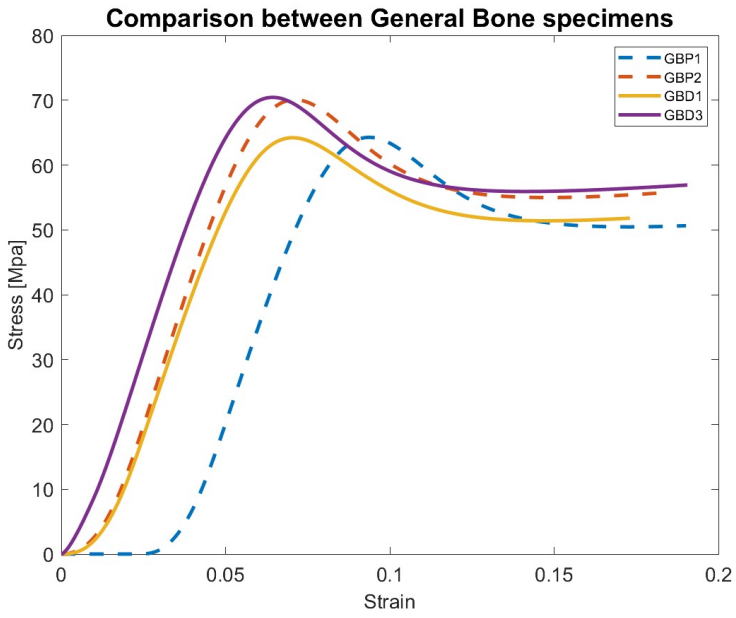

Figure 3.2: *Comparison of stress-strain curves between General Bone Dense and Porous samples. For each category, the first sample and the one with the highest elastic modulus are graphed.*

Table 3.3: *T-test for General Bone specimens*

General Bone Dense - General Bone Porous	
	p-value
Stress	0.0751
Strain	0.3833

No noticeable differences have been observed between the dense and porous types. They exhibit similar trends and values, with slightly lower values for the porous type.

The first sample for each type (Dense and Porous) exhibits lower values, possibly due to the fact that it was printed a couple of days earlier and exposed to direct light, resulting in a slight loss of properties.

No sample reached fracture. Both stress and strain obtained a p-value higher than the significance level set at 0.05. Therefore, the different porosity is not statistically significant for the model.

3.1.2 Vertebra Dense and Porous

Stress-strain curves of the individual samples are graphed below (Figure 3.3) and the maximum stresses, deformations and elastic modulus are tabulated in table 3.4[3] and 3.5[4].

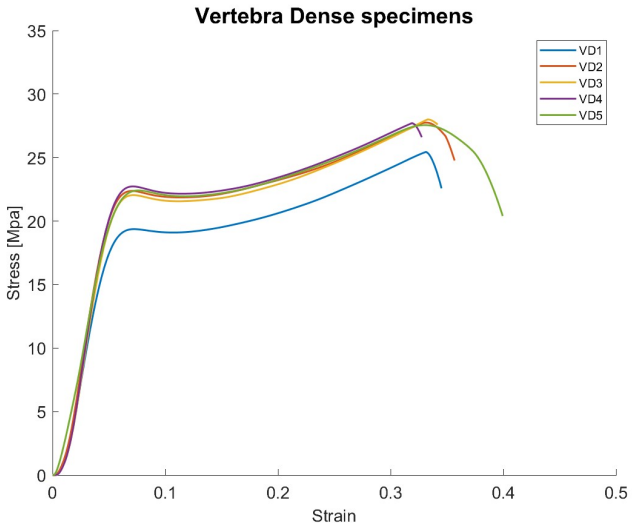

(a) *Stress-strain curve of Vertebra Dense samples.*

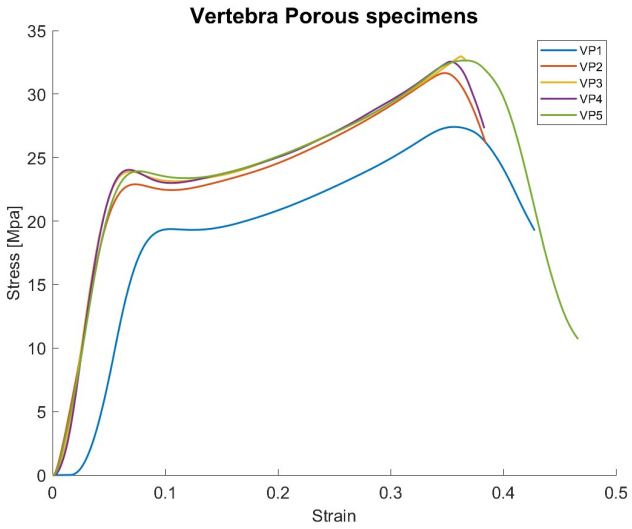

(b) *Stress-strain curve of Vertebra Porous samples.*

Figure 3.3: *Stress-strain curve of Vertebra specimens.*

The values from different samples are consistent, like for General Bone typology.

[3]VD: abbreviation of Vertebra Dense.

[4]VP: abbreviation of Vertebra Porous.

Table 3.4: *Vertebra Dense data.*

	VD1	**VD2**	**VD3**	**VD4**	**VD5**
Max Stress [MPa]	22.44	25.75	28.00	27.71	27.59
Max Strain	0.345	0.357	0.342	0.328	0.400
Elastic Modulus [MPa]	468.7	533.9	528.9	552.1	454.1

Table 3.5: *Vertebra Porous data.*

	VD1	**VD2**	**VD3**	**VD4**	**VD5**
Max Stress [MPa]	27.41	31.66	32.98	32.55	32.65
Max Strain	0.428	0.385	0.367	0.383	0.467
Elastic Modulus [MPa]	389.4	472.9	567.6	580.8	483.7

All samples within the same category exhibit a maximum stress of approximately 27 MPa for Dense and 31 MPa for Porous. The maximum strain is around 0.360 for Dense and 0.400 for Porous. The average Elastic Modulus is approximately 500 MPa for both Dense and Porous. Also here the first sample for each type (Dense and Porous) exhibits lower values, possibly due to the fact that it was printed a couple of days earlier and exposed to direct light, resulting in a slight loss of properties. All samples reached fracture.
Slightly noticeable differences have been observed between the dense and porous types (Figure 3.4. But they show similar trends.

Table 3.6: *T-test for Vertebra specimens*

Vertebra Dense - Vertebra Porous	
	p-value
Stress	0.0021
Strain	0.0096

Both stress and strain obtained a p-value lower than the significance level set at 0.05. Therefore, the different porosity in this case is statistically significant for the model.

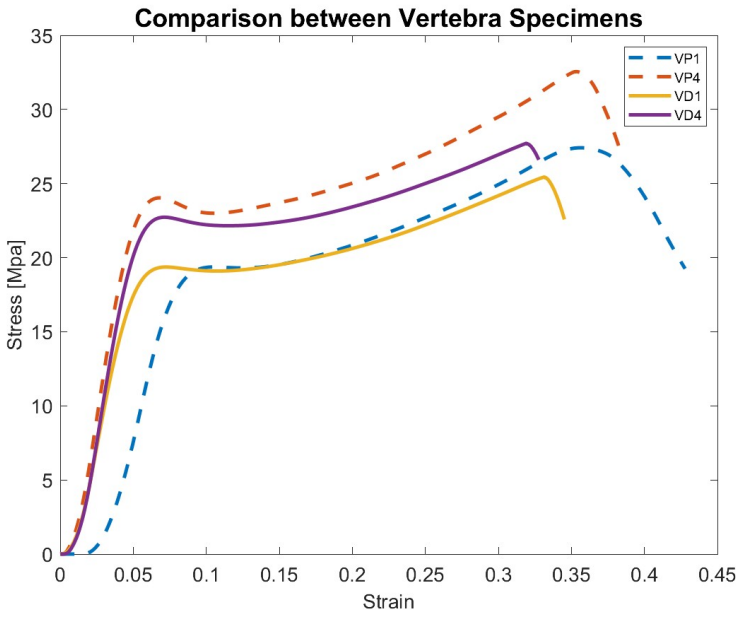

Figure 3.4: *Comparison of stress-strain curves between Vertebra Dense and Porous samples. For each category, the first sample and the one with the highest elastic modulus are graphed.*

3.1.3 Comparison

Based on what has been observed in the previous paragraphs, there doesn't appear to be a significant difference in porosity variation. Polymers have lower mechanical properties compared to human bone and the dense type should exhibit greater strength, given its lower amount of support in the composition and a larger scale factor (meaning thicker trabeculae) compared to the porous type. Therefore, to eliminate one variable in the characterization and simplify the printing workflow, it has been decided that all subsequent models will feature dense porosity.
Regarding the differences between the General Bone and Vertebra presets based on these initial tests, we can observe (figure 3.5) that they have significantly different maximum elastic modulus values: 1.5 GPa for General Bone and 0.5 GPa for Vertebra.
Additionally, their stress-strain behaviors are also different. For General Bone, there is an initial linear peak, followed by subsequent yielding and then a further increase towards a second peak, which was not calculated due to the machine's limit (a load cell of 10 kN).
In contrast, the Vertebra preset exhibits an initial linear peak, which is less pronounced compared to General Bone. After a slight yielding, there is a second peak slightly higher than the

first, leading to sample failure (as depicted in the figure 3.6).

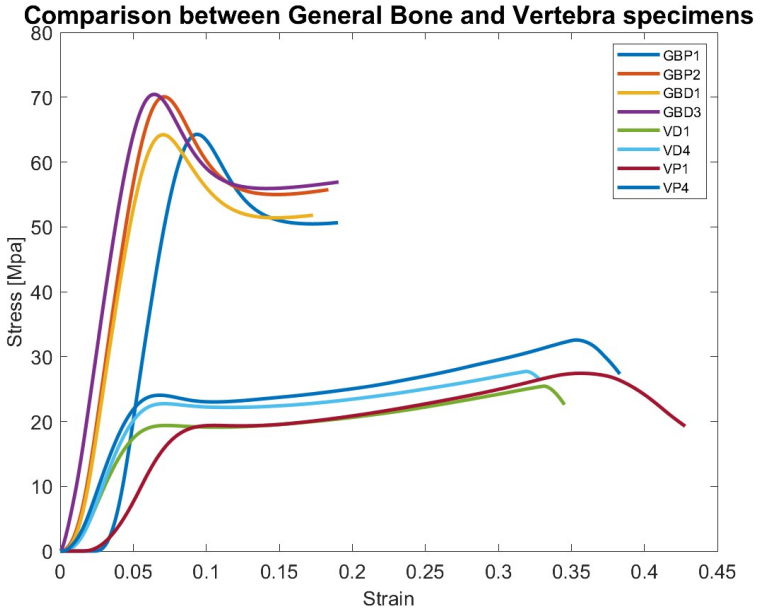

Figure 3.5: *Comparison of stress-strain curves between General Bone and Vertebra samples. For each category, the first sample and the one with the highest elastic modulus are graphed.*

As an initial analysis, when compared to existing literature, it appears that the behavior of the Vertebra preset is more similar to that of real bone. However, since we have only tested cylindrical samples, a more in-depth and detailed analysis of models obtained through segmentation will be conducted in the subsequent phase.

Figure 3.6: *Failure of Vertebra sample.*

3.2 Phase 2

3.2.1 Materials: Vero Clear, General Bone and Vertebra

Below, are reported the stress-strain curves of the individual samples (Figure 3.7). Outside of some specific cases, it is evident that the printer's replicability and reproducibility are highly accurate. All samples of the same material type exhibit similar trends and values.

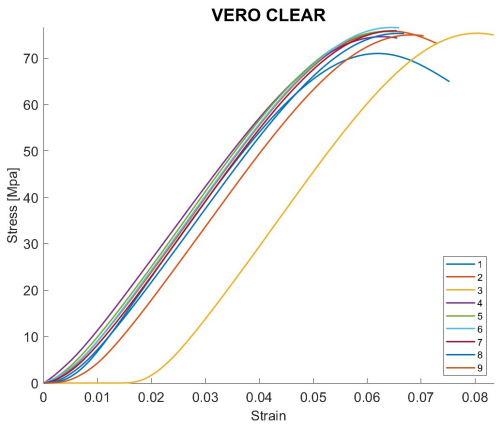

(a) *Stress-strain curve of Vero Clear samples.*

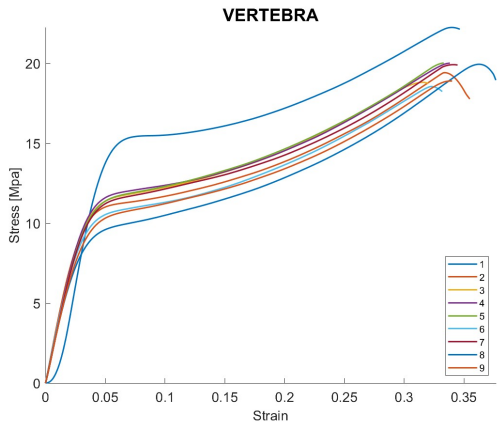

(b) *Stress-strain curve of Vertebra samples.*

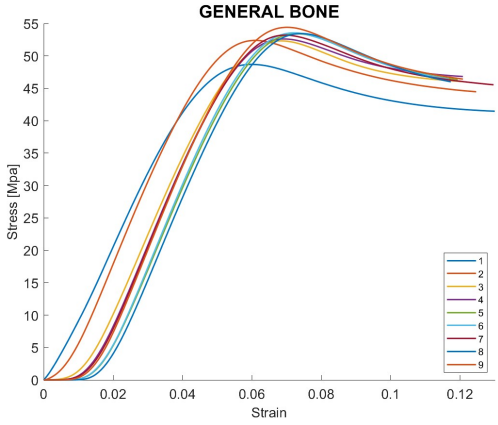

(c) *Stress-strain curve of General Bone samples.*

Figure 3.7: *Stress-strain curve comparison between different materials' specimens.*

The table 3.7 provide the average values of maximum stress, maximum strain, and elastic modulus for the materials. The graph 3.8, on the other hand, represents the mean value and standard deviation of each material.

Table 3.7: *Data comparison of materials.*

SPECIMEN	VERO CLEAR	VERTEBRA	GENERAL BONE
Average value of the maximum stress [MPa]	75.00	22.32	53.16
Average value of the maximum strain	0.072	0.358	0.122
Average value of Elastic Modulus [MPa]	1542.4	58.2	1202.8
Standard deviation of Elastic Modulus	12.71	3.23	16.89

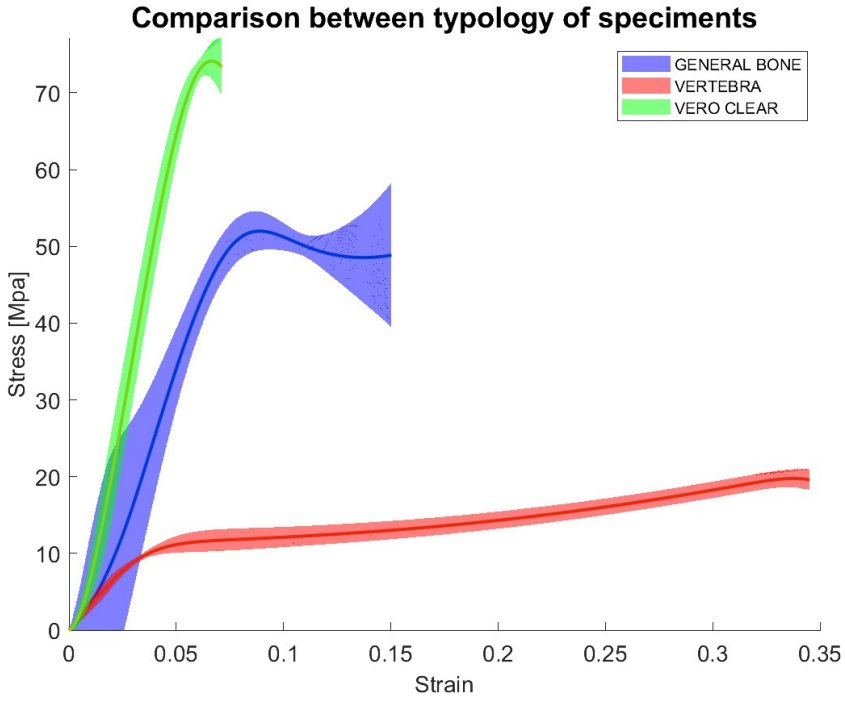

Figure 3.8: *Comparison between average value and standard deviation of each material.*

In general, it can be confirmed from the obtained values that Vero Clear is the most resilient material among them. In fact, it is the only material that did not reach fracture or show macroscopic deformations during the mechanical test (using a 10 kN load cell).

General Bone, on the other hand, presents intermediate values, which are significantly higher than the Vertebra type. It can withstand double the stresses but still exhibits greater deformations compared to Vero Clear. As shown in the figure 3.9, the second sample appears more compressed and with reduced dimensions. Finally, Vertebra has the lowest characteristics compared to the others, with high deformations and low stresses. The elastic modulus is also low and in this case, the sample reached fracture, displaying a crack on the side.

Figure 3.9: *Speciments after the mechical test. From the left,first one is Vero Clear, second one is General Bone and third one Vertebra.*

3.2.2 Micro CT: Healthy, with HC Metastasis, with support Metastasis

Table 3.8: *Data comparison of specimens obtained from Micro CT.*

SPECIMEN	HEALTHY	METASTATIC WITH SUPPORT	METASTATIC WITH HC
Average value of the maximum stress [MPA]	1.10	4.02	4.03
Average value of the maximum strain	0.308	0.137	0.103
Average value of Elastic Modulus [MPA]	11.1	66.20	75.65
Standard deviation of Elastic Modulus	1.05	16.68	13.03

Table 3.8 provides the average values of maximum stress, maximum strain, elastic modulus and relative standard deviation for the materials.

In graphs 3.10,3.11,3.12 are represent stress-strain curve of samples of each typology, instead a comparison between the mean value and the standard deviation of each material is represented in graph 3.13.

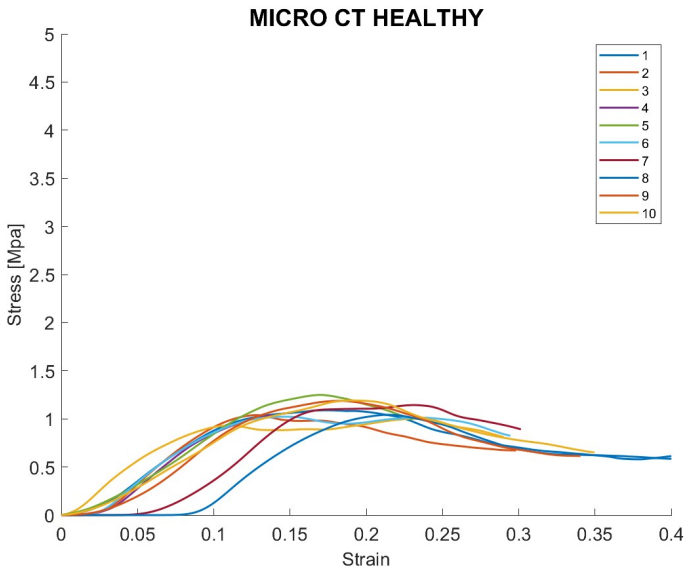

Figure 3.10: *Stress-strain curve of Healthy samples obtained from Micro CT scan.*

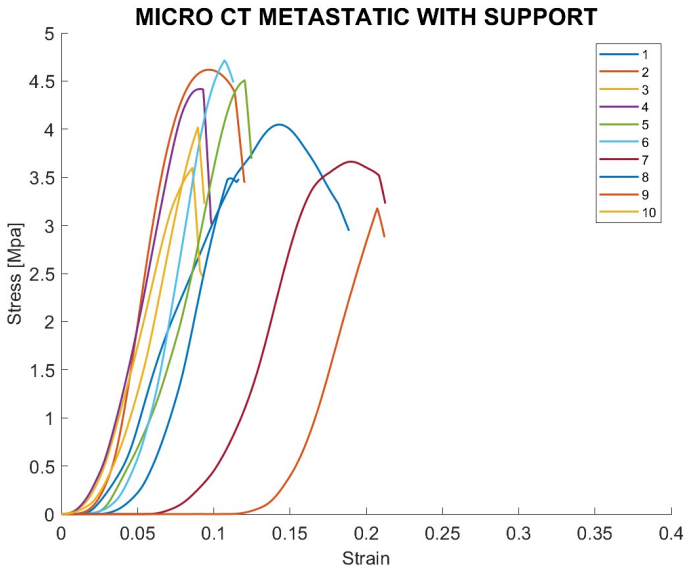

Figure 3.11: *Stress-strain curve of Metastatic samples with metastasis of support material obtained from Micro CT scan.*

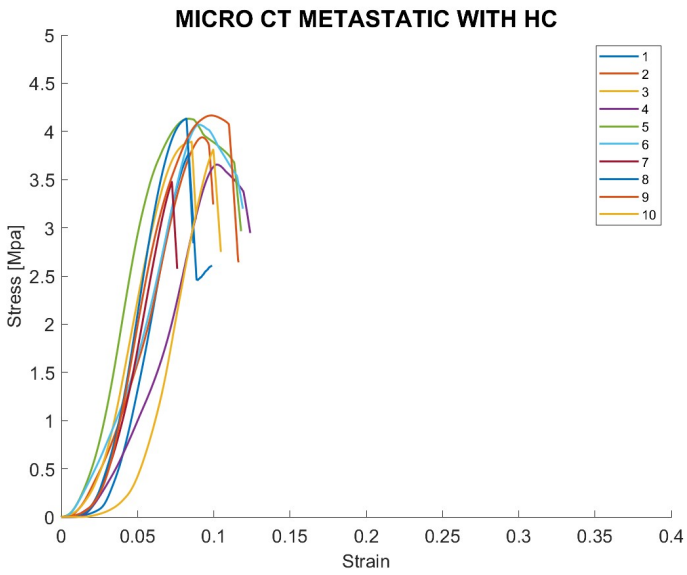

Figure 3.12: *Stress-strain curve of Metastatic samples with metastasis of highly contractible obtained from Micro CT scan.*

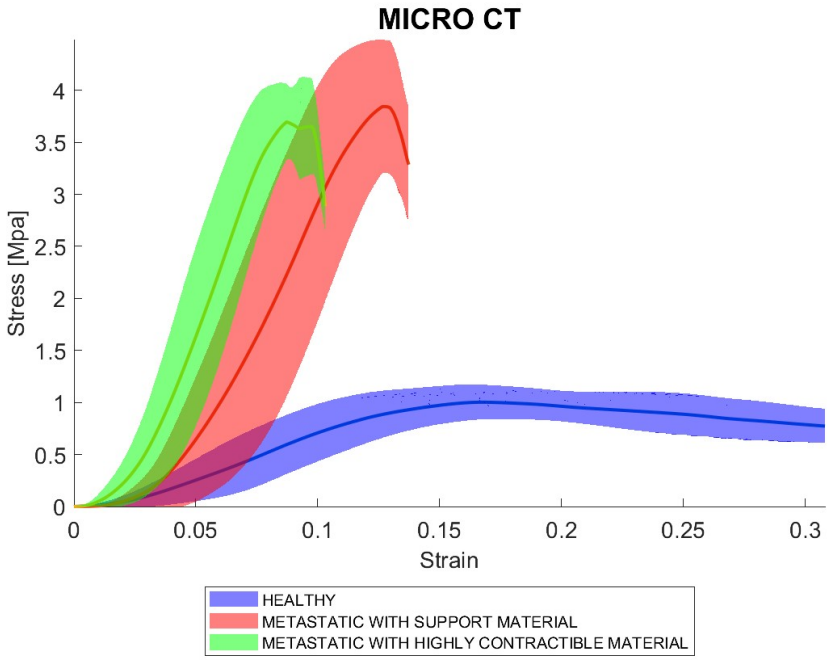

Figure 3.13: *Comparison between different types of specimens obtained from Micro CT. The solid line represents the mean value, while the shaded area represents the range of standard deviation.*

All the samples reached fracture 3.14. In the case of healthy samples, the mode of failure involves complete fragmentation. As for the metastatic vertebrae, they exhibited greater resistance. The one with support inside fractured in the middle without any material loss, whereas the one with HC inside cracked both on the side and at the back, concentrating the damage around the metastatic area. As the load increased, soft material (HC) gradually extruded from the cracked region.

(a) *Failure of Healthy samples.*

(b) *Failure of Metastatic samples with metastasis of support material.*

(c) *Failure of Metastatic samples with metastasis of highly contractible material.*

Figure 3.14: *Modes of failure of micro CT samples.*

In general, as can be observed from the data, the metastatic samples withstand higher stresses and show less deformation. However, the values for all types are low and less resistant compared to the typical data for human bone. The stress-strain behaviors of the metastatic samples exhibit an initial linear peak followed by fracture, while the healthy samples show significantly different and divergent behaviors. This could be attributed to the segmentation process or the methods used to obtain the model. Slightly noticeable differences have been observed between the two types of metastasis. Both stress and strain obtained a p-value (Table 3.9) higher than the significance level set at 0.05. Therefore, the different type of material used for the metastasis is not statistically significant for the model.

Table 3.9: *T-test for Metastatic specimens obtained from MicroCT.*

Metastatic with Support - Metastatic with HC	
	p-value
Stress	0.9890
Strain	0.0763

3.2.3 Clinical CT - Vertebra: Healthy and with Metastasis

Table 3.10 provides the average values of maximum stress, maximum strain, elastic modulus and relative standard deviation for the materials.

Table 3.10: *Data comparison of specimens obtained from Clinical CT using the Vertebra template.*

SPECIMEN	**HEALTHY**	**METASTATIC WITH SUPPORT**	**METASTATIC WITH HC**
Average value of the maximum stress [MPa]	8.71	10.92	8.60
Average value of the maximum strain	0.375	0.423	0.421
Average value of Elastic Modulus [MPa]	81.9	77.7	57.0
Standard deviation of Elastic Modulus	7.76	4.84	3.31

The metastatic samples with support material inside exhibit higher properties and better rigidity, also compared to the other typology of metastatic model.
Overall, all types of vertebrae exhibit similar trends and less variability.
In graphs 3.15,3.16,3.17 are represent stress-strain curve of samples of each typology.

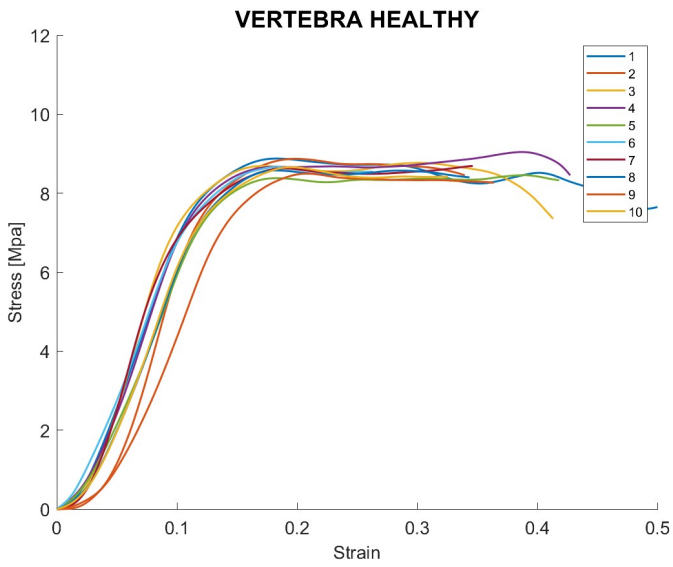

Figure 3.15: *Stress-strain curve of Healthy samples obtained from Clinical CT scan with Vertebra preset.*

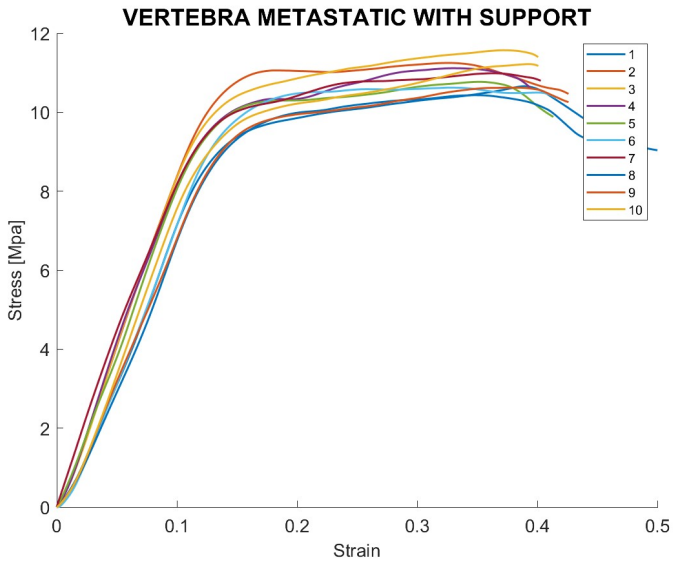

Figure 3.16: *Stress-strain curve of Metastatic samples with metastasis of support material obtained from Clinical CT scan with Vertebra preset.*

All the samples reached fracture (Fig. 3.18).

In the case of healthy samples, there is a crack in the front part of the model. Healthy samples exhibit lower resistance compared to metastatic ones. Meanwhile, metastatic samples with support material have a mode of failure similar to the healthy ones, primarily concentrated in the front part and they are more resilient than the HC material type. The latter,

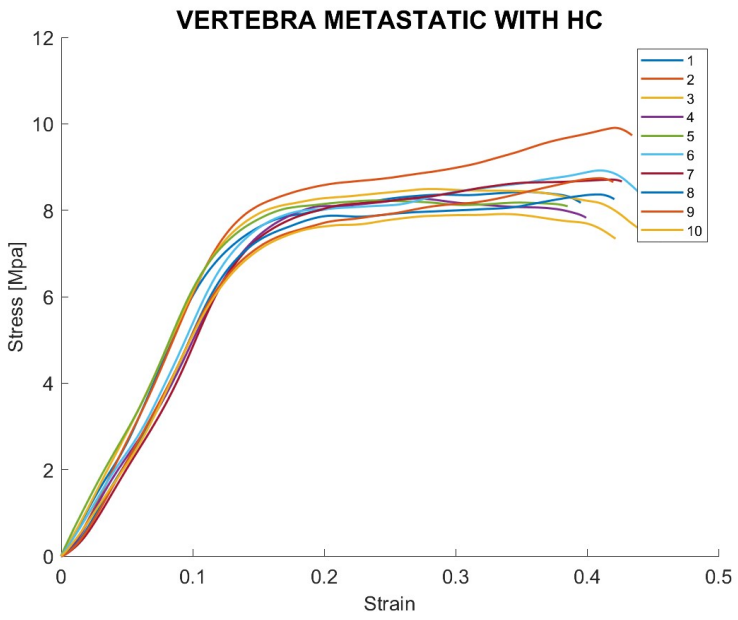

Figure 3.17: *Stress-strain curve of Metastatic samples with metastasis of highly contractible obtained from Clinical CT scan with Vertebra preset.*

(a) *Failure of Healthy samples.*

(b) *Failure of Metastatic samples with metastasis of support material.*

(c) *Failure of Metastatic samples with metastasis of highly contractible material.*

Figure 3.18: *Modes of failure of Vertebra samples from CT clinical scan.*

however, experience a fracture in the rear part of the model, in the area of metastatic concentration, and during compression, they expel the metastatic material outward, as depicted in Figure (3.19). In terms of mechanical characteristics, they fall in between the other two types.

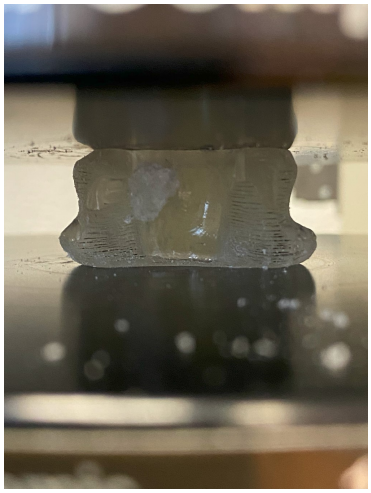

Figure 3.19: *Failure of the Metastatic vertebrae with HC during the machine test. As you can see, the metastatic material is protruding from the posterior part of the model.*

Table 3.11: *T-test for Metastatic specimens obtained from Ct Clinical with Vertebra preset.*

Metastatic with Support - Metastatic with HC	
	p-value
Stress	8.6330^{-07}
Strain	0.9054

Slightly noticeable differences have been observed between the two types of metastasis. From the T test (Table 3.11), stress obtained a p-value lower than the significance level set at 0.05. Instead the strain obtained a p value higher. So the different type of material used for the metastasis is statistically significant for the stress but not for the strain.

3.2.4 Clinical CT - General Bone: Healthy and with Metastasis

Table 3.12 provides the average values of maximum stress, maximum strain, elastic modulus and relative standard deviation for the materials. In this case as well, healthy samples exhibit lower resistance compared to metastatic ones. The metastatic samples have similar maximum stresses, while those with internal support material deform less and have a higher average elastic modulus, confirming their higher resistance among the three types.

Table 3.12: *Data comparison of specimens obtained from Clinical CT using the General Bone template.*

SPECIMEN	***HEALTHY***	***METASTATIC WITH SUPPORT***	***METASTATIC WITH HC***
Average value of the maximum stress [MPa]	14.41	18.71	18.79
Average value of the maximum strain	0.063	0.055	0.076
Average value of Elastic Modulus [MPa]	320.8	432.7	336.2
Standard deviation of Elastic Modulus	15.75	17.16	22.97

In graphs 3.20,3.21,3.22 are represent stress-strain curve of samples of each typology. All the models exhibit a linear, almost rigid behavior with an increasing trend. Compared to the Vertebra preset, they show greater variability among the various samples.

Table 3.13: *T-test for Metastatic specimens obtained from Ct Clinical with General Bone preset.*

Metastatic with Support - Metastatic with HC	
	p-value
Stress	0.0487
Strain	7.3849^{-5}

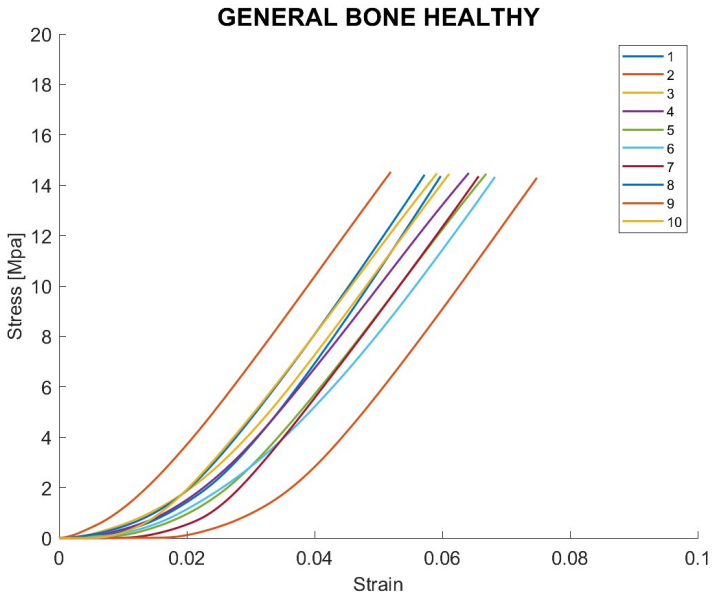

Figure 3.20: *Stress-strain curve of Healthy samples obtained from Clinical CT scan with General Bone preset.*

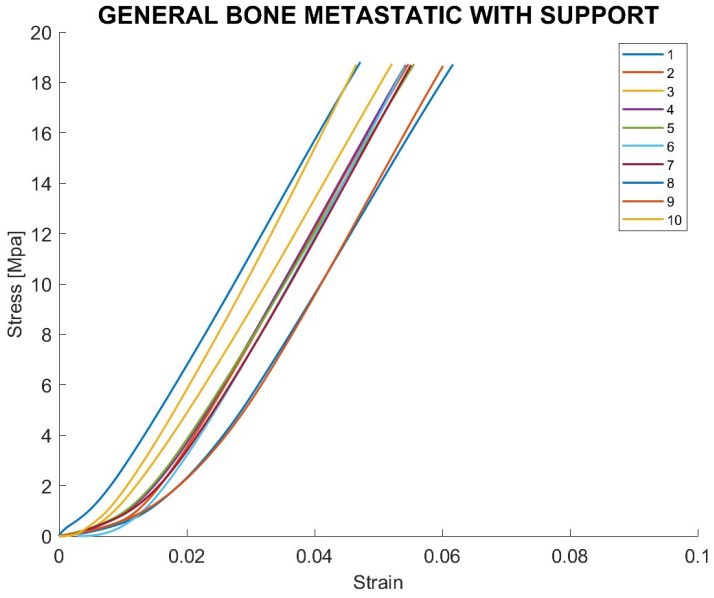

Figure 3.21: *Stress-strain curve of Metastatic samples with metastasis of support material obtained from Clinical CT scan with General Bone preset.*

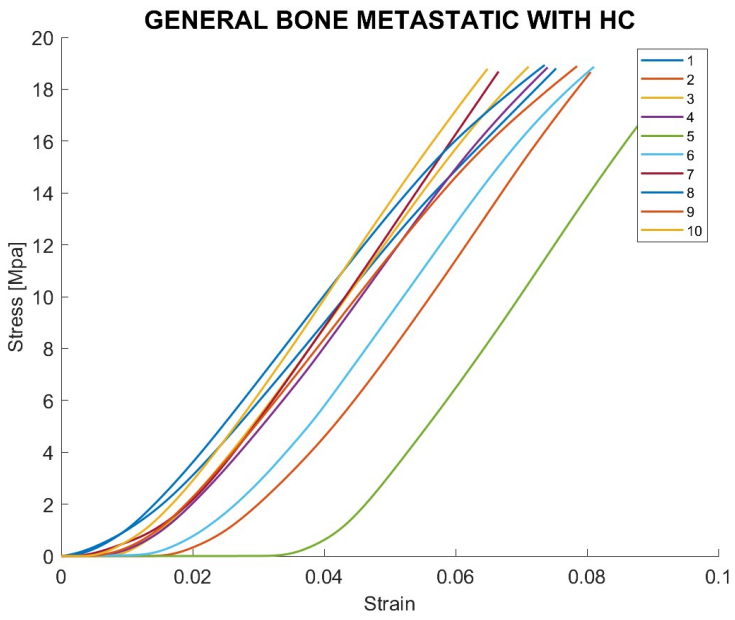

Figure 3.22: *Stress-strain curve of Metastatic samples with metastasis of highly contractible obtained from Clinical CT scan with General Bone preset.*

Also in this case, some differences have been observed between the two types of metastasis. From the T test (Table 3.13), stress and strain obtained a p-value lower than the significance level set at 0.05. So the different type of material used for the metastasis is statistically significant for the model with General Bone preset.

It's important to note that no sample reached fracture, as shown in Figure 3.23.

Figure 3.23: *Sample of General Bone after the mechanical test.*

3.2.5 General Comparison

Micro CT and Clinical CT

In Figure 3.24, all types of anatomical samples printed in this phase from medical images are depicted. The differences between healthy and metastatic samples have already been defined earlier.

Regarding the differences between the two types of medical images, at this point, clinical CT is considered more reliable and closer to human behavior. In comparison, the samples obtained from Micro CT exhibit very low resistance, fracturing after undergoing certain deformations.

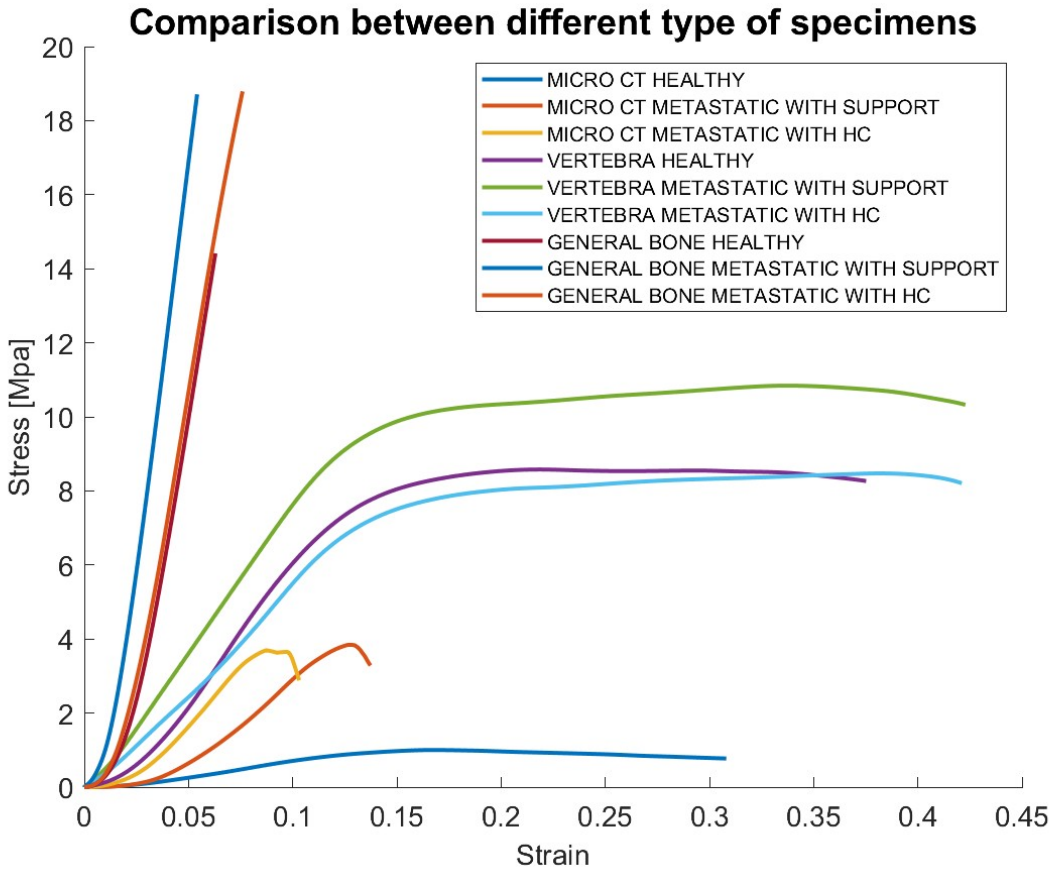

Figure 3.24: *Final comparison between models obtained from Micro CT scan and models obtained from Clinical CT scan.*

As seen in the previous paragraph, those obtained from clinical CT exhibit different behaviors depending on the preset. The General Bone preset has higher resistance but an extremely linear behavior, while the Vertebra preset displays a linear-elastic behavior. Moreover, the mode of failure is similar to that of human vertebrae, especially in the metastatic type with highly contractible material, where the fracture concentrates in the posterior part where the metastasis is concentrated, and the material escapes.

Vertebra and General Bone from Clinical CT scan

Now, focusing on the difference between the two presets: Vertebra and General Bone. Figure 3.25 illustrates the average stress-strain curves of various healthy and metastatic samples with different presets, along with the standard deviation for each type.

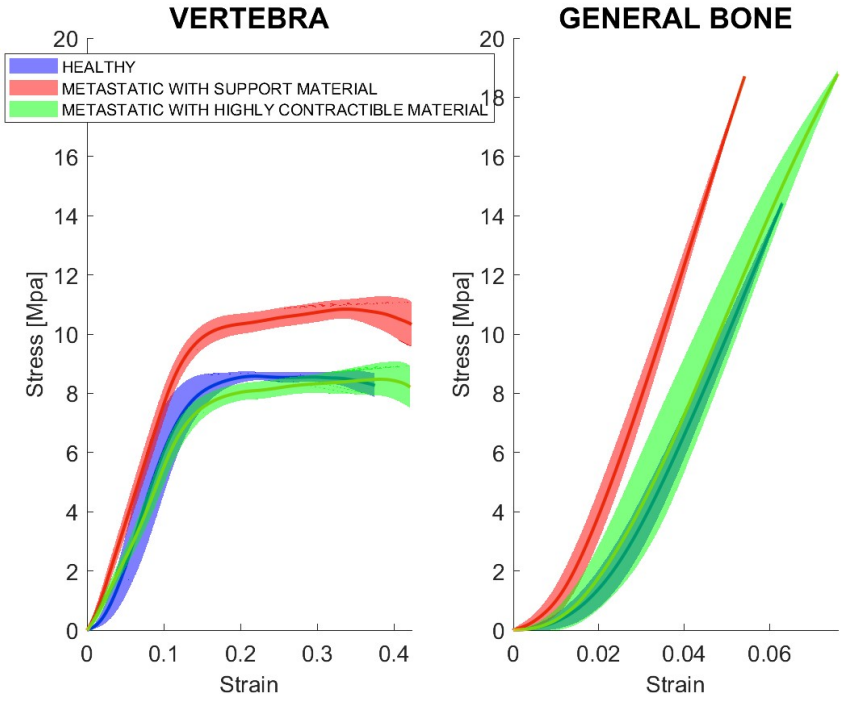

Figure 3.25: *Comparison between models obtained from different preset from Clinical CT scan.*

Comparing the two presets, we can immediately notice that the Vertebra preset exhibits an initially linear and subsequently elastic behavior, while the General Bone preset displays

a nearly rigid, linear behavior. The former has lower stiffness and reaches fracture, while the latter does not reach fracture due to the 10kN load cell limitation.
In both cases, the healthy and metastatic samples with metastases in Highly Contractible material exhibit similar mechanical behavior (as seen in the overlap). Meanwhile, the metastatic samples with metastases in support material show greater resistance in both cases.

Table 3.14: *T-test comparison between healthy and metastatic with HC specimens obtained from Ct Clinical with General Bone and Vertebra preset.*

General Bone - Vertebra	
Healthy	p-value
Stress	2.4116^{-15}
Strain	1.8146^{-7}
Metastatic with HC	p-value
Stress	1.6486^{-13}
Strain	2.0635^{-11}

Based on the T-test (Table 3.14), when comparing the presets, both for healthy and metastatic vertebrae with HC, the obtained p-value is lower than the significance level set at 0.05. With such a low p-value, it can be concluded that the observed difference in strength between the two means is statistically significant. Therefore, the influence of the preset inside the model on the mechanical properties is statistically significant.

In conclusion, after conducting these analyses, it has been established that the model representing the ex vivo human model most accurately is the one configured with the Vertebra setup, specifically the metastatic type with Highly Contractible material.

3.3 Phase 3

3.3.1 Healthy vs Metastatic with Highly Contractible material

Table 3.15 provides the average values of maximum stress, maximum strain, elastic modulus and relative standard deviation for the materials.

Table 3.15: *Data comparison of healthy and metastatic specimens*

SPECIMEN	***HEALTHY***	***METASTATIC WITH HC***
Average value of the maximum stress [MPa]	20.97	27.55
Average value of the maximum strain	0.171	0.150
Average value of Elastic Modulus [MPa]	385.2	547.9
Standard deviation of Elastic Modulus	41.13	20.43
Average value of residual strain	0.126	0.086

The metastatic specimens exhibited higher mechanical properties compared to the healthy specimens.

In graphs 3.26,3.27 are represent stress-strain curve of samples of both typology, healthy and metastatic.

The metastatic samples have a fracture load of approximately 14 kN and are highly repeatable, with expulsion of the metastatic area and orthogonal compression to the loading direction. On the other hand, the healthy samples have a lower fracture load and exhibit a different mode of fracture, occurring along planes at a 45-degree angle to the loading direction.

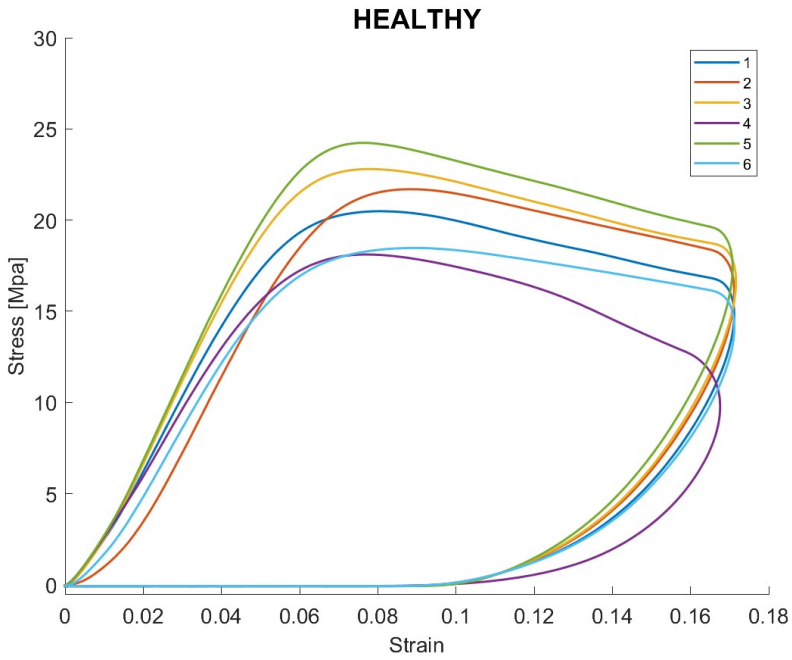

Figure 3.26: *Stress-strain curve of Healthy Specimens with cylinder at ends.*

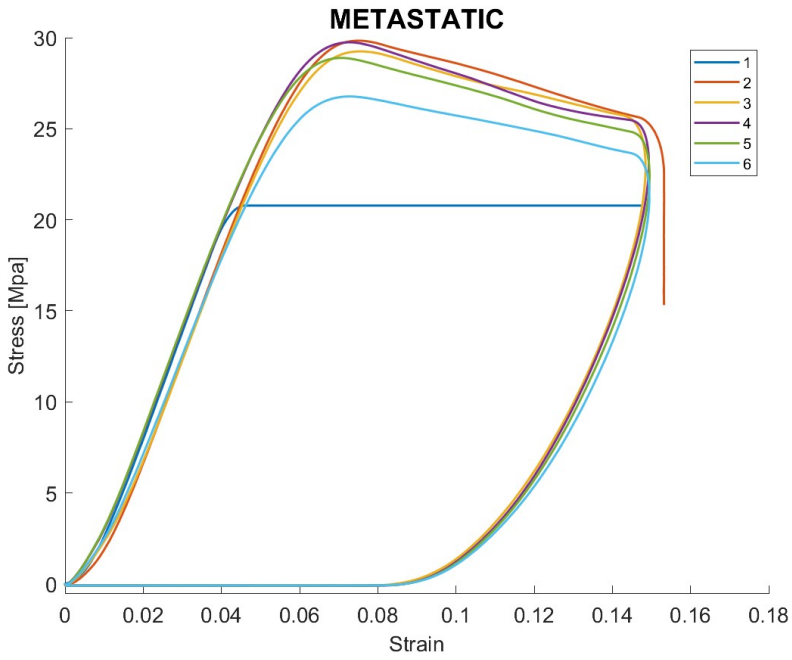

Figure 3.27: *Stress-strain curve of Metastatic specimens with Highly Contractible material and with cylinder at ends.*

The graphs 3.28 shows the mean value for each typology compared.

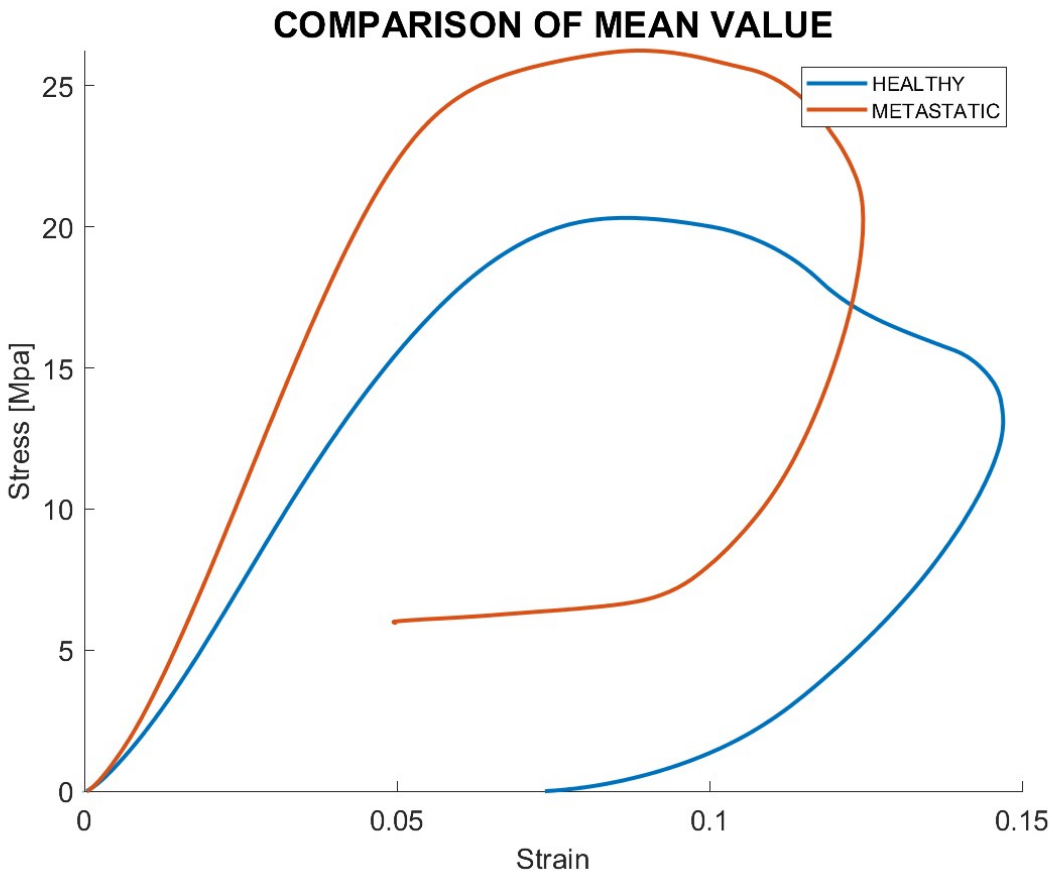

Figure 3.28: *Stress-strain curve of mean value and standard deviation of healthy and metastatic specimens with cylinder at ends.*

Both typologies exhibit high variability, although the deviation is at most 10% compared to the elastic modulus values.

The obtained strain difference value is -12.3, indicating that the metastatic vertebra is less deformed than the healthy one. This is consistent with the previous tests, which showed that the stiffness of the healthy specimens is lower than that of the metastatic ones.

Additionally, the Highly Contractible material inside the metastatic vertebra contributes to its resistance properties. Moreover the Healthy specimens present bigger dimensions than Metastatic, that means that they have more cortical bone so for this reason are less deformed.

In Figure 3.29, it is possible to observe the sample before and after the mechanical test. The compression of the vertebra and the flattening of the trabeculae in the central part of the

specimen are clearly visible.

(a) *Sample before the mechanical test.*

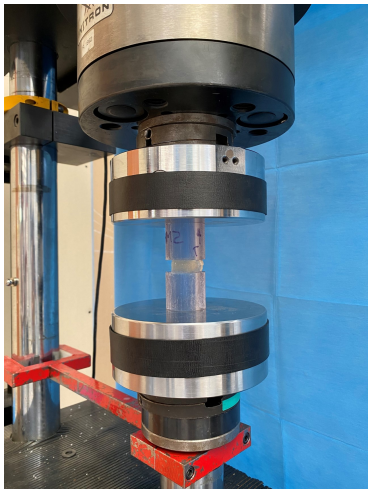

(b) *Mechanical test.*

(c) *Sample after the mechanical test.*

Figure 3.29: *Differences between specimens before and after the test.*

Table 3.16: *T test for Healthy and Metastatic specimens.*

Healthy -Metastatic	
	p-value
Stress	7.621^{-105}
Strain	3.168^{-18}

From the tables 3.16 values the p-value of Healthy - Metastatic comparison is lower than the significance level, set at 0.05. With such a low p-value, it can be stated that the observed difference in strength between the two means is statistically significant. Therefore, the presence and effect of metastasis are statistically significant for the model.

3.3.2 Metastatic with Highly Contractible material vs 'Healed Metastasis'

Table 3.17: *Data of 'healed' specimens.*

SPECIMEN	***HEALED***
Average value of the maximum stress [MPa]	26.04
Average value of the maximum strain	0.150
Average value of Elastic Modulus [MPa]	484.1
Standard deviation of Elastic Modulus	71.18
Average value of residual strain	0.076

Table 3.17 presents the average values of maximum stress, maximum strain, elastic modulus, and relative standard deviation for the materials. The specimens present high variability, although the deviation is at most 15% compared to the elastic modulus value.
In graphs 3.30, stress-strain curves of 'healed' samples are depicted, along with a comparison between mean values and standard deviations. Compared to the metastatic specimens, the 'healed' ones exhibit lower resistance and a more uniform behavior, as evident in the figure 3.31; moreover from the data it has an higher standard deviation.

By calculating the deformation difference a value of 1.13 is obtained, indicating that the metastatic vertebra in this instance is more deformed compared to the 'healed' one.

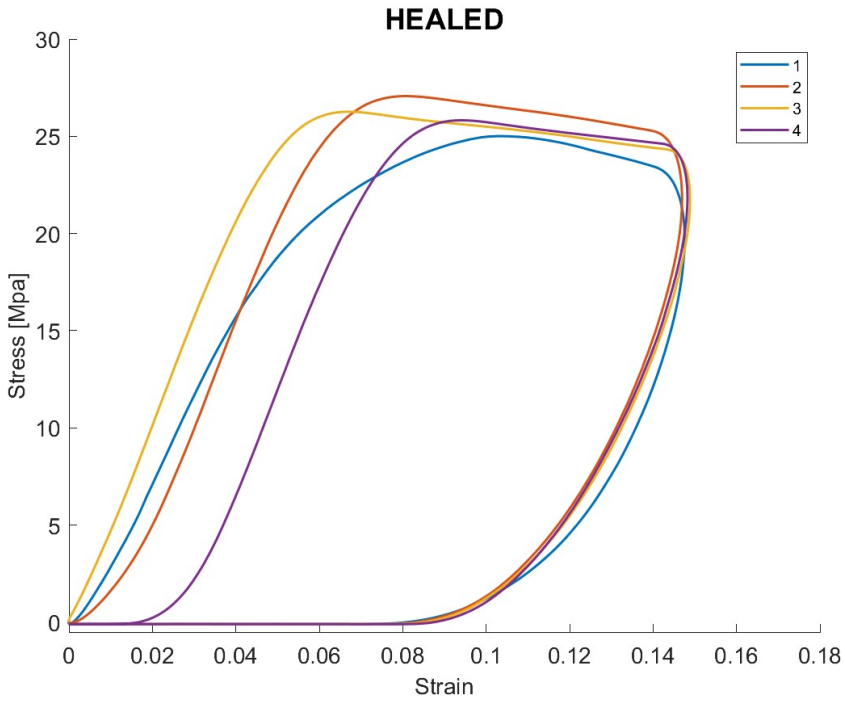

Figure 3.30: *'Stress-strain curve of Healed samples'.*

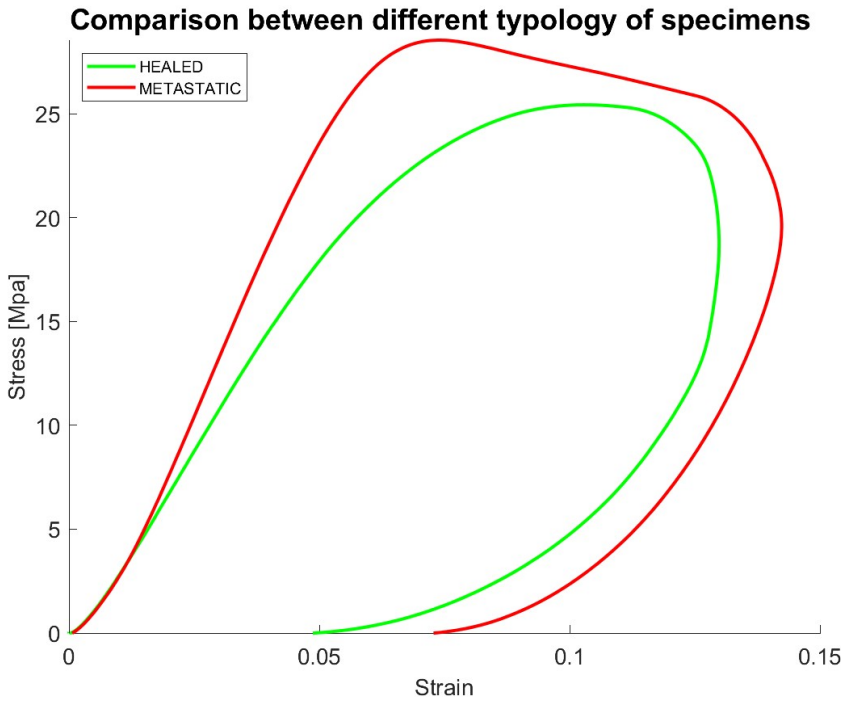

Figure 3.31: *Stress-strain curves comparison between 'Healed' and Metastatic vertebrae.*

Table 3.18: *T test for Metastatic and Healed specimens.*

Metastatic-Healed	
	p-value
Stress	1.149^{-125}
Strain	1.174^{-123}

As can be seen from the tables 3.18 values, in all cases, the obtained p-value is lower than the significance level set at 0.05. With such a low p-value, it can be stated that the observed difference in strength between the two means is statistically significant. Therefore, the presence and effect of metastasis are statistically significant for the model.

3.3.3 General Comparison

In this section, a final comparison was conducted among the types of specimens tested in the third phase (Healthy, Metastatic with HC, and 'Healed').

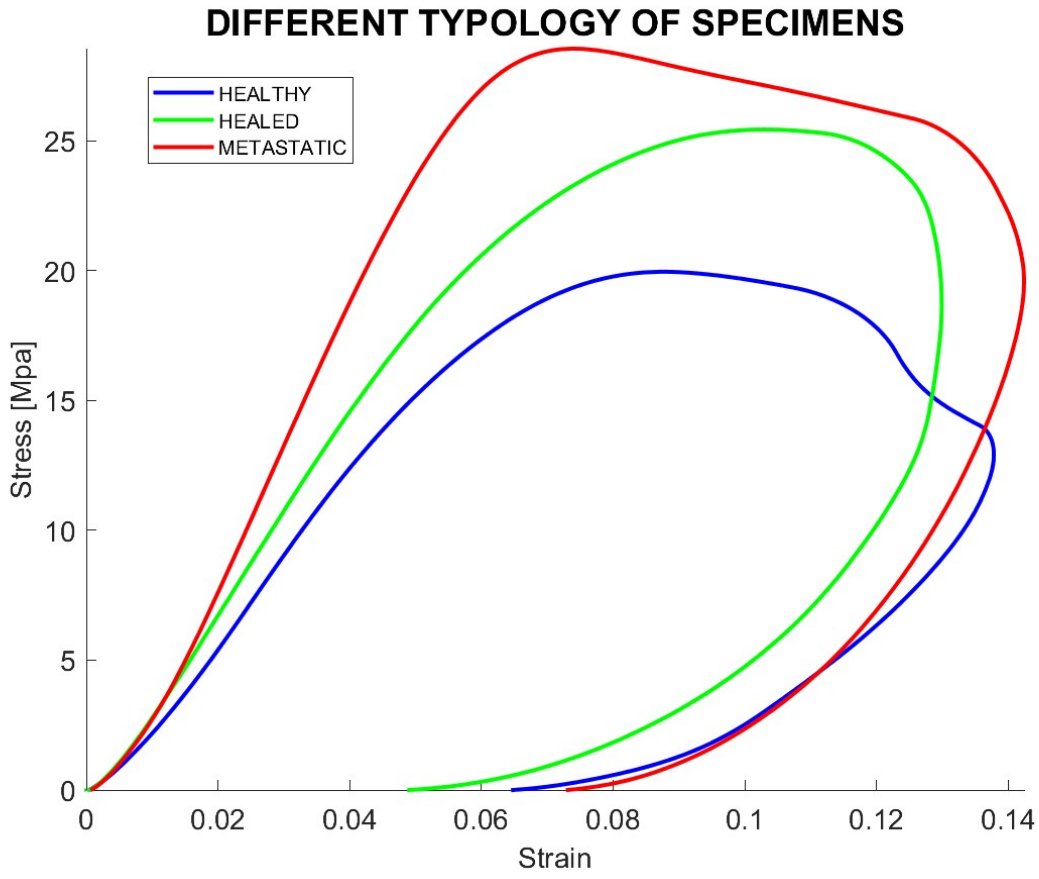

Figure 3.32: *Comparison of mean value curve between Healthy, Metastatic and Healed samples.*

Generally, as depicted in Figure 3.32 the metastatic specimens are the most resistant, and the healthy ones are the least. It's interesting to note that the 'Healed' type falls in between. The trends are close to, but the modes of failure is different.
However, it should be noted that the 'Healed' specimens may have artifacts due to the printing direction. Other factors that may have influenced the results include the temperature conditions for specimen storage, exposure to sunlight, and the printing times, if the aforementioned conditions were met.

Chapter 4

Discussion

The purpose of this study was to develop synthetic anatomical models, specifically vertebrae and metastases, using digital anatomy printing technology to assess and validate their properties compared to real samples. This involved evaluating the compression properties of models obtained from medical images, including clinical CT and Micro CT. All the models were printed using a 3D PolyJet printer from Stratasys.
In the field of biomedicine, 3D printing technology has found extensive applications, especially in various surgical procedures such as spinal, hip, pelvic, knee, foot, ankle, and upper extremity surgeries. In spinal surgery, one of the primary applications is preoperative planning, where 3D printed models are used for complex spinal deformity surgeries. By utilizing MRI and CT scan data, 3D printing technology can accurately reproduce the spinal morphology of patients with actual deformities. However, the focus has primarily been on visualization and aesthetic applications.
Furthermore, 3D printing technology has been used for preoperative planning in the removal of tumor tissues from spinal structures. Recent studies have shown that the Spinal Instability Neoplastic Score (SINS) is not cutting-edge for metastatic vertebrae and that evaluating the type, size, and location of metastases is crucial for assessing spinal instability.

In this study, despite inherent limitations, an attempt was made to address these questions, starting with a characterization of the properties of printable materials used, primarily the bone component. It was observed that all musculoskeletal components available for print-

ing not only had aesthetic and tactile characteristics similar to their human counterparts but also exhibited similar mechanical and structural characteristics. It is important to note that these components are made of polymers, so their mechanical strengths differ (3000 MPa for bone vs 400 MPa for polymers). However, fracture modes and trends are similar. It would be interesting to characterize other bone components and subsequently test complete spinal segments (vertebrae, discs, ligaments, etc.), each with its own mechanical properties.

After studying the properties of the materials, differences between models obtained from Clinical CT and Micro CT were examined. Micro CT offers higher resolution, which is visible in the print, but it can also lead to complications such as segmentation and meshing difficulties. Analyses revealed that Micro CT was not very accurate in representing the mechanical properties of the model, possibly due to segmentation or meshing errors. Clinical CT, on the other hand, proved to be more precise, partly thanks to the available printer presets that simulate the internal structure of the anatomical component by mixing materials to achieve the closest possible physical and mechanical composition. Additionally, using the Digital Anatomy Creator, it is possible to modify these compositions and define specific and customizable materials.

The study also investigated the differences between healthy and metastatic vertebrae, and these differences were extensively characterized. Lytic metastatic vertebrae contain soft elastic tissue inside them instead of trabecular bone, which makes them more resistant than healthy ones. However, this soft elastic material also increases tangential forces and pushes laterally, resulting in a characteristic fracture pattern. Considering that healthy and metastatic vertebrae are adjacent and the comparison is made due to a lack of other possibilities, the introduction of 3D printing (3DP) has allowed for more in-depth studies. Once the printer preset has been validated as a plausible representation of a musculoskeletal component, in this case, trabecular and cortical bone, it becomes possible to remove the metastasis from the metastatic vertebra and fill it using software presets as if it were healthy. This enables a true comparison between healthy and metastatic vertebrae because they are no longer two adjacent vertebrae but the same one.

Compared to ex-vivo tests, the use of 3D printed models reduces variability, as the printer offers a high level of precision, reduces costs (compared to donor specimen costs), and, most

importantly, allows for many more replicas of the same component with the same disease. This makes this method a repeatable, reproducible, and customizable alternative to using ex-vivo models. However, there are still inconsistencies in the mechanical resistance properties at the moment, even though the fracture mode can be replicated.

4.1 Limitations of the study

Clinical Data and Procedures

There are some limitations in this study that must be considered. Firstly, all anatomical samples were obtained from medical images, so the quality of these images may vary and could contain artifacts that might alter the Hounsfield Units (HU). Additionally, the quality of the scanner can affect the level of detail in the final image. Although segmentation software simplifies the process using specific tools and automatic segmentation based on Hounsfield Units, in some cases (such as details or image quality), manual intervention may be necessary, introducing the potential for human error and subsequent artifacts.
It should also be noted that this was a novel and innovative method for using these types of 3D printed synthetic models. Therefore, there was no established protocol to reference, but efforts were made to maintain consistent setups and test conditions for each sample.

Materials and Printing

The main limitation concerning materials is the polymers themselves. These materials have lower mechanical properties compared to human bone and can also be influenced by heat, which can alter their properties and, consequently, their strength. The 3D printer itself can introduce limitations as well. All printing parameters, such as print orientation, timing, etc., influence the characteristics of the model, including its surface properties. These characteristics are highly dependent on factors like exposure to sunlight and oxygen. Furthermore, the presets used for printing the models, while highly customizable and featuring various characteristics, are constrained by the printer's ability to combine seven materials, and the materials themselves are not well-known or tested in a mechanical context.

Analysis

Another limitation is the relatively small sample size, which limits the generalizability of the findings. All models were created from medical images obtained from a spinal segment with a disease. Additionally, the analysis focused on a single type of load and tested the vertebral body under axial compression conditions (following the ASTM protocol). However, a comprehensive and detailed analysis was performed on each specimen, evaluating their local properties and comparing the results for each type. Nevertheless, the modes of failure observed in this study were consistent with those reported in other studies involving ex vivo specimens.

Another important limitation pertains to the shape of the specimens. To avoid milling and, consequently, altering the model's structure, an assembly method using two cylinders at the ends was chosen. However, using this approach, the stiffness values obtained are higher because the cylinders are stronger than the anatomical model. Furthermore, by using this setup, local deformations are avoided. Nevertheless, it should be acknowledged that this setup is not an exact replica of the physiological human model.

Chapter 5

Conclusion

In this study, for the first time, the Digital Anatomy Printer was utilized to create synthetic anatomical models used for mechanical characterization rather than surgical planning. More specifically, vertebral and metastatic models were developed to replicate the mechanical behavior of ex-vivo models. To address this objective, over a hundred samples underwent compression testing.

Through an innovative approach to 3D printing, which considered the mechanical properties of Digital Material and the use of Digital Anatomy Creator, an acceptable level of accuracy and precision was achieved in investigating the differences between vertebrae with and without pathologies, particularly those with lytic metastases, and in assessing the risk of fracture.

The mechanical properties of each Digital Material were measured and then compared. The results revealed distinct behaviors among individual materials and different presets, with varying trends. Additionally, differences between models printed from different medical image segmentations were examined, showing higher accuracy and better mechanical characteristics for the models obtained from clinical CT scans.

Furthermore, an analysis of the morphological effect was conducted on the anatomical models. Vertebral segments affected by lytic metastases exhibited overall higher strains compared to control vertebrae. Moreover, a similar fracture location and mode of failure were identified compared to ex-vivo models.

This method, along with the associated evidence, when applied to a larger sample, could be instrumental in implementing new biomechanical-based criteria for predicting the risk of bone

metastasis-related fractures. These new paradigms could contribute to standardizing and customizing scenarios in this field.

Looking ahead, there are several areas that merit attention. Firstly, there is the potential to analyze subjects with various pathologies, including blastic or mixed vertebrae and osteoporotic diseases. This expansion could enhance the possibilities for replicating ex-vivo tests. Additionally, there is a need to develop digital materials with high mechanical properties and increased rigidity. This advancement could open up new possibilities, including the potential use of implantable devices in conjunction with biocompatible materials.
Furthermore, with the introduction of new features, future studies could focus on fully characterizing a spinal segment. This would involve printing and assembling all the components, each with its unique characteristics, contributing to an overall representation of the spinal column.

Appendix A

Digital Anatomy Creator

The Digital Anatomy Creator (DAC) is a powerful tool that generates unique presets, prepares models for printing and facilitates project sharing [54]. It provides a detailed view of each cross-section of a model and offers a wide range of options for assigning materials that influence the mechanical properties of the model. When used for printing anatomical structures, the DAC produces high-quality products that closely resemble real anatomy. Layers can be constructed using various materials, structures, thicknesses, and other properties.

In the DAC, each model includes a default background and outer layer. The background layer is automatically applied to all models, regardless of their size and it has an infinite size, covering the entire model to ensure the printer does not print empty space. It serves as the lowest-priority layer and comes into play when no other layer is defined. Furthermore, there is the outer layer, which has the highest priority and is at least 0.3 mm thick. Its purpose is to ensure compliance with Digital Anatomy Printer limitations.

Beyond these default layers, users can add and modify layers as needed to achieve specific mechanical properties. Each layer can incorporate up to 7 different materials, including support materials. Users have the flexibility to define the ratio and threshold of materials based on the requirements of their models.

The DAC also offers various Noise Functions (Digital Material, Perlin, Cubes Grid, Scattered Sphere, Gyroid), each providing distinct mechanical properties and visual characteristics for the layer and the model. For the Vertebra and General Bone presets, the Perlin noise function is employed, creating amorphous 3D structures composed of different materials with dy-

namic thresholds and scales. This function involves continuous and nonlinear combinations of advanced mathematical equations. In contrast, the Myocardium preset utilizes the Gyroid noise function, generating 3D wave-like patterns that give the layer an isotropic structure. An isotropic structure exhibits uniform physical properties in all directions, such as breaking points, elasticity, and stiffness.
Moreover, the size of elements inside the noise functions can be adjusted using the scale factor. Additionally, three properties (Edge Blending, Dynamic Layer Thickness, Noise Modulation) offer control over the mechanical and visual aspects of a model:

- The Edge Blending option defines the transition gradient between two layers by specifying the distance between the selected layer and those preceding and following it. This function distributes a random mixture of material from the selected layer over the other layer in a linear gradient that matches the chosen thickness.
- The Dynamic Layer Thickness option allows for changing the layer's thickness along the model's long axis.
- The Noise Modulation option creates a gradient of ratios or thresholds for materials in the selected layer. Unlike Edge Blending, which affects layer dimensions, Noise Modulation is manifested within the layer itself.

Figure A.1: *Composition of preset Vertebra Porous by DAC*

In this study, we focused on the Porous Vertebra preset and assessed the variation in mechanical properties by modifying its internal characteristics. The general structure of the preset (Figure A.1) consists of:

- Outer layer : 0.35 mm composed entirely of Bone matrix.
- Layer 1: Ranging from 0.35 mm to 2 mm (1.65 mm in total thickness) with 90% Bone matrix and 10% Vero Pure White, along with an edge blending parameter from 0 to 1.
- Background: Ranging from 0 to 50 is made of support material (SUP706) and from 50 to 100, it consists of Vero Pure White.

(a) *Replacing Vero Pure White with Vero Clear and using Gel Matrix instead of support material (GM).*

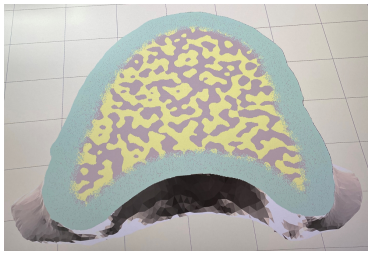

(b) *Replacing Vero Pure White with Vero Clear (VC).*

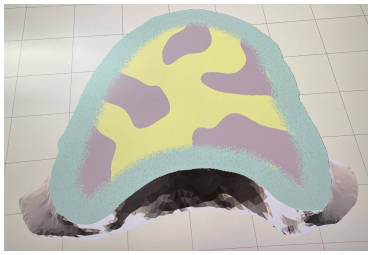

(c) *Replacing Vero Pure White with Vero Clear and also multiplying the scale factor by 5 (VC5).*

(d) *GM*

(e) *VC*

(f) *VC5*

Figure A.2: *Visualitation of the different composition in DAC and printed.*

We conducted three tests with different compositions (Figure A.2):

1. Replacing Vero Pure White with Vero Clear and using Gel Matrix instead of support material (GM).

2. Replacing Vero Pure White with Vero Clear (VC).

3. Replacing Vero Pure White with Vero Clear and also multiplying the scale factor by 5 (VC5).

Two samples were printed for each composition, one healthy and one metastatic. The obtained values of stress, strain and elastic modulus for these various models are summarized in the table A.1 and visualized in the figure A.3. We compared this data with a model of a vertebra using the original preset. It's noteworthy that the original preset values are lower due to the higher strength of Vero Clear compared to Vero Pure White. As for the graphs, they exhibit similar behavior in the initial phase across all compositions, but in the latter part, they display distinct behaviors. In general, there is potential for conducting numerous different tests, which could be explored further for the development of presets that closely mimic and are more customizable to the properties of the human body. However, for now, this part of the study concludes at this point.

Table A.1: *Data comparison between different composition*

	GM	**VC**	**VC5**	**VP**
Healthy				
Max stress [MPa]	12.31	11.48	12.21	8.71
Max strain	0.322	0.446	0.174	0.375
Elastic Modulus [MPa]	55.62	60.96	69.29	81.92
Metastatic				
Max stress [MPa]	13.05	11.67	13.15	10.92
Max strain	0.302	0.459	0.265	0.423
Elastic Modulus [MPa]	53.30	66.04	66.79	77.74

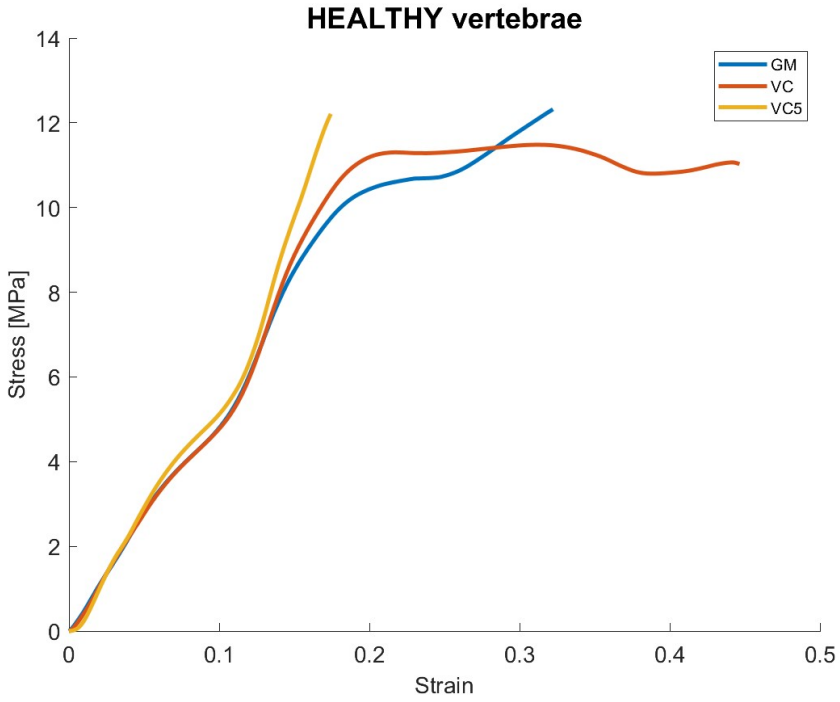

(a) *Comparison between different composition of healthy vertebrae: GM, VC and VC5*

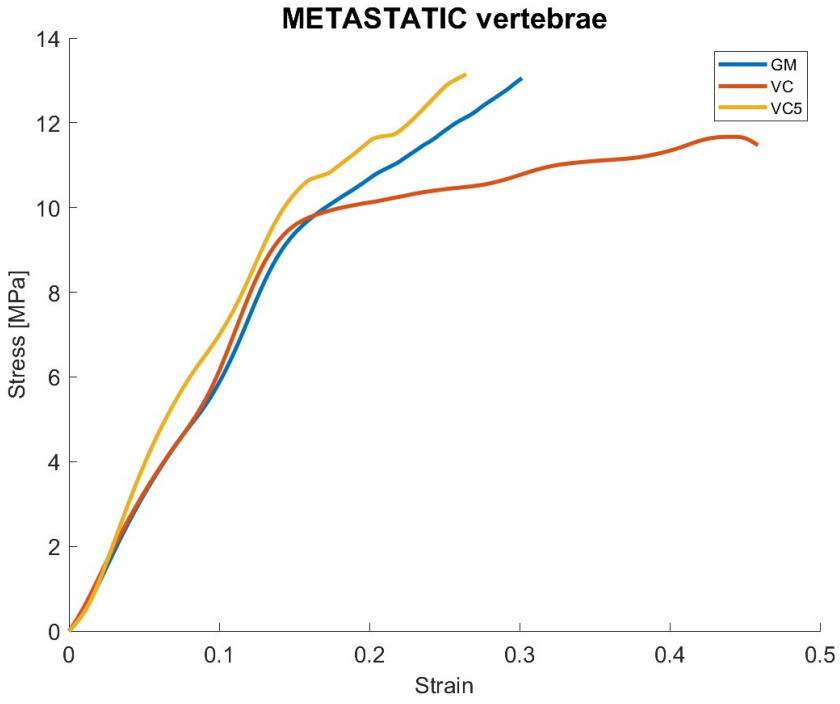

(b) *Comparison between different composition of metastatic vertebrae: GM, VC, VC5*

Figure A.3: *Stress-strain graphs.*

Appendix B

Confined compression test of metastasis

During the study, were utilized two different materials to characterize and represent metastasis: Highly Contractible (Structural Heart Myocardium) and Support material.
In general, a lower strength is observed in metastatic vertebrae. Regarding vertebrae with lytic metastasis, this lower resistance can be explained by considering that the structure is damaged by an empty zone where the bone tissue is replaced by soft tumor tissue [9].
Using the Digital Anatomy Creator, we determined that the composition of the Highly Contractible Myocardium consists of 50% Agilus30 and 50% Tissue Matrix in the core, with an outer layer of 0.4 mm of Agilus30. After conducting an analysis and study of the properties of printable digital materials, Highly Contractible appears to be the most suitable choice due to its soft tissue nature and specific elasticity. So was decided to further investigate its mechanical characteristics through confined compression tests. Since there are no regulations regarding confined compression tests of polymeric materials, was created a custom setup to test the samples.
The dimensions of the samples and test times were referenced to ASTM standard D695-15, which is the Standard Test Method for Compressive Properties of Rigid Plastic. The machine used for the mechanical tests was an MTS Insight ElectroMechanical, equipped with a 10kN load cell and the test setup employing a simple load ramp with a speed of 1.3 mm/min.

The following figures (B.1) depict the components used in the setup, namely the piston, outer cylinder, and sample.

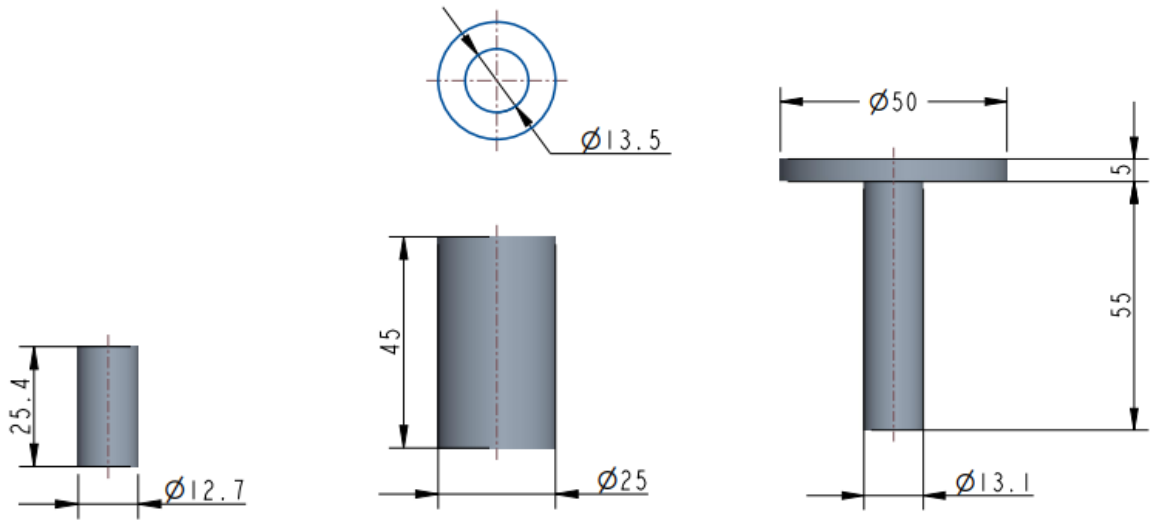

(a) *Cylinder.* **(b)** *Outer cylinder.* **(c)** *Piston.*

Figure B.1: *CAD setup for confined compression test*

The dimensions were evaluated based on the standard sample and within tolerance. Both the piston and the outer cylinder were manufactured from 316L stainless steel. Five samples were printed. From these test was obtained the maximum stress, strain and elastic modulus within the linear region. The data are summarized in the table B.1. The graphs B.2 shows that the samples exhibit an initial compression phase with high strain at constant stress and nearly zero. This is the loading and crushing phase of the sample, followed by a linear behavior leading to sample failure.

Table B.1: *Data from confined compression test.*

	HC1	**HC2**	**HC3**	**HC4**	**HC5**	***Average***
Max stress [MPa]	9.66	6.55	8.01	11.10	10.24	9.11
Max strain	0.081	0.072	0.065	0.070	0.083	0.074
Elastic Modulus of linear region [MPa]	719.9	796.6	955.6	904.8	1108.1	911.4

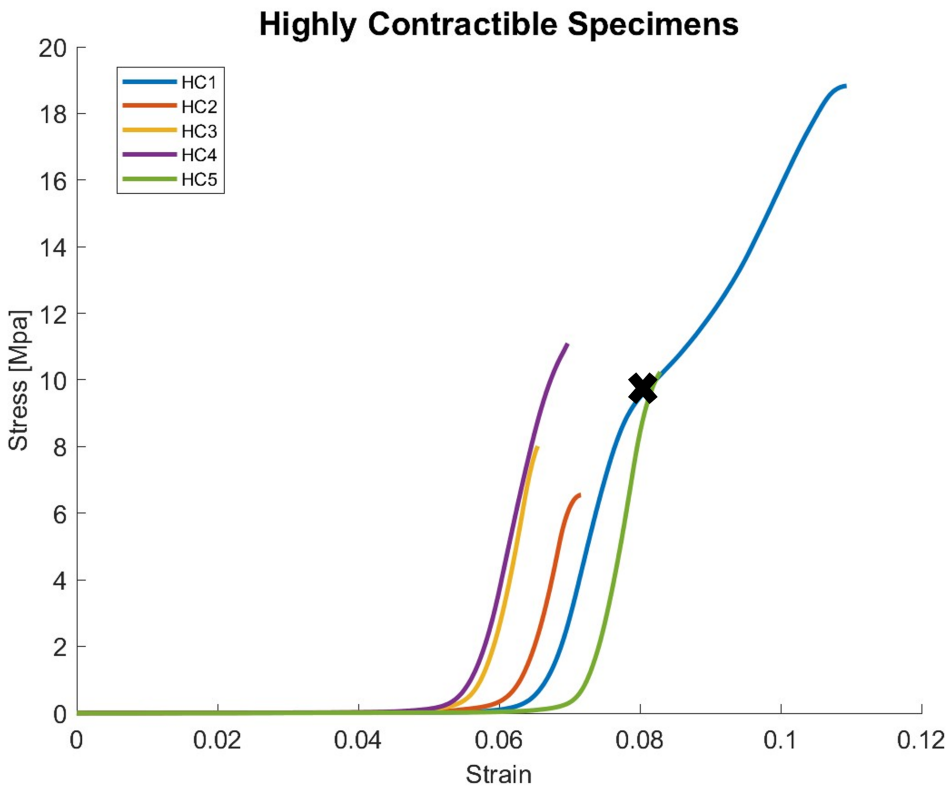

Figure B.2: *Stress-strain graph of confined compression test of Highly Contractible material.*

(a) *Setup confined compression test.*

(b) *Fracture mode of the HC samples after confined compression test.*

Figure B.3

In Sample 1, we continued to assess stresses even after the initial failure, where ”X” represents the point of first damage or failure. As we can observe, the material can withstand much higher stresses until complete compression. This could also be attributed to the presence of the outer steel cylinder, which has significantly higher strength compared to polymeric materials. The fracture mode of all samples resulted in an inclination of approximately 45 degrees, as depicted in the figure B.3. This may be due to inappropriate tolerances in the setup.
The study concluded with this characterization, confirming that the HC material exhibits an elastic and linear behavior that generally corresponds to that of metastasis within vertebrae.

Bibliography

[1] Marco Palanca, Luca Cristofolini, Alessandro Gasbarrini, Giuseppe Tedesco, and Giovanni Barbanti-Bròdano. Assessing the mechanical weakness of vertebrae affected by primary tumors: A feasibility study. *Materials*, 13(15), 2020.

[2] R. Coleman. Incidence and distribution of bone metastases. In Ingo J. Diel, M. Kaufmann, and G. Bastert, editors, *Metastatic Bone Disease*, pages 20–30, Berlin, Heidelberg, 1994. Springer Berlin Heidelberg.

[3] Marco Palanca, Giulia Cavazzoni, and Enrico Dall'Ara. The role of bone metastases on the mechanical competence of human vertebrae. *Bone*, 173:116814, 2023.

[4] Yasuaki Tokuhashi, Hiromi Matsuzaki, Hiroshi Oda, Masashi Oshima, and Junnosuke Ryu. A revised scoring system for preoperative evaluation of metastatic spine tumor prognosis. *Spine*, 30 19:2186–91, 2002.

[5] Blusson Spinal Cord Centre 6th Floor 818 W10th Avenue Vancouver V5Z 1M9 BC (Canada)] Reynolds Jeremy J Sahgal Arjun Department of Radiation Oncology Sunnybrook Health Sciences Center University of Toronto Toronto ON (Canada)] Fehlings Michael G Krembil Neuroscience Centre Toronto Western Hospital Toronto ON (Canada)] Gokaslan Ziya L Schouten Rowan Versteeg Anne L Boriani Stefano Varga Peter Pal Rhines Laurence D Kawahara Norio Fourney Daryl Fisher, Charles G and Lorna Weir. Reliability of the spinal instability neoplastic score (sins) among radiation oncologists: an assessment of instability secondary to spinal metastases, Mar 2014.

[6] Marco Palanca, Giovanni Barbanti-Bròdano, Daniele Marras, Mara Marciante, Michele Serra, Alessandro Gasbarrini, Enrico Dall'Ara, and Luca Cristofolini. Type, size, and

position of metastatic lesions explain the deformation of the vertebrae under complex loading conditions. *Bone*, 151:116028, 2021.

[7] Ron Alkalay. Effect of the metastatic defect on the structural response and failure process of human vertebrae: An experimental study. *Clinical Biomechanics*, 30, 10 2014.

[8] Ron Alkalay and Timothy Harrigan. Mechanical assessment of the effects of metastatic lytic defect on the structural response of human thoracolumbar spine. *Journal of orthopaedic research : official publication of the Orthopaedic Research Society*, 34, 01 2016.

[9] Marc A. Stadelmann, Denis E. Schenk, Ghislain Maquer, Christopher Lenherr, Florian M. Buck, Dieter D. Bosshardt, Sven Hoppe, Nicolas Theumann, Ron N. Alkalay, and Philippe K. Zysset. Conventional finite element models estimate the strength of metastatic human vertebrae despite alterations of the bone's tissue and structure. *Bone*, 141:115598, 2020.

[10] Marco Palanca, Gianluca Tozzi, and Luca Cristofolini. The use of digital image correlation in the biomechanical area: a review. *International Biomechanics*, 3(1):1–21, 2016.

[11] Enrico Dall'Ara, Marta Peña-Fernández, Marco Palanca, Mario Giorgi, Luca Cristofolini, and Gianluca Tozzi. Precision of digital volume correlation approaches for strain analysis in bone imaged with micro-computed tomography at different dimensional levels. *Frontiers in Materials*, 4, 2017.

[12] Giulia Cavazzoni. *In vitro characterization of the three-dimensional strain pattern in human vertebrae affected by metastases*. PhD thesis.

[13] Cyrille B. Confavreux, Helene Follet, David Mitton, Jean Baptiste Pialat, and Philippe Clézardin. Fracture risk evaluation of bone metastases: A burning issue. *Cancers*, 13(22), 2021.

[14] Marco Palanca, Sara Oliviero, and Enrico Dall'Ara. Microfe models of porcine vertebrae with induced bone focal lesions: Validation of predicted displacements with digital volume correlation. *Journal of the Mechanical Behavior of Biomedical Materials*, 125:104872, 2022.

[15] Nicolas Jaumard, Jennifer Leung, Akhilesh Gokhale, Ben Guarino, William Welch, and Beth Winkelstein. Relevant anatomic morphological measurements of the rat spine: Considerations for rodent models of human spine trauma. *Spine*, 40, 10 2015.

[16] Augustus A. White and Manohar M. Panjabi. *Clinical biomechanics of the spine / Augustus A. White III, Manohar M. Panjabi.* Philadelphia : Lippincott, 1978.

[17] Anthony V. D'Antoni*. Gray's anatomy, the anatomical basis of clinical practice, forty-first edition, by susan standring, editor-in-chief, elsevier limited, 2016, 1,562 pages, hardcover, $228.99 ($171.74), isbn: 978-0-7020-5230-9. *Clinical Anatomy*, 29(2):264–265, 2016.

[18] Anthony(Tony) Cassidy and Richard Lynn. A multifactorial approach to achievement motivation: The development of a comprehensive measure. *Journal of Occupational Psychology*, 62:301–312, 12 1989.

[19] Richard M. Aspden. Review of the functional anatomy of the spinal ligaments and the lumbar erector spinae muscles. *Clinical Anatomy*, 5(5):372–387, 1992.

[20] Amira I. Hussein, Zachary D. Mason, and Elise F. Morgan. Presence of intervertebral discs alters observed stiffness and failure mechanisms in the vertebra. *Journal of Biomechanics*, 46(10):1683–1688, 2013.

[21] Sabrina Donzelli, Salvatore Poma, Luca Balzarini, Alberto Borboni, Stefano Respizzi, Jorge Villafañe, Fabio Zaina, and Stefano Negrini. State of the art of current 3-d scoliosis classifications: a systematic review from a clinical perspective. *Journal of neuroengineering and rehabilitation*, 12:91, 10 2015.

[22] Eva Barrett, Karen McCreesh, and Jeremy Lewis. Reliability and validity of non-radiographic methods of thoracic kyphosis measurement: A systematic review. *Manual Therapy*, 19(1):10–17, 2014.

[23] Ori Hay, Gali Dar, Janan Abbas, Dan Stein, Hila May, Youssef Masharawi, Nathan Peled, and Israel Hershkovitz. The lumbar lordosis in males and females, revisited. *PLOS ONE*, 10(8):1–17, 08 2015.

[24] Holger Ritzel, Michael Amling, Martin Pösl, Michael Hahn, and Günter Delling. The thickness of human vertebral cortical bone and its changes in aging and osteoporosis: A histomorphometric analysis of the complete spinal column from thirty-seven autopsy specimens. *Journal of Bone and Mineral Research*, 12(1):89–95, 1997.

[25] Gulay Karaguzel and Michael Holick. Diagnosis and treatment of osteopenia. *Reviews in endocrine metabolic disorders*, 11:237–51, 12 2010.

[26] MJ Silva, TM Keaveny, and WC Hayes. Load sharing between the shell and centrum in the lumbar vertebral body. *Spine*, 22(2):140—150, January 1997.

[27] Ricardo Botelho, Matheus Oliveira, and José Rotta. Quantification of vertebral involvement in metastatic spinal disease. *The open orthopaedics journal*, 7:286–91, 08 2013.

[28] Cari M. Whyne. Biomechanics of metastatic disease in the vertebral column. *Neurological Research*, 36(6):493–501, 2014. PMID: 24797237.

[29] George Howard Bell, Olive Dunbar, James S. P. Beck, and Aj Gibb. Variations in strength of vertebrae with age and their relation to osteoporosis. *Calcified Tissue Research*, 1:75–86, 2005.

[30] Tommy Hansson and Bengt Roos. The influence of age, height, and weight on the bone mineral content of lumbar vertebrae. *SPINE 5(6):p 545-551*, November 1980.

[31] R.E. Coleman. Metastatic bone disease: clinical features, pathophysiology and treatment strategies. *Cancer Treatment Reviews*, 27(3):165–176, 2001.

[32] Marco Palanca, Giovanni Barbanti-Bròdano, and Luca Cristofolini. The Size of Simulated Lytic Metastases Affects the Strain Distribution on the Anterior Surface of the Vertebra. *Journal of Biomechanical Engineering*, 140(11):111005, 08 2018.

[33] Ilya Laufer, David G. Rubin, Eric Lis, Brett W. Cox, Michael D. Stubblefield, Yoshiya Yamada, and Mark H. Bilsky. The NOMS Framework: Approach to the Treatment of Spinal Metastatic Tumors. *The Oncologist*, 18(6):744–751, 05 2013.

[34] Fabio Galbusera, Zhihui Qian, Gloria Casaroli, Tito Bassani, Francesco Costa, Benedikt Schlager, and Hans-Joachim Wilke. The role of the size and location of the tumors and of the vertebral anatomy in determining the structural stability of the metastatically involved spine: a finite element study. *Translational Oncology*, 11(3):639–646, 2018.

[35] M.C. Costa, P. Eltes, A. Lazary, P.P. Varga, M. Viceconti, and E. Dall'Ara. Biomechanical assessment of vertebrae with lytic metastases with subject-specific finite element models. *Journal of the Mechanical Behavior of Biomedical Materials*, 98:268–290, 2019.

[36] Daryl R. Fourney, Evan M. Frangou, Timothy C. Ryken, Christian P. DiPaola, Christopher I. Shaffrey, Sigurd H. Berven, Mark H. Bilsky, James S. Harrop, Michael G. Fehlings, Stefano Boriani, Dean Chou, Meic H. Schmidt, David W. Polly, Roberto Biagini, Shane Burch, Mark B. Dekutoski, Aruna Ganju, Peter C. Gerszten, Ziya L. Gokaslan, Michael W. Groff, Norbert J. Liebsch, Ehud Mendel, Scott H. Okuno, Shreyaskumar Patel, Laurence D. Rhines, Peter S. Rose, Daniel M. Sciubba, Narayan Sundaresan, Katsuro Tomita, Peter P. Varga, Luiz R. Vialle, Frank D. Vrionis, Yoshiya Yamada, and Charles G. Fisher. Spinal instability neoplastic score: An analysis of reliability and validity from the spine oncology study group. *Journal of Clinical Oncology*, 29(22):3072–3077, 2011. PMID: 21709187.

[37] Michael R. Hardisty, Margarete K. Akens, Seyed-Parsa Hojjat, Albert Yee, and Cari M. Whyne. Quantification of the effect of osteolytic metastases on bone strain within whole vertebrae using image registration. *Journal of Orthopaedic Research*, 30(7):1032–1039, 2012.

[38] M. Marciante M. Serra A. Gasbarrini e G. BarbantiBròdano Palanca, L. Cristofolini. Lack of correlation between the sins and the biomechanical outcomes in case of metastatic vertebra. *GSC2020*, 2020.

[39] Hiroshi Taneichi, Kiyoshi Kaneda, Naoki Takeda, Kuniyoshi Abumi, and Shigenobu Satoh. Risk factors and probability of vertebral body collapse in metastases of the thoracic and lumbar spine. *Spine*, 22 3:239–45, 1997.

[40] Nicola Brandolini, Luca Cristofolini, and Marco Viceconti. Experimental methods for the biomechanical inestigation of the human spine: A reiew. *Journal of Mechanics in Medicine and Biology*, 11 2013.

[41] Nicolas Jaumard, J. Leung, A. J. Gokhale, Benjamin B. Guarino, William C. Welch, and Beth A. Winkelstein. Relevant anatomic and morphological measurements of the rat spine: Considerations for rodent models of human spine trauma. *An International journal for the study of the spine*, 40:E1084–E1092, 2015.

[42] Alessandro Marro, Taha Bandukwala, and Walter Mak. Three-dimensional printing and medical imaging: A review of the methods and applications. *Current Problems in Diagnostic Radiology*, 45(1):2–9, 2016.

[43] Francesca Uccheddu, Monica Carfagni, Lapo Governi, Rocco Furferi, Yary Volpe, and Erica Nocerino. 3d printing of cardiac structures from medical images: an overview of methods and interactive tools. *International Journal on Interactive Design and Manufacturing (IJIDeM)*, 12, 05 2018.

[44] Daniel Rittirsch, Edouard Battegay, Lukas Zimmerli, Werner Baulig, Donat Spahn, Chris Ossendorf, Guido Wanner, Hans-Peter Simmen, and Clément Werner. Cement-augmented dorsal instrumentation of the spine as a safe adjunct to the multimodal management of metastatic pheochromocytoma: A case report. *Patient safety in surgery*, 6:1, 01 2012.

[45] Manaswini Jena, Smita Mishra, and Debahuti Mishra. A survey on applications of machine learning techniques for medical image segmentation. *International Journal of Engineering and Technology*, 7:4489–4495, 01 2018.

[46] F. Rengier, Amit Mehndiratta, Hendrik Von Tengg-Kobligk, Christian Zechmann, Roland Unterhinninghofen, Hans-Ulrich Kauczor, and Frederik Giesel. 3d printing based on imaging data: Review of medical applications. *International Journal of Computer Assisted Radiology and Surgery*, 5:335–341, 07 2010.

[47] Martelli P et al. Alessandri G, Santi GM. 3d-printing of porous structures for reproduction of a femoral bone. *F1000Research*, 2023.

[48] Paolo Gargiulo. *Handbook of Surgical Planning and 3D Printing: Applications, Integration, and New Directions*. 04 2023.

[49] Thore Bücking, Emma Hill, James Robertson, Efthymios Maneas, Andrew Plumb, and Daniil Nikitichev. From medical imaging data to 3d printed anatomical models. *PLOS ONE*, 12:e0178540, 05 2017.

[50] Parth Patpatiya, Kailash Chaudhary, Anshuman Shastri, and Shailly Sharma. A review on polyjet 3d printing of polymers and multi-material structures. *Proceedings of the Institution of Mechanical Engineers, Part C: Journal of Mechanical Engineering Science*, 236:095440622210795, 04 2022.

[51] Peng C. Pille P. et al. Tee, Y.L. 3d printing of composite materials: Experimental and modelling approach. *JOM 72, 1105–1117*, 2020.

[52] Stratasys. *Technical Application Guide Digital Anatomy Printer*, 2022.

[53] Standard test method for compressive properties of rigid plastics. Technical report, ASTM, 2015.

[54] Stratasys. *Technical Application Guide Digital Anatomy Creator*, 2021.